DEVELOPMENT OF NON-NOBLE (Co-N/MWCNT) AND POLYBENZIMIDAZOLE-MODIFIED (Pt-PBI/MWCNT) ELECTROCATALYSTS FOR HIGH-TEMPERATURE PEM FUEL CELL APPLICATIONS

A THESIS SUBMITTED TO
THE GRADUATE SCHOOL OF NATURAL AND APPLIED SCIENCES
OF
MIDDLE EAST TECHNICAL UNIVERSITY

BY
ENİS OĞUZHAN EREN

IN PARTIAL FULFILLMENT OF THE REQUIREMENTS
FOR
THE DEGREE OF MASTER OF SCIENCE
IN
POLYMER SCIENCE AND TECHNOLOGY

MAY 2020

Approval of the thesis:

DEVELOPMENT OF NON-NOBLE (Co-N/MWCNT) AND POLYBENZIMIDAZOLE-MODIFIED (Pt-PBI/MWCNT) ELECTROCATALYSTS FOR HIGH-TEMPERATURE PEM FUEL CELL APPLICATIONS

submitted by **ENİS OĞUZHAN EREN** in partial fulfillment of the requirements for the degree of **Master of Science in Polymer Science and Technology Department, Middle East Technical University** by,

Prof. Dr. Halil Kalıpçılar
Dean, Graduate School of **Natural and Applied Sciences** _____

Prof. Dr. Necati Özkan
Head of Department, **Polymer Sci. and Tech.** _____

Prof. Dr. Necati Özkan
Supervisor, **Polymer Science and Technology** _____

Assoc. Prof. Dr. Yılser Devrim
Co-Supervisor, **Energy Sys. Eng., Atılım Uni.** _____

Examining Committee Members:

Prof. Dr. Head of the Ex. Committee Cevdet Kaynak,
Metallurgical and Materials Engineering, METU _____

Prof. Dr. Necati Özkan**,**
Polymer Science and Technology, METU _____

Assoc. Prof. Dr. Yılser Devrim,
Energy Systems Engineering, Atılım University _____

Prof. Dr. Göknur Bayram,
Chemical Engineering, METU _____

Assist. Prof. Dr. Cemal Merih Şengönül,
Manufacturing Engineering, Atılım University _____

Date: 22.05.2020

I hereby declare that all information in this document has been obtained and presented in accordance with academic rules and ethical conduct. I also declare that, as required by these rules and conduct, I have fully cited and referenced all material and results that are not original to this work.

Name, Surname: Enis Oğuzhan Eren

Signature:

ABSTRACT

DEVELOPMENT OF NON-NOBLE (Co-N/MWCNT) AND POLYBENZIMIDAZOLE-MODIFIED (Pt-PBI/MWCNT) ELECTROCATALYSTS FOR HIGH-TEMPERATURE PEM FUEL CELL APPLICATIONS

Eren, Enis Oğuzhan
Master of Science, Polymer Science and Technology
Supervisor: Prof. Dr. Necati Özkan
Co-Supervisor: Assoc. Prof. Dr. Yılser Devrim

May 2020, 103 pages

Due to the extremely high cost of platinum group metals, the development of highly efficient, non-noble electrocatalysts, especially for the oxygen reduction reaction (ORR) is essential for the commercialization. In recent studies, state-of-the-art Metal-N-C (Metal = Fe or Co) catalysts are considered as promising alternatives to expensive Pt/C catalysts because of their excellent electrochemical and physical properties. They can somehow provide decent mass activity and electrochemical performance with considerably low material and synthesis cost.

In this thesis, the main course is the development of a non-noble, high-performance Co-N/MWCNT electrocatalyst for high-temperature proton exchange membrane fuel cell (HT-PEMFCs) application, and the second course is the development of polybenzimidazole (PBI) modified carbon-nanotubes as a support material for platinum-based electrocatalysts to increase catalytic durability at elevated temperatures.

Upon completion of the studies, synthesis of the Co-N/MWCNT catalyst with a high-temperature pyrolysis method was successfully demonstrated by XPS, ToF-SIMS, XRD, Raman, and HR-TEM analysis. Results showed that the uniform dispersion of Co nanoparticles and the formation of active pyridinic Co-N_4 sites

were appropriately achieved. It is believed that the formation of stable Pyridinic-N sites could promote more electron pathways through the ORR, and increases the catalyst's stability. Rotating disc electrode (RDE) analysis demonstrated that the kinetics of the Co-N/MWCNT catalyst is sufficient enough to operate as a cathode for a typical PEM fuel cell operation. From the HT-PEMFC test results, at the 150°C and 160°C, the peak current/power density of the cobalt-based MEA was somehow higher than that of the commercial Pt/C. The only drawback is the stability issue at higher temperatures (170°C or more) in an acidic medium. Results partially confirmed that the Co-N/MWCNT catalyst could be the promising alternative to replace noble Pt/C catalysts at the cathode side.

In the sub-study, polybenzimidazole wrapped carbon-nanotubes and microwave-assisted reduction of Pt nanoparticles were successfully characterized by TGA, XPS, XRD, and TEM analysis. Modifying carbon-nanotubes through the polybenzimidazole film ensured fine (about 2 – 5 nm) and uniform dispersion of Pt nanoparticles. Cyclic voltammetry (CV) analysis concluded that the Pt-PBI/MWCNT catalyst had a 43 $m^2 \cdot g^{-1}$ of electrochemically active surface area (ECSA) to catalyze hydrogen oxidation, which is parallel to the literature but slightly lower than that of commercial Pt/C and Pt/MWCNT catalysts due to hydrophobic behavior of PBI molecules in an aqueous electrolyte. On the other hand, it has shown superior durability compared with the commercial Pt/C and Pt/MWCNT. After the 1000^{th} CV, it has retained almost 80% of its initial ECSA, which makes the Pt-PBI/MWCNT is much more durable than the Pt/C and Pt/MWCNT. However, HT-PEMFC tests indicated that the peak current/power density values of the PBI-modified catalyst were lower than that of commercial-grade Pt/C, suggesting that some balance between durability and performance has to be taken into consideration.

Keywords: Co-N/MWCNT, Pt-PBI/MWCNT, PEM Fuel Cell, High-Temperature, Polybenzimidazole

ÖZ

YÜKSEK SICAKLIK PEM YAKIT HÜCRELERİ İÇİN DÜŞÜK MALİYETLİ VE YÜKSEK PERFORMANSLI (Co-N/MWCNT) VE POLİBENZİMİDAZOL (PBI) İLE MODİFİYE EDİLMİŞ (Pt-PBI/MWCNT) ELEKTROKATALİZÖRLERİN GELİŞTİRİLMESİ

Eren, Enis Oğuzhan
Yüksek Lisans, Polimer Bilim ve Teknolojisi
Tez Danışmanı: Prof. Dr. Necati Özkan
Ortak Tez Danışmanı: Doç. Dr. Yılser Devrim

Mayıs 2020, 103 sayfa

PEM yakıt hücrelerinin birim maliyetini azaltma ve ticari kullanım alanlarının yaygınlaşmasını sağlama amacı ile yapılan çalışmalarda, mevcut platin grubu değerli metallerden hazırlanmış elektro-katalizörlerin, daha düşük maliyetli ve yüksek performanslı katalizörler ile değiştirilmesi oldukça önem arz etmektedir. Yapılan literatür araştırmaları neticesinde, karbon destekli Metal-N-C (Metal= Fe veya Co) tipi katalizörlerin, katot tarafında gerçekleşen oksijen indirgenme reaksiyonu (ORR) için ticari Pt/C'ye göre özellikle kütle aktivitesi ve kullanım ömrü anlamında yer yer daha iyi veya muadil sonuçlar verdikleri görülmüştür. Bu çalışmada, düşük maliyetli ve yüksek performanslı Co-N/MWCNT tipi katalizörün geliştirilmesi ve alt çalışma olarak da mevcut platin tabanlı elektrokatalizörler için polybenzimidazole polimeri ile modifiye edilmiş karbon nanotüp destek malzemelerinin kullanımı incelenecektir.

Çalışmalar sonucunda, Co-N/MWCNT katalizörün başarılı bir şekilde sentezlendiği ve istenilen morfolojik yapıda olduğu, XPS, ToF-SIMS, XRD, Raman ve TEM analizi ile gösterilmiştir. Testler sonucunda kobalt nano-parçacıklarının karbon-nanotüpler üzerinde düzenli biçimde dağınımı ve aktif piridinik Co-N_4 bölgelerinin oluşumu gözlemlenmiştir. Piridinik-N oluşumu

oksijen indirgenme reaksiyonu için daha fazla elektron yolu sağlarken aynı zamanda katalizörün stabilitesini de arttırmaktadır. Elektrokimyasal karakterizasyon, döner disk elektrot (RDE) metodu ile gerçekleştirilmiş olup bu test sonucunda da Co-N/MWCNT katalizörün, ticari muadillerine benzer sonuçlar vererek oksijen indirgenme reaksiyonları için kullanılabileceği gözlenmiştir. Yüksek sıcaklık PEM yakıt hücresi testi sonucunda, Co-N/MWCNT içeren hücrenin maksimum güç ve akım yoğunluğu değerleri, 150°C ve 160°C'de ticari muadilinden daha iyi çıkmıştır. Ancak literatüre göre bu katalizörlerin yüksek sıcaklıkta bazı stabilite sorunları yaşamaları mümkündür. Bu yüzden 170°C ve üzerinde performansı gözle görülür biçimde düşmüştür. Yapılan deneyler sonucunda, bu katalizörlerin, Pt/C katalizörlere kısmi olarak alternatif olabilecekleri görülmüştür.

Alt çalışmada ise, karbon-nanotüp destek malzemesinin polybenzimidazole (PBI) polimeri ile modifikasyonu ve Pt-PBI/MWCNT katalizörün mikrodalga yöntemi ile başarılı bir şekilde sentezlendiği TGA, XPS, XRD ve TEM analizleri ile gösterilmiştir. Dönüşümlü voltametri (CV) testi ile katalizörün elektrokimyasal aktif yüzey alanı 43 $m^2 \cdot g^{-1}$ olarak hesaplanmış, ticari muadili Pt/C ve Pt/MWCNT katalizör ile kıyas edildiğinde benzer veya nispeten daha düşük bir değere sahip olduğu belirlenmiştir. Düşük olmasının sebebi ise nanotüpleri saran PBI polimerinin hidrofobik özelliğe sahip olması ve bu yüzden elektrolit sıvının aktif yüzeylere temasının nispeten daha düşük olması gösterilebilir. Fakat 1000. Döngü sonunda, Pt-PBI/MWCNT katalizörün neredeyse ilk aktif yüzey alanının %80'ini koruduğu görülmüştür ve diğer katalizörlerden daha uzun ömürlü olduğu da belirlenmiştir. YS-PEM yakıt hücresi testi sonucunda ise Pt-PBI/MWCNT'den hazırlanan hücrenin, güç ve akım yoğunluğu değerlerinin ticari Pt/C katalizör içeren referanstan, tüm sıcaklıklarda daha düşük olduğu görülmüştür. Çalışmalar sonunda performans veya dayanıklılık arasında bir denge gözetilmesi gerektiği sonucu çıkmıştır.

Anahtar Kelimeler: Yakıt Pili, PEM, Co-N-C, Co-N/MWCNT, Pt-PBI/MWCNT

To the Universe

ACKNOWLEDGMENTS

I would like to thank my supervisors Prof. Dr. Necati Özkan and Assoc. Prof. Dr. Yılser Devrim for their guidance, advice, suggestions, and encouragement throughout the thesis studies. I would also like to thank the lab colleague Yağmur Budak for her valuable support during the processes.

This study was funded by The Scientific and Technological Research Council of Turkey (TUBITAK) under grant no of 119M018. Material characterizations were carried out in the Central Laboratory, Middle East Technical University. Electrochemical characterizations were carried out in the Hydrogen Energy and Fuel Cell Research Laboratory, Atılım University. GDEs were prepared by the support of TEKSIS Company (METU Technopolis).

Also, I would like to thank examining committee members, Prof. Dr. Cevdet Kaynak, Prof. Dr. Göknur Bayram, and Dr. Cemal Merih Şengönül for their valuable suggestions through the revising and improving the thesis manuscript.

Special thanks to Meriç Eren, Ergül & Mustafa Arif Eren, Ayşe Altunbaş, Ömer Burak Akgün, Mustafa Atik, Göksu Taşçeviren, and Mehmet Akpınar.

TABLE OF CONTENTS

LIST OF TABLES

TABLES

LIST OF FIGURES

FIGURES

LIST OF ABBREVIATIONS

ABBREVIATIONS

AFC	Alkaline Fuel Cell
BE	Binding Energy
BET	Brunauer-Emmett-Teller
CHP	Combined Heat and Power
CNT	Carbon Nanotube
CV	Cyclic Voltammetry
D-Raman	Dispersive Raman Spectroscopy
DFT	Density Functional Theory
DI	Deionize
DMAc	Dimethylacetamide
DMFC	Direct Methanol Fuel Cell
ECSA	Electrochemically Active Surface Area
EG	Ethylene Glycol
EW	Equivalent Weight
EXAFS	Extended X-Ray Absorption Fine Structure
FTIR	Fourier-Transform Infrared Spectrometry
GC	Glassy Carbon
GDE	Gas Diffusion Electrode
GDL	Gas Diffusion Layer
HOR	Hydrogen Oxidation Reaction
HR-TEM	High-Resolution Transmission Electron Microscopy
HT	High-Temperature
IPA	Isopropyl Alcohol
LSV	Linear Sweep Voltammetry
LT	Low Temperature
MCFC	Molten Carbonate Fuel Cell
Me-N-C	Metal-Nitrogen-Carbon

MEA	Membrane Electrode Assembly
MWCNT	Multi-Walled Carbon Nanotube
NASA	National Aeronautics and Space Administration
OCV	Open Circuit Voltage
ORR	Oxygen Reduction Reaction
PA	Phosphoric Acid
PAFC	Phosphoric Acid Fuel Cell
PBI	Polybenzimidazole
PEM	Proton Exchange (Polymer Electrolyte) Membrane
PEMFC	Proton Exchange (Polymer Electrolyte) Membrane Fuel Cell
PTFE	Polytetrafluoroethylene
RDE	Rotating Disc Electrode
RHE	Reference Hydrogen Electrode
SOFC	Solid Oxide Fuel Cell
SSA	Specific Surface Area
TAPy	Triazolopyridine
TGA	Thermogravimetric Analysis
ToF-SIMS	Time-of-Flight Secondary Ion Mass Spectrometry
WFR	Water Formation Reaction
XANES	X-Ray Absorption Near-Edge Structure
XAS	X-Ray Absorption Spectroscopy
XPS	X-Ray Photoelectron Spectroscopy
XRD	X-Ray Diffraction
YSZ	Yttria-Stabilized Zirconia

LIST OF SYMBOLS

SYMBOLS

L	Average crystallite size (nm)
$\lambda_{K\alpha}$	Wavelength of the X-ray (nm)
B	Full-width at half-maximum (FWHM) in radians
θ	Bragg angle (Degree or Radian)
ε	Strain induction
Q_H	Charge exchanged in the H_2 adsorbtion/desorption ($\mu C \cdot cm^{-2}$)
d_{32}	Sauter mean-particle diameter (nm)
η_{Pt}	Platinum utilization efficiency (%)
P_{max}	Maximum power density ($mW \cdot cm^{-2}$)
I_{max}	Maximum current density ($mA \cdot cm^{-2}$)
j	Overall current density ($mA \cdot cm^{-2}$)
j_k	Kinetic current density ($mA \cdot cm^{-2}$)
j_d	Diffusion limiting current density ($mA \cdot cm^{-2}$)
n	Number of transferred electrons
F	Faraday constant ($A \cdot s \cdot mol^{-1}$)
C_o	Saturated concentration of oxygen ($mol \cdot cm^{-3}$)
D_o	Diffusion coefficient of oxygen ($cm \cdot s^{-1}$)
η	Cell efficiency (%)
R_{ohmic}	Ohmic resistance (Ω)
η_{ohmic}	Ohmic loss (Ω)
σ	Conductivity ($S \cdot m^{-1}$)
K_c	Thermodynamic stability
ΔE	DFT formation energy (eV)
r_{PBI}	Thickness of the PBI layer (nm)
r_{MWCNT}	Radius of the carbon nanotubes (nm)

ω	Rotation rate (rpm or rad·s^{-1})
v	Kinematic viscosity (cm^2·s^{-1})
E_{onset}	Onset potential (V)
$E_{1/2}$	Halfwave potential (V)
T_g	Glass transition temperature (°C)
T	Temperature (K)
E_a	Activation energy (KJ·mol^{-1})

CHAPTER 1

INTRODUCTION

The population of the World and global energy consumption have doubled in the past 50 years. It is a fact that energy needs cannot be sustained by just the combustion of fossil fuels. And, this is not a real problem when compared with the management of CO_2 emissions, especially in an urban area. According to society's awareness, air pollution and the emission of greenhouse gases are considered to be the main reasons for global warming, and these problems have to be solved immediately. Kyoto Protocol, one of the most significant breakthroughs for this case, suggests that the reduction of emissions can be attained by renewable energy sources, CO_2 sequestration, and promotion to the existing highly efficient technologies. Investment costs of CO_2 sequestration are very high, and furthermore, the CO_2 sequestration is a complicated process. So, improving the efficiency of existing conventional systems and a new approach to developing clean energy systems are more convenient ways to handle emission problems.

In the past few decades, there has been significant progress over fuel cell science and technologies, which led them to become one of the most promising alternative energy sources. Despite having reasonable operating costs and high efficiency, they are still in their development infancy. To obtain commercially mature systems, governments and large corporations are still making huge investments over the commercialization of fuel cells. Recently, it has been shown that they can be used in various industries, including transportation, defense, stationary & portable power systems, and even cutting-edge space & rocket science technologies.

In this chapter, an overview of fuel cell systems, definitions, historical milestones, and working principles of the primary fuel cell types will be summarized.

1.1. Fuel Cell

A fuel cell is an electrochemical device that directly converts the chemical energy of a fuel into electrical energy through an oxidizing agent. Unlike the batteries, which are considered storage devices, fuel cells require a continuous source of fuel, oxygen/air to produce electricity, and electrodes are not the consuming materials. There are various types of fuel cells; however, they all work with the same principle. Anode, cathode, and the electrolyte are three main segments, and chemical reactions take place at the interface of these segments. Electrons move through an external circuit, and ions move through an electrolyte that placed between anode and cathode to produce direct current electricity [1].

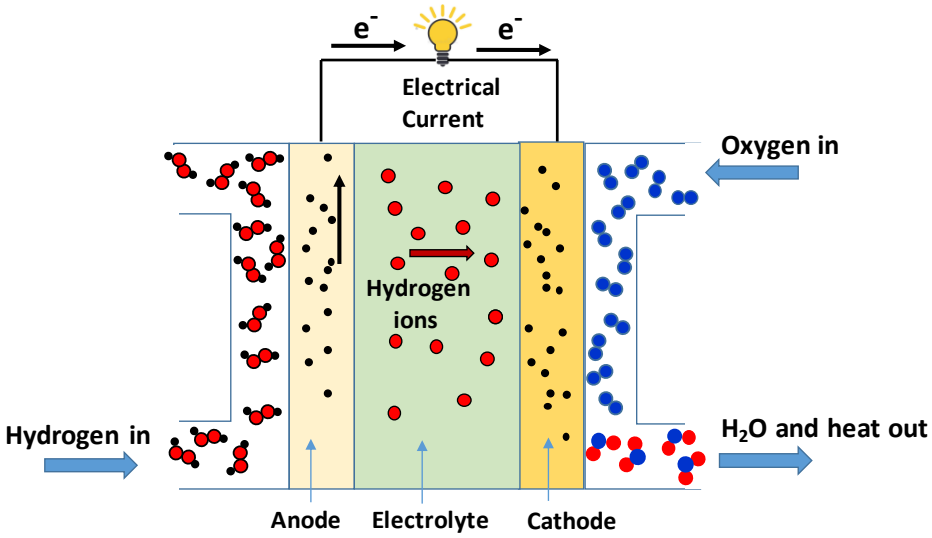

Figure 1.1. Schematic demonstration of a fuel cell.

The basic operation of hydrogen fuel cells is straightforward (Figure 1.1). At the anode electrode, hydrogen gas ionizes through the catalytically active sites and releases electrons and H^+ ions. This is the energy-releasing reaction.

$$2H_2 \rightarrow 4H^+ + 4e^- \tag{1.1}$$

At the cathode side, oxygen reacts with hydrogen ions and electrons obtained from anode to form water.

$$O_2 + 4e^- + 4H^+ \rightarrow 2H_2O \quad (1.2)$$

To generate power, both reactions have to occur simultaneously.

1.2. Historical Milestones

The fuel cell was invented by Willian R. Grove in 1838, and it was called "gaseous voltaic battery." At that time, Grove used platinum electrodes and sulfuric acid as an electrolyte. Reactant gases were hydrogen and oxygen. Interestingly, platinum was already known as a catalyst [2]. In 1882, Lord Rayleigh developed a new form of gas battery by increasing the active surface of the platinum catalyst within the electrode. In 1889, Mond and Langer invented the first prototype of a practical fuel cell. However, the main problem was the electrode flooding. In 1904, Haber and Bruner invested in direct coal fuel cells formed by iron electrodes in molten alkaline electrolytes. Hydrogen was formed by the coal in the molten caustic soda. It was concluded that the performance of direct coal fuel cell was abysmal because electrodes would be consumed quickly. In 1912, Baur and Ehrenberg worked molten silver as the cathode for coal fuel cell because it has excellent oxygen-dissolving properties. Baur and Preis developed the first solid oxide fuel cell in 1937, which used zirconia as an electrolyte because zirconia-based solid electrolytes were more manageable than the molten electrolytes. Operating temperatures vary between 500 °C - 1100 °C and depend on the ohmic resistances of electrolyte materials [3]. In 1946, Davtyan introduced the first molten carbonate fuel cell using a mixture of baked sodium carbonate, tungsten trioxide and sodium wolframate as an electrolyte. Based on the previous progress, the methanol fuel cell was introduced with the hope of oxidizing fuel directly in the 1960s [4]. In the beginning, sulfuric acid was used as an electrolyte, but nowadays, catalysts such as platinum alloyed with ruthenium show the best performance among all. In 1960, Grubb and Niedrach developed a fuel cell with a solid ion-exchange polymer membrane. This was the first prototype of today's proton exchange membrane fuel cell. To provide ionic conductivity, the membrane must contain water, but the management of flooding in the electrodes was not easy, though. Also, the life of the membrane was too short because of the corrosive environment at

the cathodic site. Spectacular improvement in membrane's service life was achieved when the Nafion® membrane of DuPont Company and PTFE membranes have been introduced. Today proton exchange membrane fuel cells are among the most promising clean energy sources for typical commercial applications because of the excellent efficiency and high-power density. Here (Figure 1.2) is the chronology about the history of fuel cells.

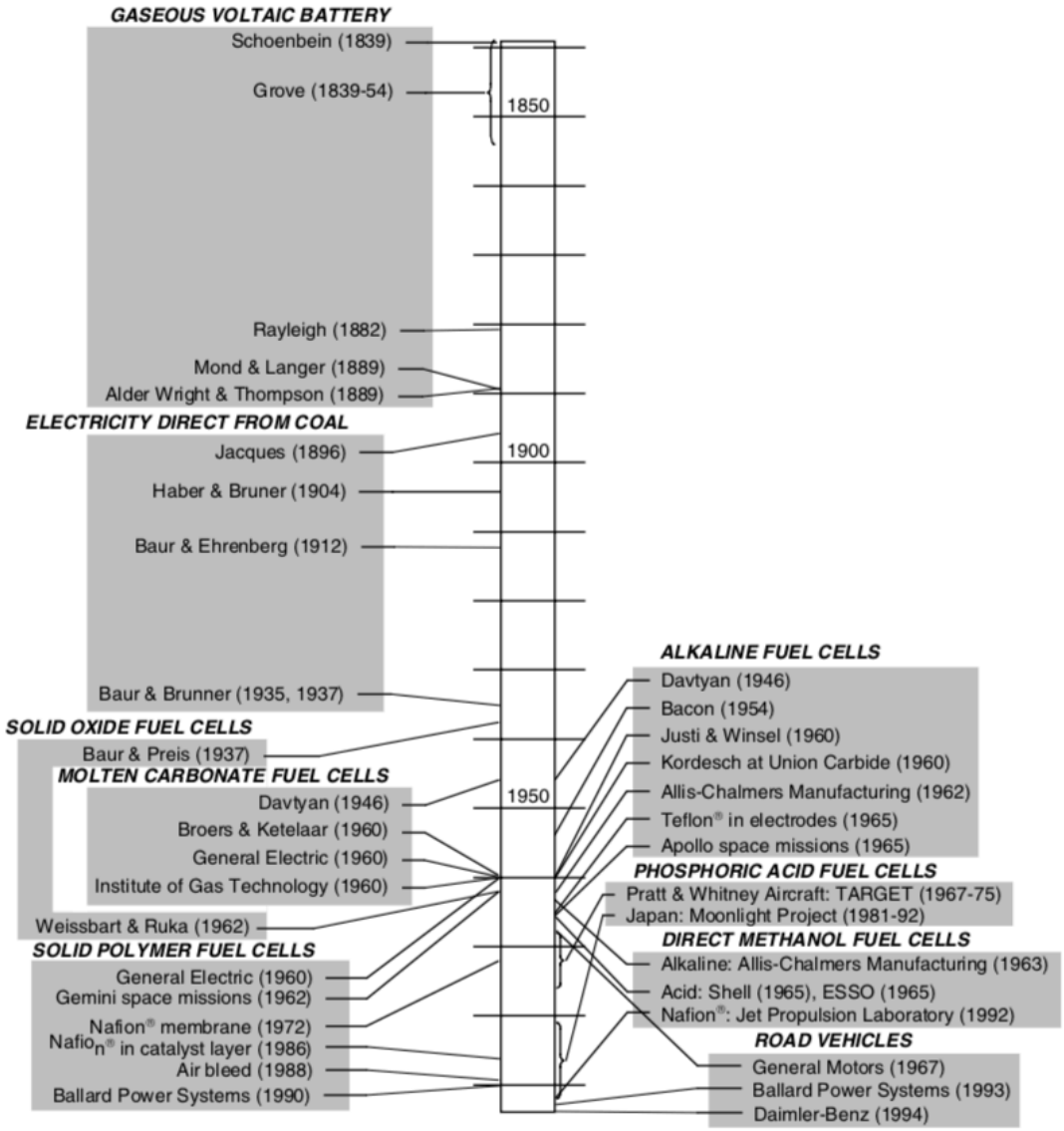

Figure 1.2. Chronology based on the introduction of fuel cell technologies [5].

1.3. Fuel Cell Types and Applications

The classification of fuel cells mostly depends on their electrolyte materials (Table 1.1). Each type of fuel cell has its own characteristics, which bring some benefits and shortcomings. Application fields of fuel cells are also dependent on various properties such as operating temperature, efficiency, power density, and useful life. In transportation and portable power generation industry, size and weight requirements are also very important.

Table 1.1. *Most Common Types of Fuel Cells*

Fuel Cell Type	Electrolyte	Charge Carrier	Operating Temperature	Fuel	Efficiency
Alkaline (AFC)	KOH	OH^-	60-120°C	H_2	35-55%
Proton Exchange Membrane (PEMFC)	Solid Polymer	H^+	50-160°C	H_2 (tolerates CO, CO_2)	35-45%
Phosphoric Acid (PAFC)	Phosphoric Acid	H^+	~220°C	H_2 (tolerates CO, CO_2)	40%
Molten Carbonate (MCFC)	Lithium and Potassium Carbonate	CO_3^{2-}	~650°C	H_2, Hydrocarbons (tolerates CO, CO_2)	>50%
Solid Oxide (SOFC)	Solid Oxide (Yttria, Zirconia)	O^{2-}	~1000°C	H_2, Hydrocarbons (tolerates CO, CO_2)	>50%

1.3.1. Alkaline Fuel Cell (AFC)

Alkaline fuel cells consume pure hydrogen and oxygen to produce electrical energy. In the alkaline fuel cell, overall cell reactions are the same, but the principle is different. At the cathode, Hydroxyl (OH^-) ions move toward anode to form water. Two electrodes are separated with the porous matrix filled with an alkaline solution such as potassium hydroxide (KOH). KOH solution cannot tolerate even a small amount of CO_2 impurities. To prevent from "poisoning effect" (conversion of KOH to K_2CO_3), AFCs must only be fed by pure hydrogen and purified air. Having low operating temperatures (~90°C) and being more efficient than other fuel cells with an acidic

electrolyte are the main advantages of AFCs. AFCs have been used by NASA since the Apollo-Series missions and on the space shuttles. Because pure hydrogen and oxygen are already available in these systems, the adaption of AFCs is quite simple and cost-efficient.

1.3.2. Phosphoric Acid Fuel Cell (PAFC)

PAFCs are considered the first generation of modern fuel cells. The electrolyte is a liquid phosphoric acid (H_3PO_4) saturated in silicon carbide (SiC) matrix, and operating temperature varies from 150°C to 210°C. Unlike the other fuel cells, PAFCs are more tolerant of CO_2, and even small amounts of CO (about 1%) [6]. Early applications of PAFCs were based on the stationary power systems, and today there is only one company that manufactures commercially available PAFCs. When compared to PEMFCs, PAFCs are relatively large, heavy, and less powerful. So, adaptation to the transportation industry is relatively ineffective. Furthermore, PAFCs have very long start-up time, and they also require preheating before the operation, which makes this type of fuel cells are more suitable for the stationary power generation.

1.3.3. Molten Carbonate Fuel Cell (MCFC)

Molten carbonate fuel cells are composed of alkali metal carbonates as an electrolyte such as molten potassium, sodium, and lithium carbonate (K_2CO_3 - Na_2CO_3 - Li_2CO_3). The electrolyte is coated over a porous ceramic matrix made of lithium aluminate ($LiAlO_2$) or strontium titanate ($SrTiO_3$). The typical operating temperature of MCFCs is approximately 650°C. Due to high operating temperatures, less “poisoning effect” observed in the fuel cell so that MCFCs can operate with a variety of different fuels, including reformate gases. Moreover, MCFCs do not need noble metals as a catalyst. Current densities of MCFCs are somewhere between PAFCs and SOFCs. Having the liquid electrolyte, carbonate atoms are consumed at the anode, and injection of CO_2 to the cathode is required to provide balance. Due to the high operating temperatures, MCFCs are also more vulnerable to corrosion. Another disadvantage of MCFCs, they cannot tolerate more than 1-5 ppm of sulfur without suffering a significant amount of

performance loss [7]. Today, MCFCs are widely used in large stationary power generation applications.

1.3.4. Solid Oxide Fuel Cell (SOFC)

Due to the very high operating temperatures (500°C - 1000°C), SOFCs have solid oxide material as an electrolyte. The most typical electrolyte is yttria-stabilized zirconia (YSZ), which is a great ion conductor at elevated temperatures. SOFC geometry is either tubular or planar (Figure 1.3). To provide thermal shock resistance, tubular geometry must be used. On the other hand, planar geometry offers an advantage in terms of power density and ease of cell manufacture. Today, ongoing researches are generally focused on developing intermediate and low-temperature applications of SOFCs. This would enable the use of cheaper materials with better properties also improves commercialization by increasing efficiency. SOFCs can be used for both stationary and portable power generation as an auxiliary power unit [8].

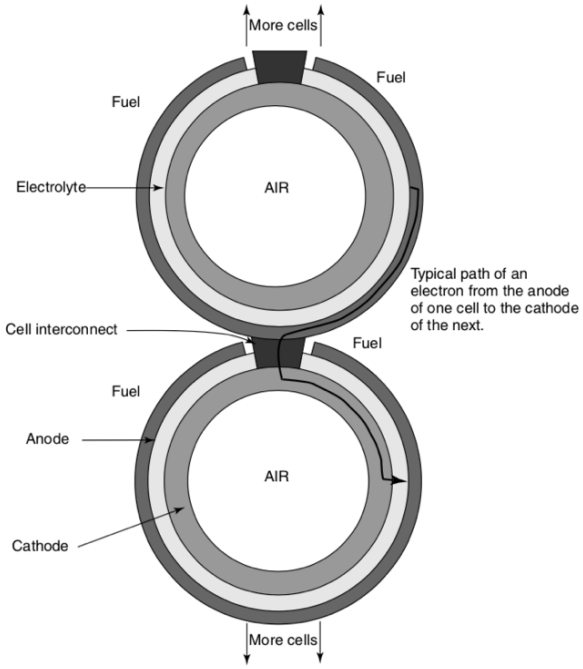

Figure 1.3. End view of a tubular type of SOFC [8].

1.3.5. Proton Exchange Membrane Fuel Cell (PEMFC)

Proton exchange (polymer electrolyte) membrane fuel cell is a fuel cell type with relatively low operating temperatures and a unique proton-conducting polymer electrolyte. For the extensive information, see Chapter 1.4.

1.4. Fundamentals of PEM Fuel Cells

Proton exchange (polymer electrolyte) membrane fuel cells (PEMFC) were developed in the 1960s by NASA for the usage in their space applications. Using the solid ion-conducting polymer as an electrolyte, they have relatively low operating temperatures (as low as 50 – 60ºC) compared with the other types of fuel cells. An extremely thin layer of the anode and the cathode are bonded onto each side of the polymer membrane, forming the membrane electrode assembly (MEA). These membrane electrode assemblies are connected in series with using bipolar plates to form large fuel cell stacks. Having relatively compact MEAs, short start-up times, and low operating temperatures, PEMFCs are particularly suitable for portable applications.

In the early applications, the average lifetime of a single PEMFC was only 500 hours. Moreover, permeability and durability of the membranes were very poor. However, at that time, the performance of fuel cells was relatively sufficient for those limited space & rocket science applications. Considering the commercialization of PEMFCs, the introduction of Nafion® by DuPont made a huge breakthrough. Since then, Nafion® membranes became an industrial standard for PEMFCs. On the electrode side, platinum group metals have become the leading metals for catalyzing oxidation and reduction reactions due to their spectacular electrocatalytic properties. Cost per kW was the main obstacle for the commercialization of PEMFCs, and it is strictly dependent on MEA because of the valuable platinum group metals and PTFE based membranes. Over the few decades, thanks to the improvements in materials science, the load of platinum group metals on catalyst layers reduced from 28 $mg \cdot cm^{-2}$ to 0.2 $mg \cdot cm^{-2}$ or less with a spectacular renovation on cell performance [9]. Furthermore, these developments have brought the current densities up to 1000 mA cm^2 or more, resulting in much-improved power density.

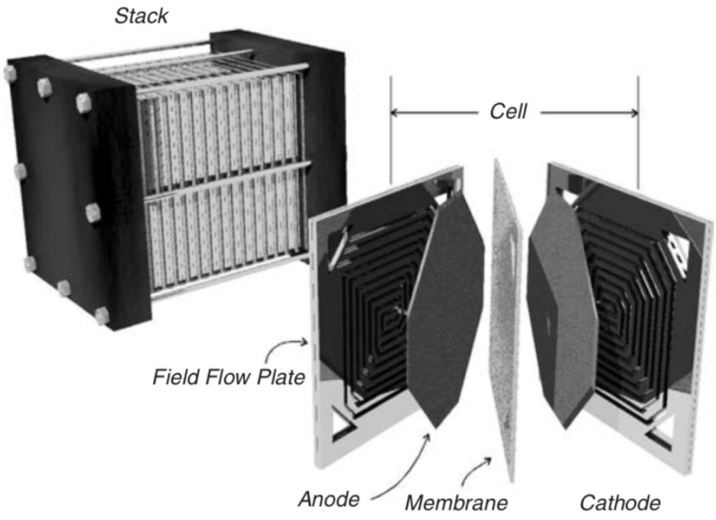

Figure 1.4. Typical PEMFC components and fuel cell stack [10]

Today, PEMFCs are possible energy sources for a wide range of technological and transportation applications, starting from a few watt systems to hundreds of kilowatts. Among them, driving the energy for transportation and industrial CHP systems are the most promising and efficient applications. Within this vast range of fields, there are still several shortcomings that affect the commercialization of PEMFCs. Typical PEMFC components are summarized in Figure 1.4.

1.4.1. How the PEMFCs Work?

Here are the electrochemical reactions take place at the anode and the cathode, respectively;

$$2H_2 \rightarrow 4H^+ + 4e^- \ (E_r = 0\ V) \tag{1.3}$$

$$O_2 + 4e^- + 4H^+ \rightarrow 2H_2O\ (E_r = 1.23\ V) \tag{1.4}$$

Upon completion of the oxidation reaction, protons migrate through the ion-conducting membrane and reach the cathode side to form water by giving electrical energy and heat. To provide thermal management, anode electrode must be porous enough to remove generated heat from the reactive zone easily. At the cathode,

reactions become more complicated due to the formation of water and kinetic limitations, resulting in significant performance loss. The formation of water enables the steady formation of vapor and droplets at the catalytic pores and restricts gas access to the reactive zone. Moreover, oxidant used in most of the applications is not pure oxygen but air with a high amount of inert gas, meaning, the only low fraction of oxidants has to reach catalytic sites. Moreover, another critical problem is the humidifying of the proton-conducting membrane. Due to the nature of the ion-conducting membranes, they have to be well humidified to migrate protons properly. There is a formation of water flux from anode to cathode related to the migration of protons, which results in depletion of water from the anode interface of the membrane. So, the humidity is generally provided by pre-humidifying reactants [10]. Considering the volume of the real oxidants; efficiency, humidity, and water management became some of the most challenging issues in PEMFCs.

1.4.2. Voltage Efficiency and Power Density

When no current is drawn, theoretical open cell voltage (OCV) would be 1.23 V, but the actual operating voltage is lower due to some parasitic reactions. A small amount of hydrogen oxidized at the cathode and compete with the oxygen reduction reaction resulting in significant loss of open-circuit voltage (OCV). Also, inevitable corrosion reactions take place at the catalysts layer, mostly in the carbon support material. When current is drawn from the cell, these reactions are dominated by the actual electrochemical reactions. So, lower cell voltage than the theoretical value is obtained. The electric power density produced by MEA is directly related to voltage and the current density. At the OCV, power density is zero. It increases with the increasing current density to its maximum value, which is one of the most important factors that represents the quality of MEA. Beyond the maximum point, there might be a sharp decrease in cell voltage, and this surpasses the increase in current density.

Cell efficiency (η) is related to the cell voltage. The following equation (Eq. 1.5) shows the maximum thermal efficiency of an electrochemical cell at the elevated temperatures.

$$\eta_{max} = \frac{n_e F E^{\circ}}{HHV} \quad (1.5)$$

In transportation industry, maximum power is required. Considering the rapid drop of power density, operating cell voltage should be somewhere between ~0.7 – 0.8 V. In an application where the fuel efficiency is the primary importance, such as stationary application, the cell has to operate at much higher values than these.

1.4.3. Ohmic Loss

A combination of cell components creates an electronic resistance in a typical fuel cell, while proton transport creates an ionic resistance. These two provide ohmic losses during the transport of electrons and ions. Influence on the cell performance can be classified by numerical fitting methods of ohmic correction data obtained from electrochemical impedance spectroscopy and current interrupt. The total internal resistance of fuel cells is critical when considering the reliable lifetime of a commercial system. Here (Figure 1.5) is the typical circuit model of a porous electrode used to model the EIS data.

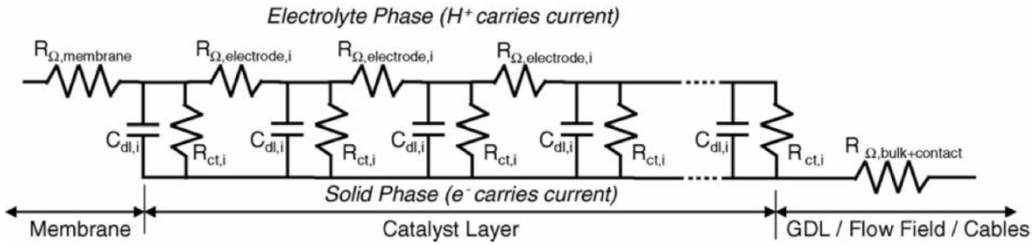

Figure 1.5. Equivalent circuit of a PEMFC represented by transmission line model [11]

Moreover, the ohmic loss is also dependent on contact resistances, materials, and operating variables such as temperature, pressure, and current density. Among all, the ionic losses can be considered the most important one. Simplifying the total ohmic loss to ionic loss could give a more practical approach for understanding the mechanism. The main requirement for reducing the ohmic loss is to increase the ionic

conductivity. To calculate fuel cells resistance, a cross-sectional area of conductor, length, thickness, and conductivity properties are required. R_{ohmic} can be calculated by:

$$\eta_{ohmic} = iR_{ohmic} = jA_{cell}\left(\frac{L_{thick}}{\sigma A_{fuelcell}}\right) = \frac{jL_{thick}}{\sigma} \quad (1.6)$$

From the equation above, it is concluded that the adjusting thickness and increasing the conductivity are the most practical ways to reduce ohmic losses [12].

1.4.4. Mass Transport Effect

Onset at the end of the linear region of the current/potential curve is marked as a mass transport limitation, which is a quite complex function and cannot be described by a simple equation. To understand the mechanism, much extensive information required related to the electro-osmotic drag and the total water balance kinetics (Figure 1.6). A concentration gradient is a driving force, and there is a back diffusion of water along the concentration gradient. Net crossover of water is related to the electro-osmotic drag of migrating protons. In a typical PEMFC, gases that supplied to the cathode side are not pure oxygen, it is artificial or natural air, and it might contain a high amount of inert gases. So, another mass transfer effect, called nitrogen blanket effect, is directly related to the supplied air, and it is one of the primary reasons for limiting diffusion of oxygen in the catalyst layer. Moreover, the formation of water droplets also blocks the gas access. The number of water molecules and protons transported through the membrane directly depends on the membrane material properties and has a substantial impact on the mass transport behavior of the MEA. Also, developing corrosion resistance catalyst materials, especially working in an acidic medium, may mitigate mass transport losses.

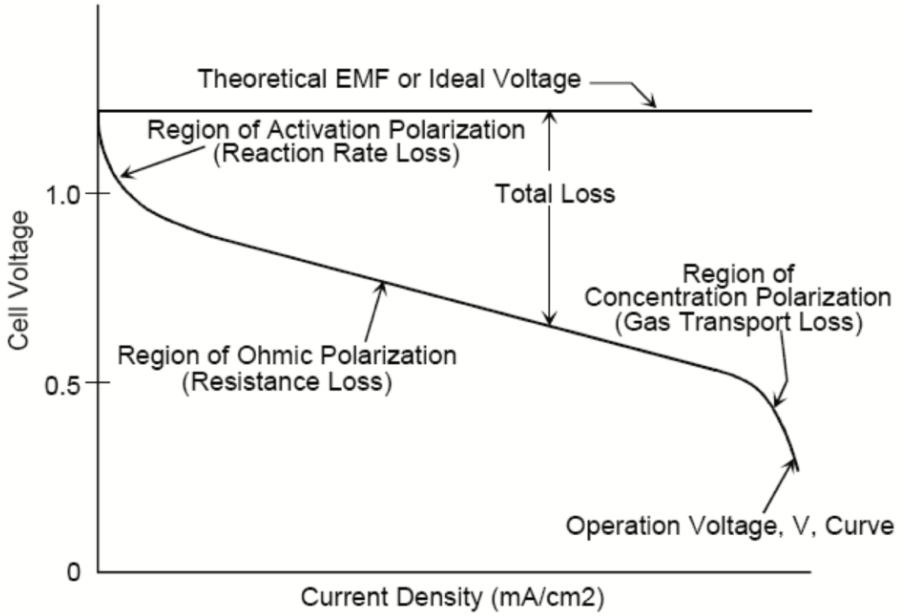

Figure 1.6. Ohmic and transport loss can be observed from the typical cell voltage vs current density curve of PEMFC [13].

1.4.5. MEA Components

The development of a proper membrane electrode assembly (MEA) is one of the most critical processes for bringing fuel cell prototypes into a final product. A high-performance MEA must sustain high power density by providing excellent durability and cost-efficiency. To understand the importance of a MEA concept, it is better to understand the mechanisms of each component. In the following section, the definition of components, working principles, materials, and typical challenges will be explained. In a typical PEMFC, MEA will consist of the ion-conducting polymer membrane, anode and cathode electrodes, gas diffusion layers, and sealing materials.

1.4.5.1. Membranes and Ionomers

Using solid polymer material as an electrolyte has brought so many advantages in fuel cell applications. They are excellent electric insulator while allowing high proton transport and current densities. Solid polymer electrolyte does not degrade, redistribute easily. Considering the tolerance to rapid load changes, they are very

suitable for both mobile and stationary applications. PEMFCs were first developed for the space program. In the early forms, polystyrene sulfonic acid, which humidified by reactant gas, was used as a membrane at an operating temperature of 21°C. At that time, the duration requirements for a typical mission was up to two weeks so that this polymer can ensure the necessary program requirements. However, for the more extended operations, durability problems came out until the perfluorinated membranes have been introduced.

1.4.5.2. Perfluorinated (Nafion®) Membranes for LT-PEMFCs

In the late 1960s, DuPont introduced a state-of-the-art polymer electrolyte material under the trade name Nafion® which is based on polytetrafluoroethylene (PTFE) with side chains consists of perfluorinated vinyl polyether (Figure 1.7). Moreover, sulfonic acid groups at the end of the chains give the cation exchange capability. Material is still one of the best suitable for low-temperature applications with over 60,000 hours of service life. Mass of polymer per active sulfonic group is called equivalent weight (EW), and it is a significant factor in describing the ion exchange capability of a typical polymer membrane. EW values of early commercial membranes were relatively high, 1200, or higher, negatively affected the proton exchange capacity. In the late 80s, some other companies such as Dow Chemical lowered this value to almost 800 but with a dramatic decrease in durability.

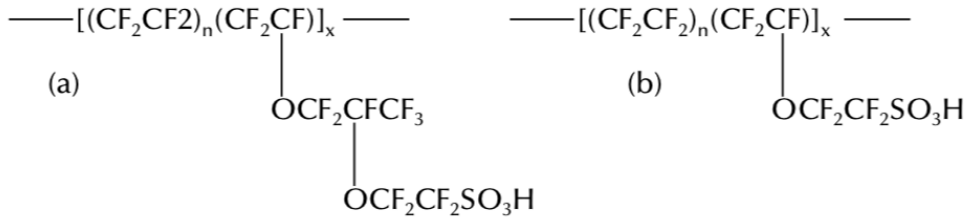

Figure 1.7. Typical perfluorinated polymers from DuPont (a) and Dow Chemical (b). Values "n" and "x" varies with different equivalent weight (EW) values [14].

To this date, DuPont remained the sole provider for Nafion® membranes, and it is still the most preferred membrane material in use for low-temperature PEMFC applications. Under the 80°C operating temperature with proper humidification, typical Nafion® 117 (1100 EW and 178 μm) has approximately 0.17 Scm^{-1} of ionic conductivity, and 0.105 Ωcm^2 of specific resistance [14]. Today thickness of a commercial membrane varies from 25 to 250 μm, and it is directly related to permeability. Reducing thickness may increase performance but reduce the durability and may lead to reactant crossover, especially for direct methanol fuel cells. As mentioned before, the performance of an ion-conducting polymer strongly depends on humidification. Above the 100°C of operating temperatures, thermal stability issues cause immediate dehydration that results in an extreme loss on cell performance. In this manner, thinner membranes may bring some shortcomings. Over the few decades, there has been significant progress over the development of the optimum polymer membrane by whether improving the existing Nafion® or introducing a brand-new cutting-edge material.

1.4.5.3. Alternative Membranes

Nafion® has become the industry standard in the PEMFC industry, but there are also some limitations related to its value, performance at elevated temperatures, and humidification requirements. Today unit cost of fully perfluorinated membranes ranges from 500 to 1000 $USD \cdot m^{-2}$. Considering the commercialization for systems, they are still way expensive than the target. The high purchase price of these materials forces people to interest and develop cheaper materials. In this manner, rather than developing new material, improving the existing ones is still the most preferred way. One example is the radiation grafted membrane. Crosslinking the regular perfluorinated membranes with a functional side chain by beta or gamma radiation may reduce the cost and improve the kinetics for operating temperatures below 60°C. However, these types of modifications generally make membranes more fragile to oxidative attacks and decrease durability. Another approach for reducing the cost is the use of hydrocarbon-based membranes. Hydrocarbon membranes provide sufficient performance for low-temperature applications, but their useful service life

will not exceed 2500 hours at 60°C. Despite the low cost of procurement, the idea of using hydrocarbon membranes became unpopular because they have to be replaced at a specific interval. Composite approaches such as woven or non-woven matrix with perfluorinated membranes are still the most promising ways to improve the performance. This type of ionomers exhibits excellent strength and ionic conductivity. Today, W.L Gore has introduced a brand-new PTFE based composite membrane under the trademark GoreSelect®. These extremely thin membranes (5-20 μm) consist of porous PTFE impregnated with a Nafion® solution. PTFE has low shrinkage under dehydration and excellent mechanical properties. Having relatively high resistance will not create a significant problem because the membranes are extremely thin; it will balance easily. PTFE matrix also allows the membrane to act more hydrophobic. Combining it with the thickness, the water management issue becomes easier than that in conventional Nafion® even at elevated temperatures. The priority of this type of composite applications is to improve membrane performance rather than reduce its cost. Recently, Nafion® membranes have been modified using molten acidic salts to increase proton conductivity at above 150°C even under anhydrous conditions, which enable their usage in high-temperature applications. Today, there are also lab-scale studies over combining the Nafion® membrane with Pt and TiO_2 nanoparticles to catalyze the recombination of hydrogen and oxygen for providing internal humidification [15]. Over the last decades, polybenzimidazole (PBI, Figure1.8) membranes have also become the sole material for the high-temperature PEMFC applications. Nowadays, over 150°C, proton conductivity can only be sustained through the acid-doped polybenzimidazole membranes. See section 1.5 for extra information.

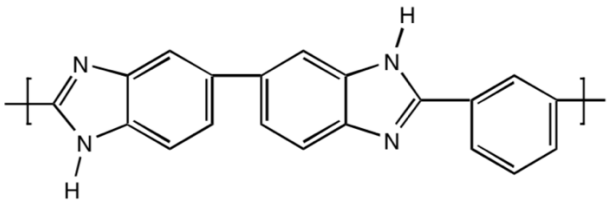

Figure 1.8. Molecular structure of polybenzimidazole (PBI) [15].

1.4.5.4. Gas Diffusion Layers

In a fuel cell, hydrogen and air/oxygen reactants have to reach the reactive zone within the electrode. Electrode substrate or gas diffusion layers (GDL) can provide this mission by distributing gases uniformly while removing the excessive heat and liquid from the anode and the cathode through the link with the adjacent cells and cooling plates. In modern fuel cells, allowing reactants to directly reaching the catalyst layer without an electrode substrate material is not a preferred way to feed the system. As seen in Figure 1.9, gas flow through the specific landing areas of open gas channels has to be diffused and uniformly distributed along with the catalyst layer.

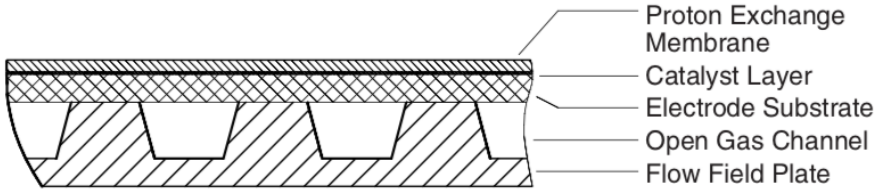

Figure 1.9. Cross-section of MEA in contact with the electrode substrate and open gas channels [16].

Today number of different materials have been used as fuel cell gas diffusion layers. Carbon fiber papers and woven carbon clothes are the most famous backing materials for this purpose. Carbon fiber papers have excellent rigidity and electronic conductivity. On the other hand, clothes are more flexible with good conductivity and possible advantages due to improved water management. Another potential low-cost approach is attaching electrically conductive fillers such as carbon black to non-woven material. To enable two-phase flow, they are usually covered with a wetproofing agent such as PTFE [16].

1.4.5.5. Fuel Cell Electrocatalysts

The most important sectors of a typical fuel cell MEA are two electrocatalyst layers where the vital electrochemical reactions such as hydrogen oxidation (HOR), oxygen reduction (ORR), and water formation (WFR) take place. They are bonded on both sides of the membrane with an essential role. Today, providing an excellent

electrochemical activity, good durability, and cost-efficiency are the absolute requirements for the catalyst design.

1.4.5.5.1. Anode Electrocatalysts

When considering the oxidation of dihydrogen, noble metals such as Pt and Pd perform better and show high stability in an acidic environment. Furthermore, using pure H_2 as a fuel, the operation can be sustained even with a deficient level of Pt loading on the anode. Comparing with the non-noble alternatives, Pt-based anode catalysts are still the leading candidate and the only commercial material for a PEM fuel cell application. However, the increase in demand for platinum and other noble metals brings increasing in power generation cost. Reducing the Pt loadings on catalysts while improving the catalytic activity is possible with the new generation support materials. Increasing the surface area by carbon material provides better dispersion of Pt on the catalyst layer. In the beginning, carbon powder products of Cabot and Ketjen became the popular support materials because of the higher BET surface areas and adsorption properties. Nowadays, improvement in material science brings the introduction of more sophisticated and better support materials such as functionalized and aligned carbon nanotubes, graphene nanoplatelets. Using the high-tech support materials and functionalize them may also improve the useful life of the catalysts. A commercial PEMFC is expected to operate for tens of thousands of hours, so the kinetics of the chemical degradation is very important, especially in an acidic environment. Modifying the carbon support material with some polymers such as polybenzimidazole, PTFE, and also bimetallic catalyst layers can be considered some of the lab-scale works in this area. Wrapping multi-walled carbon nanotubes with a thin film of a polymer may increase durability in an acidic environment. Furthermore, it may provide better dispersion of metallic Pt over support material and enhance catalyst activity.

Hydrogen produced by the hydrocarbons contains some amount of CO and CO_2. CO poisons active sites on the Pt catalyst that results in a dramatic decrease in catalyst performance such as H_2 oxidation. To overcome this problem, reformate-tolerant

electrocatalyst must be developed. Alloying Pt with Ru, Sn, or Mo will provide high tolerance to CO gases in the anode side. Among them, Pt-Ru bi-alloy has shown that the best tolerance at higher potentials. CO tolerance maintained by the electro-oxidation of the catalyst surface.

1.4.5.5.2. Cathode Electrocatalysts

In the cathodic side, the reactions and their kinetics are far more complicated than that of the anodic side. Both the oxygen reduction (ORR) and water formation (WFR) reactions have their limitations to be surmounted. In an acidic environment, almost all of the noble metals can be chosen for the oxygen reduction reaction. Still, when comparing with the hydrogen oxidation, the catalyst is at least 10^6 times less active, even using the commercial Pt/C [23]. So, the main limitation of fuel cell efficiency is the higher overpotential generated from oxygen reduction. Increasing electron transfer pathways, just like the anode catalysts through the increasing active surface area, maybe the solution. Today, Pt with carbon support catalysts are far the most preferred materials used for the oxygen reduction reaction. However, there has been significant progress over the usage of non-noble materials for cathodic reactions. Nowadays, metal-nitrogen-carbon based catalysts are considered the most promising candidates for ORR because of the active pyridinic nitrogen sites that are placed along with the carbon support materials. Transition metals (Co, Fe, and Ni) are considered the leading candidates for such catalyst. Not also improving the cell performance but also decreasing the fuel cell operating costs is possible by eliminating Pt group noble metals from the cathodic site. In this thesis, the development of a cobalt-based nitrogen-carbon complex as a cathode catalyst, especially for the oxygen reduction reaction and demonstration of its performance in specific HT-PEMFC operation conditions, are the main courses. Because of the complexity of the Me-N-C structure, understanding the mechanisms and kinetics are still in the preliminary phase. Thus, this requires extensive knowledge over synthesis and characterization processes. Further information about the mechanisms of Me-N-C catalysts, synthesis, treatment methods, other properties, and shortcomings will be discussed in Chapter 2.

1.4.5.6. Preparation of Membrane Electrode Assemblies (MEAs)

Applying the catalyst layer directly on either side of the membrane and then sandwiched with the gas diffusion layers by the hot-pressing method is the most common way of putting MEA together. Alternatively, catalysts can be applied directly onto the gas diffusion layers before assembling the membrane. As prepared catalyst inks with a specific platinum loading ultrasonically sprayed onto the backing layer of GDLs and bonded to the membrane. To achieve an excellent ionic contact, the solubilized form of the membrane has to be added into the ink as a binder. For example, it has been shown that the Nafion®, with the 15 wt% loading in ink, provides the right balance for an ionic conductivity [17].

1.4.6. Fuel Cell Stacks

To form a fuel cell stack, the as-prepared number of MEAs should be put together with an efficient design to reduce ohmic losses and sufficient access of reactants. Flow field plates are employed to feed the reactants. Typical fuel cell stack may include flow field plates, cooling elements, current collector plates, and possibly humidifiers.

1.4.6.1. Bipolar Plates

Generally, flow field plates are made of graphite-based materials (Figure 1.10). These plates have high electronic and thermal conductivity with a thickness of several millimeters. However, fabrication and design challenges are the main issues in preparing efficient flow field plates. Flow field plates can be machined for use on either side of the stack; the term bipolar plate is used in this context. Current conduction, heat conduction, control of gas flow, and by-product (water) removal are the main tasks of a flow field plate.

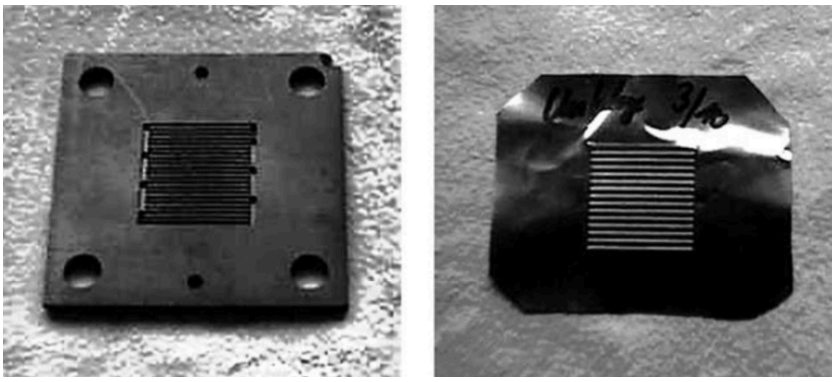

Figure 1.10. Sample of two flow field plates; machined graphite (left) and low-cost metal (right) [19].

So, the design and selection of build material are fundamental issues considering these critical tasks. A combination of fluid-dynamic modeling with experimental evaluation may provide achievement of the right structure for bipolar plates, especially considering the complexity of heat and water removal processes. Compression energy is required to drive the reactants through the flow field structure; furthermore, removing water is a challenging process due to two-phase flow. The primary solution to these problems is to construct a parallel gas channel and increase the pressure difference between plate inlet and outlet. However, the most important shortcoming of a conventional parallel plate design is the coalescence of water droplets at the cathode, resulting in blocking some gas channels and inactivation of MEA. The so-called serpentine flow field (Ballard) and its improved derivatives (General Motors) are believed to overcome this blockage by differentiate pressure between inlet and outlet, and force stagnant water out of channels (Figure 1.11).

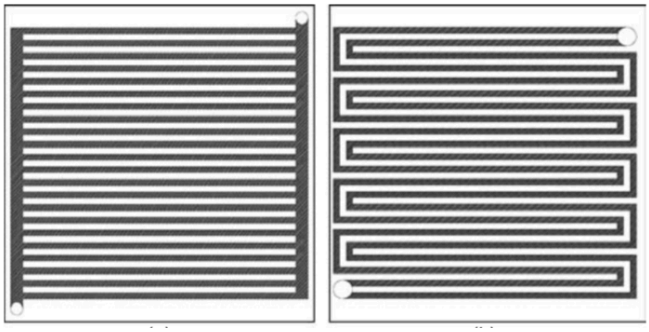

Figure 1.11. Conventional parallel gas channels (left) and serpentine flow field design (right) [18].

1.4.6.2. Humidifiers and Cooling Plates

Two other components in fuel cell stacks are humidifiers and cooling plates. Cooling is very important to maintain the required operating conditions for a given fuel cell stack. Considering the complexity of heat transfer mechanisms, isothermal conditions, or temperature gradient may have a positive effect on water removal. In an automotive application, liquid cooling is required because high and stable power density has to be sustained for long-term operation. Internally cooled bipolar plates are the only solution for removing the excessive heat from large stacks, whereas in very short stacks, cooling the only end plates is reasonable. In less demanding applications, air cooling is sometimes applied. To provide cooling, reactant air is supplied by a fan rather than a natural aspiration. This type of cooling does not have a long-term performance data, though [19].

Bubblers, fiber bundle humidifiers, and water evaporators are the most common types of humidifying agents in the PEMFC industry. Simplest one is the bubbler, which has a wash bottle design and directly passes through the liquid. This primitive approach allows only poor control of humidification, and it is not suitable for complex stacks. Another approach is using a membrane humidifier. A semi-permeable membrane isolates the water-filled compartment from the compartment with the reactant gases. During the transfer of gases through the membrane, it creates a counter-flow arrangement, and increases the humidity continually [20]. Nowadays, combining humidification and cooling processes are also prevalent, and at least three companies have patented these concepts as cooler-humidifier plates. These plates provide heat removal with the flow of water on one side and moisten the reactant gases on the other side. Evaporation of water at the humidification side may also provide additional cooling.

1.4.7. High-Temperature PEM Fuel Cells

Despite storage and pressurizing challenges, H_2 gas is still the leading reactant for most of the fuel cell applications. Furthermore, considering the unit cost per amount of energy, pure H_2 fuel can be regarded as a massive drawback to the

commercialization of fuel cell applications. Over a decade, there has been significant progress over the idea of using the different compositions of reformate gases as a single reactant instead of using pure H_2. However, the operating temperatures of traditional PEMFC's are low (~60-80°C) and cannot provide the essential impurity (carbon monoxide (CO)) tolerance, which brings the inefficiency. In a typical HT-PEMFC, higher operating temperatures improve kinetics, CO tolerance, heat, and water management. On the other hand, the complexity of the operation and stability of MEA at elevated temperatures force people to use more expensive materials. For example, over 150°C, proton conductivity can only be sustained through the acid-doped polybenzimidazole membranes. Combining the temperature and acidic environment, corrosion at the active sites and durability become the main problems that need to be overcome. Developing electrocatalysts with an improved electrochemical property, long term stability, and corrosion resistance are vital for HT-PEMFCs.

The main component and the leading materials are the phosphoric acid doped-PBI (polybenzimidazole) membranes which make HT-PEMFCs are operational at elevated temperatures. They are able to operate at temperatures up to 200°C. Today, in a typical HT-PEMFC, the recommended lower boundary of operation temperature is 120°C to avoid the formation of liquid water. In contrast, the recommended upper boundary is 180°C to avoid harsh degradation. Switching to a higher temperature reduces the resistance of the charge and proton transfer, resulting in an increase in the efficiency of kinetic reactions. To minimize the CO poisoning effect, more CO tolerant catalysts have to be developed. Modifying the Pt/C with Ru or developing new state-of-the-art metal-nitrogen-carbon catalysts are very promising and can be the solution to this problem in the near future. On the other hand, CO tolerance of current commercial Pt/C catalysts is raised by as much as 3% to 5% depending on the temperature and loading (Figure 1.12) [21]. Because at higher temperatures above 140°C, CO tolerance increases, and CO adsorption on Pt is associated with high negative entropy. In practice, in a hydrogen reformer system, the gas composition can be adjusted to improve performance, tolerate impurities, and lower the power generation cost.

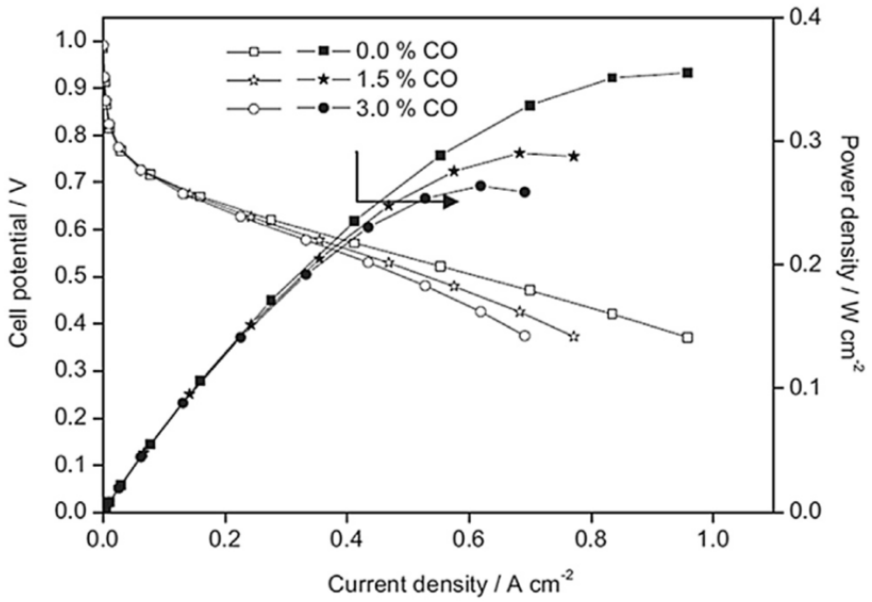

Figure 1.12. Polarization and power density curves of HT-PEMFCs for three different anode fuels: 0.0% of CO, 1.5% of CO, and 3.0% of CO [21].

Other advantages of HT-PEMFCs are heat and water management. In LT-PEMFCs, energy is produced as a heat that must be immediately removed from the system; otherwise, overheating causes degradation of components and malfunction. Furthermore, conventional air-cooling systems are not sufficient for this purpose and sophisticated cooling systems required, which increases the weight and cost of an order. In HT-PEMFCs, thanks to the large temperature gradient between the environment and fuel cell, the heat transfer rate increases. This provides better and easier heat management. On the water management side, when operating at lower temperatures (below 80°C), a dual-phase water system is present. It might be kept in control due to the humidification requirements of the Nafion® membrane, which is very difficult. At higher temperatures, liquid water does not exist, so there is only single phase (water vapor) present. This means the transport of water is simple, and the design of flow field plates can be simplified. Furthermore, removing the liquid water in the system may prevent blocking active sites, which means more reaction takes place [22].

1.5. Importance of Polybenzimidazole (PBI)

Polybenzimidazole (PBI, short for poly[2,2'-(*m*-phenylene)-5,5'-bisbenzimidazole]) is a high performing amorphous polymer discovered by American polymer chemist Carl Shipp Marvel. With over 400°C of the glass transition temperature (T_g), it has superior durability, retention of stiffness, and toughness at elevated temperatures. Due to its high stability, PBI is an excellent candidate for high-temperature applications, including firefighter's gear, space suits, and high-temperature PEM fuel cell operations.

Table 2.2. *Electrical, physical, and mechanical properties of polybenzimidazole.*

Dielectric constant @1 MHz	3.2
Compressive modulus (GPa)	6.2
Compressive strength (MPa)	400
Tensile modulus (GPa)	5.9
Tensile strength (MPa)	160
Elongation at break (%)	3
Hardness (Rockwell)	K115
Poisson's ratio	0.34
Density ($g \cdot cm^{-3}$)	1.3
Coefficient of thermal expansion ($10^{-6}\ K^{-1}$)	23
Thermal conductivity @23C ($W \cdot m^{-1} \cdot K^{-1}$)	0.41
Upper working temperature (°C)	260-400

1.5.1. Fabrication of Polybenzimidazole

The synthesis of typical PBI is carried out by the step-growth polymerization (Figure 1.13). Technical production can be conducted in two steps. In the first step, aromatic tetra-amine is condensed with the diphenyl ester of an aromatic dicarboxylic acid at 220–260°C, yielding a poly (amino amide) through the elimination of phenol. In the second step, ring closure with the elimination of water is conducted at 400°C. The

amorphous nature of the polymer is suitable for further improvements, including improvement in conductivity and solubility [88].

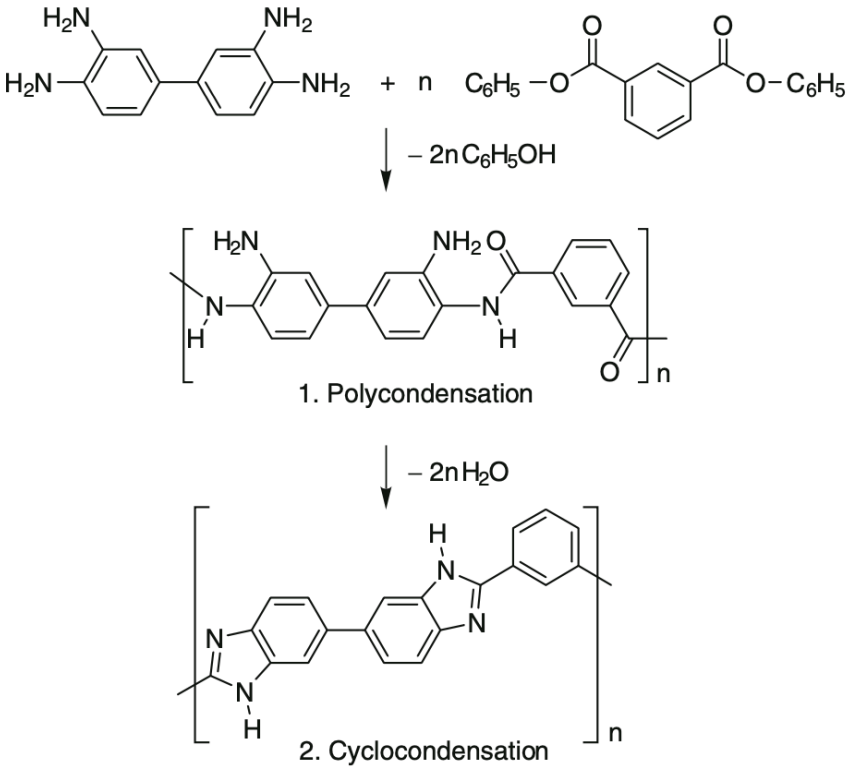

Figure 1.13. Fabrication of the polybenzimidazole (PBI) by the step-growth polymerization [88].

1.5.2. Improving the Polybenzimidazole

There are many ways to improve the properties of PBI further. For example, modification of the leading chains through the incorporation of "aryl sulfone" and "para-phenylene" linkages improve the acid-doping capability and somehow improve the mechanical properties [89]. Synthesis of cross-linked PBIs with poly(benzoxazine), preparation of other PBI co-polymers, and blends are other ways to improve the properties [90].

1.5.3. Polybenzimidazole Membranes for HT-PEMFCs

Considering the advantages of high-temperature proton exchange fuel cells (HT-PEMFC) over the low-temperature ones (detailed in section 1.4.7), "performance

rather than a cost" goal in early stages brings the development of PBI (polybenzimidazole) membranes in the late 1990s. Despite generation large amounts of water at the cathode, conductivities of perfluorinated membranes such as Nafion® are strongly dependent on the level of inside hydration. At the operating temperatures above 100°C under the atmospheric pressure, humidifying the membrane becomes more complicated. One of the effective ways is pressurizing reactants to over 2 Bar above ambient pressure, but this is also not practical because of the high parasitic power requirements for compressors. So, membranes that do not require water to sustain proton conductivity have been established with phosphoric acid doped polybenzimidazole (PBI) polymer. However, before that, PBI has already known as one of the best engineering polymers; it has a glass transition temperature (T_g) of over 400°C, spectacular mechanical properties, and excellent permeability. Having higher resistance to dehydration enables the operation at elevated temperatures. It has been reported that at the temperatures over 150°C, phosphoric acid doped PBI films can achieve a conductivity of 3.5 x 10^{-2} S·cm^{-1}, and also, they are entirely tolerant up to 2% CO in hydrogen, which is very important for the fueling issues of HT-PEMFCs [15].

1.5.4. Proton Conductivity of Polybenzimidazole Membranes

Unlike the Nafion® membranes, PBI membranes do not require humidified conditions to maintain proton conductivity. The proton conductivity mainly occurs through acid-doping (generally phosphoric acid), and strongly dependent on acid-doping level. Typical conductivity can be demonstrated by a modified Arrhenius equation (Eq. 1.7), where σ^0 and A are pre-exponential factors; R is the Boltzmann constant; T is membrane testing temperature, and E_a is the activation energy. Activation energy is correlated with the acid-doping level, and it decreases while increasing the acid-doping level. (e.g., 41 KJ·mol^{-1} for doping level of 3.00 PA/RU; 34 KJ·mol^{-1} for doping level of 4.20 PA/RU; 27.5 KJ·mol^{-1} for doping level of 6.0 PA/RU) [91].

$$\sigma = \sigma^0 \exp\left(\frac{-E_a}{RT}\right) = \frac{A}{T} \exp\left(\frac{-E_a}{RT}\right) \quad (1.7)$$

1.6. Aim of the Thesis

The main goal of this thesis is to develop a highly efficient, non-noble fuel cell electrocatalyst (Co-N/MWCNT) with knowledge of the recent advances in materials science and chemistry. Synthesis and characterization of such an electrocatalyst could be very challenging and require precise step-by-step verification. Due to the infancy of the subject, building robust literature is still very popular and essential. Ongoing researches about Me-N-C complexes are generally focused on the fundamentals of oxygen reduction mechanisms and low-temperature applications of proton exchange membrane (PEM) fuel cells. Moreover, considering the subject's individuality, there is still a lack of knowledge on the cobalt-based Me-N-C catalysts, especially for the HT-PEMFC operations. In this thesis, procedures about the synthesis of Co-N/MWCNT catalysts through the high-temperature pyrolysis treatment, characterization, and demonstration of its electrochemical performance will be demonstrated. Furthermore, the second course in the thesis is the development of polybenzimidazole (PBI) modified carbon-nanotubes as a support material for platinum-based electrocatalysts (Pt-PBI/MWCNT) to increase catalytic durability at elevated temperatures. To obtain more durable electrocatalyst, preparation of the polymer-wrapped support material (PBI/MWCNT) and microwave-assisted reduction of platinum nanoparticles will be examined.

CHAPTER 2

LITERATURE REVIEW

2.1. High-Performance, Non-Noble Me-N-C (Me = Co or Fe) Catalysts for Oxygen Reduction Reaction (ORR)

Because of the excellent electrochemical properties, platinum group metals are considered the best alternatives and leading materials for catalyzing both H_2 oxidation (HOR) and O_2 reduction (ORR). However, the increase in demand for noble metals hampers economic viability and sustainability. Even decreasing the amount of noble metals in the catalysts does not bring adequate economic efficiency for the commercialization [24]. Moreover, for the ORR, the superior performance of platinum-based catalysts is not so important because the current-limiting kinetics mainly occurred at the cathodic side. So, ongoing researches are generally focused on the decreasing unit cost of the electrocatalysts. This brings the idea of developing high-performance, cost-efficient electrocatalysts from non-noble metals, especially for the ORR. Recently, nitrogen-doped carbons and transition metals (Ni, Fe, Co) have been demonstrated to have great potential for such a mission [25,26,40,41,43,63-71]. The main motivation of such researches is creating a ternary complex over the carbon support material (amorphous carbon, graphene, nanotube) by specific heat treatment and understanding the kinetics of its electron transfer mechanisms. The literature indicates that the results of the electrochemical measurements are good enough for a typical ORR operation. Furthermore, catalysts may gain even some durability in the alkaline or acidic medium [27,28,41]. Among the various support materials, existing graphene-like materials have shown desirable results due to the two-dimensional layered structure of sp^2-hybridized atoms combined with the Me-N_x structures. But, the three-dimensional nano-architectures such as carbon nanotubes and nanofibers enhance the surface-gas phase interaction while providing better resistance to oxidation [29,46].

2.1.1. Catalytic Metal-N_x-C Sites

It is known that all of the pyridinic, pyrrolic and graphitic nitrogen sites are favored for ORR. Some researchers conclude that the N-doped-graphene (graphitic-N) has more pathways and could promote $4e^-$ on a single active site. However, the formation of Me-N_x clusters on graphene found to be energetically more favorable and responsible for catalytic activity [34]. Furthermore, according to DFT calculations, Me-N_x clusters may provide thermodynamic stability and chemisorption energy for ORR intermediates such as O_2, O, OH, OOH, HOOH, and H_2O. Formation energy (ΔE) of Me-N_4 cluster near graphitic pores can be represented as;

$$\Delta E = E_{Me\text{-}N4\text{-}pore} - (E_{graphene\text{-}pore} - 6\,\mu_C + 4\mu N + \mu_{Me}) \quad (2.1)$$

From this equation, DFT calculations suggest that the formation energies of Fe-N_4, Co-N_4, Ni-N_4 clusters are -3.75, -4.53, and -4.72 eV, respectively [34]. Negative formation energy means that the formation of these clusters near graphitic pores is favorable.

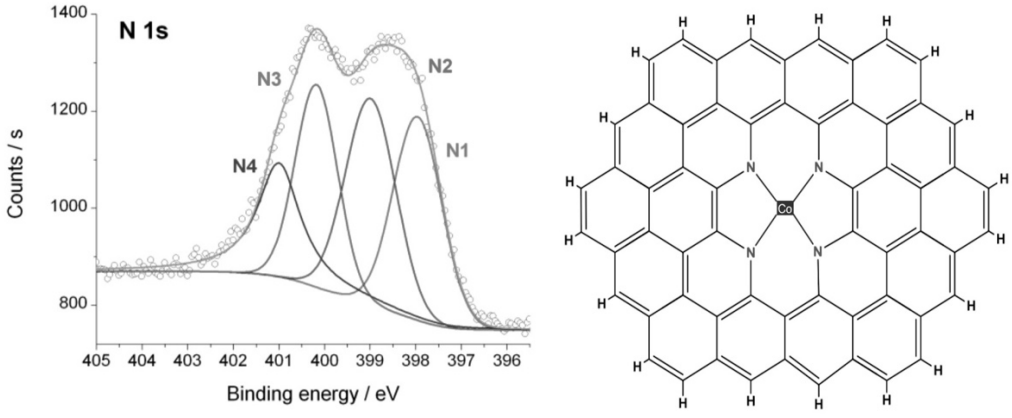

Figure 2.1. Deconvolution of XP spectra of N 1s [35] and most efficient structure of Co-N_4-C

Characterization of these structures near graphitic pores can be evaluated by deconvolution and quantification signals gathered from the XPS spectra. As seen in Figure 2.1, deconvolution separates the intensity curves of graphitic, pyridinic, and

pyrrolic structures of nitrogen atoms. Around 398 eV, pyridinic-N described as N1, around 400 eV pyrrolic-N as N3 and around 401 eV graphitic-N as N4.

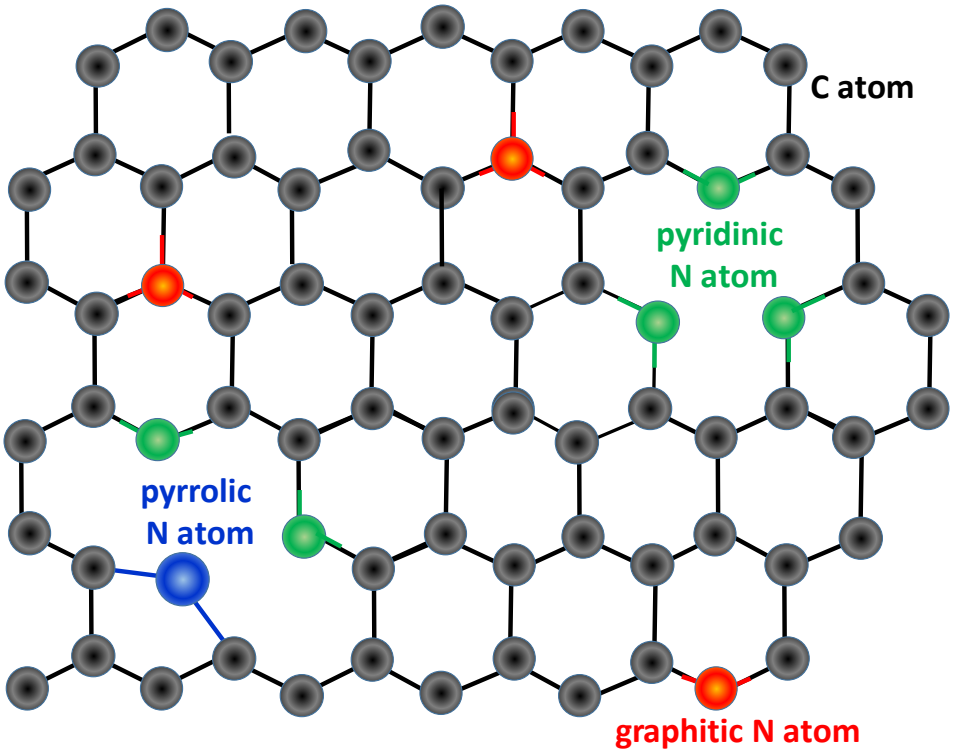

Figure 2.2. Schematic demonstration of graphitic-N, pyridinic-N, and pyrrolic N.

For the further characterization of the Me-N_x sites, other useful tools such as XAS (X-ray absorption spectroscopy), XANES (X-ray absorption near-edge structure), and EXAFS (Extended X-ray absorption fine structure) with DFT calculation methods must be used. The majority of pyrrolic-N and pyridinic-N structures show a peak in radial distribution from EXAFS at 1.6 – 1.8 Å. Additional Me-C peaks can be observed at 2.0 – 2.4 Å. Recent advances in electron microscopy, such as aberration-corrected scanning TEM, could also enable us to see single atomic Me sites on CNTs and have a vital complementary role in such a characterization [36,44].

2.1.2. Oxygen Reduction Reaction (ORR) on Metal-N_x-C Sites

A remarkable amount of studies demonstrated that the significant enhancement in ORR activity over Me-N_x sites. Distribution of pyridinic-N and pyrrolic-N may contribute further activity on the open edges or defects of nitrogen-doped CNTs. Comparing Me-N_{2+2} with Me-N_4, DFT calculations indicated that the formation of the pyridinic-N structure of Me-N_4 is the more active and preferred site for the ORR [30,31,33,63-71]. Another study showed that the formation energy of the Fe-N_4-C is -5.04 eV, which means the catalytic site is energetically stable. Moreover, the calculated O – N bond length is 3.11 Å, and the O – Fe bond length is 1.71 Å; this means there is no activation energy barrier for ORR. After the ORR, charge transfers indicate that the Fe becomes more positive. Moreover, effective charges of four N atoms remain nearly the same. This means charge transfer occurs mostly in the ferrous state rather than the ferric state [32]. Bader charge analysis on Fe-N_4/C shows that the charge transfer of four N and Fe atoms are $Fe^{+1.22}$, $N^{-2.57}$, $N^{-2.58}$, $N^{-2.56}$, respectively. On the surrounding carbon side, charge transfer of eight C atoms are, $C^{+1.06}$, $C^{+1.07}$, $C^{+1.08}$, $C^{+1.07}$, $C^{+1.013}$, $C^{+1.09}$, $C^{+1.03}$, and $C^{+1.18}$ respectively [32]. A large amount of charge transfer between N – C and N – Fe means that nitrogen atoms play a critical role in stabilizing the defect site. Looking into the adsorption of O_2 over the central metal atom, there are two possibilities of the placement. That can be either a side-on or end-on configuration. In the side-on configuration, the O_2 molecule lies along the parallel to the central plane, and two oxygen atoms have the same distance to the central metal atom. In the end-on configuration, one oxygen atom is closer to the central atom. DFT calculations suggest that the minimal binding energies observed for O_2 over the Ni-N_4 (-0.05 eV for side-on and -0.02 eV for end-on). Such a weak interaction of the Ni-N_4 cluster with O_2 concludes that the Ni is the inefficient choice for the ORR. On the other hand, the binding energies of both Fe-N_4 and Co-N_4 are sufficient enough to capture O_2 molecules to initiate ORR (Table 2.1).

Table 2.1. *DFT calculation results of the binding energy for various ORR intermediates over Fe-N_4 and Co-N_4 clusters* [34].

	Fe-N_4 clusters			Co-N_4 clusters		
Adsorbates	BE	d_{Fe-O}	d_{O-O}	BE	d_{Co-O}	d_{O-O}
O_2 (end on)	-1.45	1.69	1.29	-0.63	1.85	1.28
O_2 (side on)	-1.61	1.83, 1.90	1.37	-0.82	1.87, 1.94	1.34
OOH	-1.88	1.84	1.46	-1.18	1.86	1.45
HOOH	-2.65	1.88	2.51	-1.90	1.90	2.58
H_2O	-0.40	2.22	-	-0.25	2.25	-
O	-4.94	1.61	-	-3.57	1.69	-
OH	-3.14	1.83	-	-2.48	1.83	-

Due to the high operating temperatures of PEMFCs, stability is a significant problem considering the catalytic activity, corrosion, and degradation of active sites. However, recent studies showed that the increase in temperature might also produce a positive effect on the stability of Me-N-C sites and their dioxygen hydroxyl complexes.

K_C (Thermodynamic stability) values are found as 2.5 x 10^{-8} (Fe-N_4-C_{12}($O_{2,\,ads}$)) to 8.8 x 10^{-8} (Fe-N_{2+2}-C_{12}($OH_{,\,ads}$)) for $\Delta_r H°_{298}$. Around the 80°C, the typical operating temperature of LT-PEMFCs, K_C values are 1.0 x 10^{-7} (Fe-N_4-C_{12}($O_{2,\,ads}$)) to 9.1 x 10^{-9} (Fe-N_{2+2}-C_{12}($OH_{,\,ads}$)) for $\Delta_r H°_{353}$. The slightly endothermic reaction for H^+ and decreasing number of electrons in the antibonding orbitals may be responsible for the thermodynamic stability at elevated temperatures [37]. However, there is still some confusion about the thermodynamic stability at even higher operating temperatures, such as 140 °C or more, which are the operating temperatures of HT-PEMFCs. Researches about this field are very limited in number, and there are only a few studies related to the usage of Me-N-C catalysts for ORR in High-Temperature PEMFC applications [43].

2.1.3. Evaluating ORR Performance by Rotating Disc Electrode (RDE) Method

Rotating disc electrode (RDE) method is widely used for evaluating the electron-transfer kinetics of materials, particularly for the oxygen reduction reaction (ORR). In conventional methods, neglecting the ionic migration, there are only two significant variables left for the transport; diffusion and convection. For the conventional method, solution convection is negligible, so the thickness of the diffusion layer may become thicker and thicker during the reaction process. RDE provides vigorous solution convection via electrode rotation, which results in a fixed diffusion layer and steady-state current density (k). To summarize current-potential relation on RDE, Fick's second law has to be used for expressing limiting current density as a function of rotating rate and concentration. In this manner, three directions (r, x, and ϕ) change with time through the diffusion (Eq. 2.2) and convection (Eq. 2.3), where C_o is the saturated concentration of oxygen and D_o is the diffusion coefficient of oxygen [80,81].

$$\left(\frac{\partial C_o}{\partial t}\right)_{diffusion} = D_o \left[\frac{\partial^2 C_o}{\partial x^2} + \frac{\partial^2 C_o}{\partial r^2} + \frac{1}{r}\left(\frac{\partial C_o}{\partial r}\right) + \frac{1}{r^2}\left(\frac{\partial^2 C_o}{\partial \emptyset^2}\right)\right] \quad (2.2)$$

$$\left(\frac{\partial C_o}{\partial t}\right)_{convection} = -\left[v_r \left(\frac{\partial C_o}{\partial r}\right) + \frac{v_\emptyset}{r}\left(\frac{\partial C_o}{\partial \emptyset}\right) + u_x \left(\frac{\partial C_o}{\partial x}\right)\right] \quad (2.3)$$

At steady state, the concentration gradient (vs. time) must be the same for both convection and diffusion. Moreover, due to geometrical-symmetry related to the disk center, oxidant concentration is not a function of ϕ.

$$D_0 \frac{\partial^2 C_o}{\partial x^2} = u_x \left(\frac{\partial C_o}{\partial x}\right) \quad (2.4)$$

$$u_x = -0.51\omega^{3/2} v^{-1/2} x^2 \quad (2.5)$$

Combining equation 2.4 and 2.5 and resolving it for the limiting oxidant supply, (C_O = 0 at x=0) limiting current density can be expressed by Eq. 2.6;

$$I_{DC,O} = nFD_o \left(\frac{\partial C_o}{\partial x}\right)_{x=0} = 0.62nFD_0^{2/3} v^{-1/6} \omega^{1/2} C_o^0 \quad (2.6)$$

Evaluation of the number of transferred-electrons (n) can be estimated by the Koutecky-Levich plot of $I_{D,\ C}$ vs. $\omega^{1/2}$, where the slope of straight-line equals to $0.62nFD^{2/3}\nu^{-1/6}C$. However, if the reduction kinetics of oxidant is much slower than that of diffusion convection, surface concentration cannot be zero. In this case, Levich plot will not be straight anymore with an increasing $\omega^{1/.2}$ To surplus slow electron kinetics; the modified equation will be used, which is Eq. 2.7;

$$\frac{1}{j} = \frac{1}{j_k} + \frac{1}{j_d} = \frac{1}{j_k} + \frac{1}{0.62nFC_{O_2} D_{O_2}^{2/3} v^{-1/6} \omega^{1/2}} \quad (2.7)$$

Where j is the overall current density, j_k is the kinetic current density, j_d is the diffusion current density, n is the number of transferred electrons in the ORR, F is the Faraday constant, C_{O_2} is the saturated concentration of oxygen, D_{O_2} is the diffusion coefficient of oxygen, ν is the kinematic viscosity of the solution, and ω is the rotation rate of the electrode [80,81]. Oxygen is the most common oxidant for most fuel cell cathodes simply due to the availability of the oxygen in the atmosphere and the large thermodynamic driving force of the ORR. There are two possible ways of reductions that can take place. Oxygen can reduce to water by direct 4-electron pathway (or to peroxide by 2-electron pathway. The most efficient one is the direct reduction of oxygen through the 4-electron pathway.

2.1.4. Water Formation Reaction (WFR) on Metal-N_x-C Sites

Studies about the WFR process show the relative potential energy of H_2O formation forces H atoms to move closer to oxygen simultaneously, which results in the formation of H_2O. There is no activation energy barrier for this reaction. However, when we look into the distance of Fe – O atoms which is 2.12 Å, there might be a chance that the H_2O is slightly trapped. To desorb/move away trapped molecule, bonds between Fe – O need to be broken. After desorption, the distance between Fe – O becomes 4.0 Å, and the relative potential energy of formed H_2O is lower than that

of the initial state by 6.81 eV. After the desorption, driving force through desorption of H_2O will make a catalytic site reach its equilibrium state, then the system goes back to its original structure to catalyze the next cycle.

2.1.5. Heat Treatment

Although the exact mechanisms have not fully understood yet, there is strong evidence that positive effects of heat treatment on activity and stability. Moreover, the structure of the catalytic site is strongly dependent on the heat-treatment variables. Around the 700°C, pyrolysis may produce the more metallic-N_x sites, and above the 700°C towards 1000°C, N-molecules are removed slowly. So, the system will contain only inorganic metal fragments over the carbon support. Many studies conclude that the most effective pyrolysis temperature to create Me-N_x sites is around 700-800°C in which the ratio of pyridinic-N/pyrrolic-N fragments is higher [38,39]. Vecchio and Aricò have demonstrated (Table 2.2) that the composition of pyridinic-N has decreased. In contrast, the pyrrolic-N and graphitic-N have increased while shifting the pyrolysis temperature from 800°C to 1000°C.

Table 2.2. *Nitrogen concentration and structure distribution from XPS spectra [38].*

Composition of Nitrogen (relative %)						
Catalysts	N (at. %)	Pyridinic	N-M (M = Co, Fe)	Pyrrolic	Graphitic	N – O
Co-N-C 800	1.7	34.21	10.44	39.74	13.10	2.51
Co-N-C 1000	0.7	24.59	11.08	43.86	17.97	2.50
Fe-N-C 800	1.3	27.74	36.42	21.04	13.78	1.02
Fe-N-C 1000	0.7	14.37	26.54	36.35	16.80	5.94

Raman spectroscopy is generally used to measure the quality of carbon-based catalyst; the ratio of D/G band is useful for determining the crystallization degree of the structure. Upon increasing the pyrolysis temperature, I_D/I_G slightly decreases, which means the increase in crystallinity (can be verified by XRD), decrease in the BET surface [42,45].

2.1.6. Electrochemical Performance

The electrochemical properties of such catalysts are mainly dependent on the synthesis methods and support materials. However, most of the researchers conclude that the uniformly distributed fine nanoparticles are essential for an excellent performance. In the literature, it was demonstrated that at the 0.6 V, unprecedented power density may vary between ~0.2 W cm^{-2} to ~0.8 W cm^{-2} for a typical LT-PEM Fuel Cell. Moreover, M-N-C catalysts may exhibit superior durability under alkaline or even in an acidic environment. After the 5000 or 10000 cycle, catalytic stability of M-N-C for ORR is much better than that of the commercial-grade Pt/C catalyst [38,47,48].

2.2. Polybenzimidazole (PBI) Modified Carbon Nanotubes as a Support Material for Platinum-Based Electrocatalysts (Pt-PBI/MWCNT)

High-temperature PEM fuel cells bring so many advantages to the fuel cell industry, such as tolerance of CO impurities in hydrogen fuel up to 2% or more, improved reaction kinetics, improved efficiency, and more natural heat and water management. Acid doped PBI (Polybenzimidazole) is the critical polymer for HT-PEMFCs because of the excellent thermal and chemical stability over 150°C. However, usage of phosphoric acid-doped PBI membranes may have some side effects, such as poisoning the active sites of platinum catalysts through the acid, resulting in a reduction in mechanical stability. Combining with the higher operation temperatures, this degradation may even accelerate the corrosion of carbon, which also results in a significant decrease in durability [49,50]. Being the critical material in nanoscience and chemistry, carbon-nanotubes are also very important for fuel cell electrocatalysts as a support material. They have extraordinary electrochemical properties and very high surface areas to improve fuel cell efficiency while providing the reduction of precious metal loadings on the electrodes. However, degradation in elevated temperatures and insolubility of CNTs hinder further improvement to achieve more stable support material, especially for the HT-PEMFC applications. Recently, there has been significant progress over increasing the durability of platinum-based catalysts in an acidic medium by preparing a PBI wrapped CNTs as a support material [51]. Moreover,

there is strong evidence that the polymer film might generate more binding sites on where platinum nanoparticles are attached. Kaewsai and Lin have also demonstrated that the polymer film may improve efficiency by decreasing the amount of platinum waste in the catalyst [51].

2.2.1. PBI Coating Over CNTs

Recent studies demonstrated that the PBI acts as an excellent solubilizer for CNTs. Dispersing in DMAc and ultrasonication for a sufficient time may provide enough driving force to coat CNTs with a polymer film. To characterize PBI/MWCNT, two-step weight reduction from the thermogravimetric analysis (TGA) could be used (Figure 2.3). The first step represents the thermal degradation of PBI and starts around ~500°C, and the second one is related to the MWCNT, around 700-800°C.

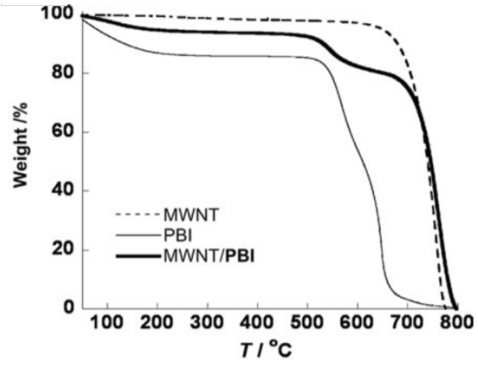

Figure 2.3. TGA of a PBI/MWCNT [53]

The morphology of the structure can be observed within the TEM analysis. Assuming that the PBI uniformly wraps the cylindrical MWCNT, the theoretical thickness of the wrapping layer (r_{PBI}) can be calculated from the Eq. 2.8 and somehow can be verified by the TEM images (Figure 2.4);

$$r_{PBI} = \left(\sqrt{1 + \frac{V_{PBI}}{V_{MWCNT}}} - 1\right) r_{MWCNT} \tag{2.8}$$

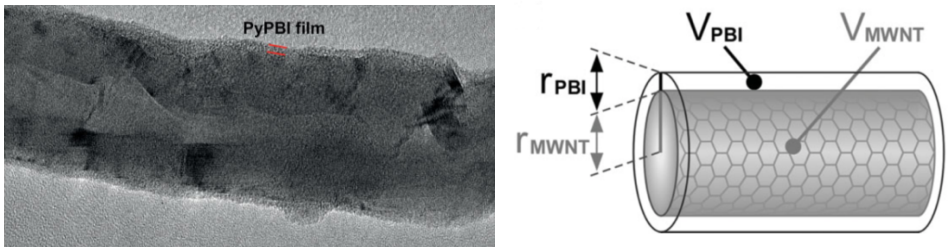

Figure 2.4. (a) TEM image of PBI/MWCNT (b) Illustration of PBI/MWCNT [52]

Considering the small radius of MWCNTs, the thickness of the PBI film should even be smaller. Such a thin structure is suitable for the preparation of an efficient electrocatalyst [52,72-75].

2.2.2. Pt Loading on PBI/MWCNT

The reduction of Pt precursor and the deposition of Pt nanoparticles over PBT/MWCNT generally carried out by the alcohol reduction method. Heating the precursor in ethylene glycol (EG) is the most suitable and practical way of reduction. Nowadays, in some cases, microwave-assisted irradiation may also be the cost and time-efficient method considering the synthesis of novel catalysts. Moreover, when compared with the polyol synthesis, microwave-assisted irradiation may promote more efficient and uniform loadings of nanoparticles. [57-62,72-75]. The reduction of Pt nanoparticles can be verified by XPS signals coming from the Pt (0) $(4f)_{7/2}$ and $(4f)_{5/2}$. Having large double peaks around the 70 – 75 eV is directly related to the spin-orbital splitting of platinum, and further deconvolution may also provide additional information about Pt (II) and Pt (IV) [51].

2.2.3. Electrochemical Performance

Cyclic Voltammetry (CV) is the most practical electrochemical characterization method for the H_2 adsorption performance of an electrocatalyst. ECSA (Electrochemically Active Surface Area) of the electrocatalyst is calculated with the Eq. 2.9 from the charges (Q_H) in the specific H_2 adsorption/desorption regions (-0.2V to 0.1V) assuming a value of 210 $\mu C \cdot cm^{-2}$ for the adsorption of hydrogen monolayer.

$$ECSA\ (m^2 g^{-1}) = \frac{Q_H(\mu C\ cm^{-2})}{210\ (\mu C\ cm^{-2})\ x\ Pt\ loading\ (g\ m^{-2})} \quad (2.9)$$

From the recent studies, ECSA values of Pt-PBI/CNT catalysts vary between 33 to 50 $m^2 \cdot g^{-1}$ depends on the metal loadings, support materials, and synthesis methods. Such high ECSA values are sufficient for the effective oxidation of hydrogen in a typical HT-PEMFC operation. Further studies show that the peak power densities are as high as ~600-700 $mW \cdot cm^{-2}$, which are significantly higher than those of traditional electrocatalysts [53-56]. In addition to that, an increase in durability is the primary key parameter for this type of composite electrocatalysts.

CHAPTER 3

EXPERIMENTAL PROCEDURE

3.1. Synthesis and Characterization of Co-N/MWCNT Catalysts for Oxygen Reduction Reaction (ORR) and Evaluation of Its Performance in HT-PEMFC

3.1.1. Materials

Cobalt (II) nitrate hexahydrate ($Co(NO_3)_2 \cdot 6H_2O$, >98%) (Sigma-Aldrich), 1H-1,2,3-Triazolo[4,5]pyridine (TAPy >98%) (Sigma-Aldrich), Multi-walled carbon nanotubes (MWCNTs >98% , D = 6-13 nm, L = 2,5-20 μm) (Sigma-Aldrich), Ethanol (Sigma-Aldrich), Nafion® 117 solution (15 wt. %) (Sigma-Aldrich), DI water (Sigma-Aldrich), 1-Propanol (Sigma-Aldrich), Teflon (60 wt. %) (ElectroChem), GDL (Sigracet 34 BC), Commercial PBI membrane (40μm) (Dapozol M40), Commercial Pt/C (60 wt. % and 40 wt. %) (HISPEC, Tanaka), 0.5 M H_2SO_4 as prepared aqueous solution. All chemicals were used as received, without further purification. All gases were ultra-pure, >99.9% purity.

3.1.2. Synthesis of Co-N/MWCNT

To obtain 12 wt. % of metallic Co, 443 mg of metal precursor cobalt (II) nitrate hexahydrate, 500 mg TAPy, and 250 mg of MWCNT are required. Initially, $Co(NO_3)_2 \cdot 6H_2O$ and TAPy mixed in a 35 mL ethanol and the as-prepared solution was stirred about 2 hours at 60°C. Simultaneously, another solution was prepared to disperse 250 mg CNTs into 120 mL ethanol and ultrasonicated for about 30 minutes. The latter mixture was added into the previous solution and heated under reflux at 60°C and held there for about 5 hours. To remove excessive ethanol, the solution was filtrated and kept in a furnace for overnight at 80°C. As-obtained Co-N/MWCNT

powder was placed in a tube furnace for the further heat-treatment process. High-temperature pyrolysis of dry powder was achieved under the argon atmosphere. After the removal of residual air, the furnace was heated at 5°C·min^{-1} until 700°C and held there for about an hour, then cooled to room temperature at 10°C·min^{-1}. Detailed characterization of the synthesized Co-N/MWCNT catalyst and its electrochemical performance will be demonstrated in the following sections.

3.1.3. Physico-Chemical Characterizations

X-ray photoelectron spectroscopy (XPS) was performed using PHI 5000 VersaProbe Al Kα instrument under vacuum with an energy range of 0 to 900 eV, step size of 1.0 eV and X-ray spot size of 100 μm. The catalyst sample was characterized by using an ION-ToF (Gmbh) ToF-SIMS V equipment with a Bi^+ ion source. A 25 kV Bi^+ beam was pulsed at 10 kHz with a bunched pulse width of < 1 ns. The crystallinity of the Co-N/MWCNT catalyst was determined by X-ray diffraction (XRD) using Rigaku Ultima-IV (Cu Kα radiation, 1.54056 Å). Raman spectroscopy was obtained using a Renishaw inVia confocal Raman microscope with an excitation wavelength of 532 nm Nd-YAG laser. JEOL JEM 2100F with an accelerated voltage of 200 kV was used as a high-resolution transmission electron microscope.

3.1.4. Electrochemical Characterization

Oxygen reduction (ORR) performance of a Co-N/MWCNT catalyst was examined through the rotating disc electrode (RDE) analysis. Electrochemical workstations, Wonatech Zive SP-2 and BASI RDE-2 with the three-electrode system were prepared to contain a glassy carbon (GC) working electrode (0.0707 cm^2), Ag/AgCl (incl. KCl) reference electrode and Pt wire auxiliary electrode. The catalyst solution was prepared by ultrasonically mixing of 6.4 mg Co-N/MWCNT powder, 22 μl Nafion® solution (15% wt.), 120 μl DI water, and 300 μl ethanol. 2 μl of as-prepared solution was dropped onto the surface of the GC electrode (polished with an alumina suspension) to obtain 400 μg·cm^{-2} of final catalyst loading, and dried overnight at 25°C. 0.5M H_2SO_4 was used as an electrolyte solution. To provide saturation, O_2 gas was purged

before the experiment. Linear sweep voltammetry (LSV) curves were collected at room temperature with a scan rate of 5 $mV \cdot s^{-1}$, and the rotation rates (ω) of 400, 800, 1200, 1600, and 2000 rpm.

3.1.5. Preparation of Membrane Electrode Assemblies

Cathode catalyst ink was prepared through the ultrasonically mixing of Teflon binder (4.0 mg), DI water (0.5 ml), propanol (3.0 ml), and the necessary amount of Co-N/MWCNT powder (15.0 mg). Due to the lower solubility and slow oxygen diffusion in phosphoric acid, final catalyst loading in HT-PEMFC applications must be relatively higher than in the LT-PEMFC applications. So, the final cathode loading was selected as 3.0 $mg \cdot cm^{-2}$ for the Co-N/MWCNT. On the anode side, to get final catalyst loading as 0.6 $mg_{Pt} \cdot cm^{-2}$, required amount of Pt/C powder was ultrasonically dispersed in the Teflon binder, propanol, and DI Water solution. As-prepared catalyst inks were applied on a 5 cm^2 carbon paper GDL through the Sonotek (USA) ultrasonic coating machine. After the removal of residual solvent, GDEs were ready to assembly with the membrane. The 40 μm commercial polybenzimidazole (PBI) membranes were immersed in H_3PO_4 (85 wt.% aqueous solution) at room temperature for about seven days to maintain proton conductivity. The acid doping level (mole number of H_3PO_4 per repeat unit of PBI) of the membranes was calculated as approximately 11. Finally, prepared GDEs were attached and sandwiched to the membrane by hot-pressing method at 150°C under a pressure of 172 $N \cdot cm^{-2}$ for 5 min. For the reference, a membrane-electrode-assembly (MEA) consisting of commercial Pt/C catalyst (0.6 $mg_{Pt} \cdot cm^{-2}$ for both the anode and the cathode) was prepared using the aforementioned methods.

3.2. Synthesis and Characterization of Pt-PBI/MWCNT Composite Catalyst and Evaluation of Its Performance in HT-PEMFC

Synthesis of a Pt-PBI/MWCNT electrocatalyst should be conducted in two different sections, which are preparation of a highly dispersed PBI/MWCNT support material, and microwave-assisted reduction of Pt nanoparticles (Figure 3.1). Just as the previous

catalyst, synthesis and characterization of such an electrocatalyst are challenging and require a comprehensive work.

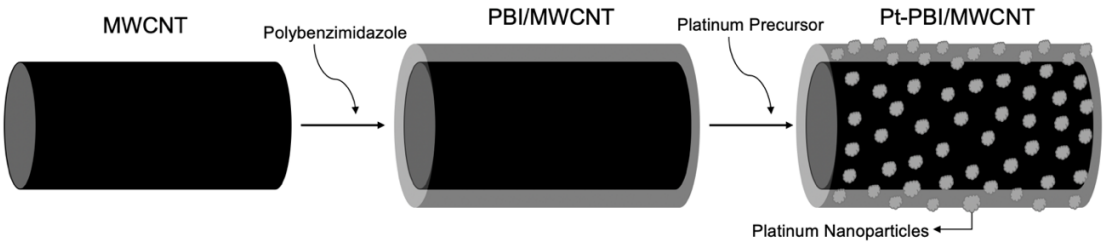

Figure 3.1. Sequence showing preparation of a Pt-PBI/MWCNT composite electrocatalyst.

3.2.1. Materials

Chloroplatinic acid hexahydrate ($H_2PtCl_6 \cdot 6H_2O$) (Sigma-Aldrich), Poly2,2'-(m-phenylene)-5,5'-bibenzimidazole powder (PBI Avg. Mw = 18,000) (Celazole), (-COOH) Functionalized multi-walled carbon nanotubes (MWCNTs >96%, D = 48-78 nm, L = 10-25 μm) (Nanografi), N,N-Dimethylacetamide (DMAc, >99%) (Sigma-Aldrich), Ethylene glycol (EG, >99%) (Sigma-Aldrich), Isopropyl alcohol (IPA, >99%) (Sigma-Aldrich), Nafion® 117 solution (15 wt. %) (Sigma-Aldrich), DI water (Sigma-Aldrich), 1-Propanol (Sigma-Aldrich), Teflon (60 wt. %) (ElectroChem), GDL (Sigracet 34 BC), Commercial PBI membrane (40μm) (Dapozol M40), Commercial Pt/C (60 wt. % and 40 wt. %) (HISPEC, Tanaka), 1 M NaOH in EG, 0.2 M HNO_3 and 0.1M $HClO_4$ aqueous solution. All chemicals were used as received, without further purification. All gases were ultra-pure, >99.9% purity.

3.2.2. Preparation of PBI/MWCNT

30 mg of PBI powder was dissolved in 75 mL DMAc under a magnetic stirrer. 75 mg of MWCNT was added into the PBI solution and mixed for about 10 minutes. In order to provide uniform dispersion, the as-prepared solution was ultrasonicated for about an hour. Having a good attraction between PBI and MWCNT, the dissolved polymer can easily wrap the carbon-nanotubes. Due to the functional sites (-COOH) of carbon-nanotubes, this process now becomes even more effectively. Finally, the solution with

MWCNTs was filtered and centrifugated for about an hour to remove excessive DMAc. The PBI coated MWCNT powder was dried overnight at 120°C.

3.2.3. Deposition of Platinum on PBI/MWCNT

A previously published method was modified as a microwave-assisted platinum deposition technique [78]. 100 mg of as-prepared PBI/MWCNT powder was added into a mixture of ethylene glycol (EG) and isopropyl alcohol (IPA) with a volume of 48 mL and 12 mL, respectively. After 1 hour of ultrasonication, 179 mg of Pt-precursor (chloroplatinic acid hexahydrate ($H_2PtCl_6 \cdot 6H_2O$)) was added to the previous solution to obtain 40 wt. % Pt in the final powder. The pH value of the as-prepared solution was fixed to the strong alkaline state by adding a sufficient amount of 1 M NaOH in EG because it is noted that higher pH values have a positive effect on the formation of fine nanoparticles. The suspension containing PBI/MWCNT powder and Pt-precursor was remixed for about 30 minutes under N_2 atmosphere. The solution was placed in a household microwave and irradiated for about 60 seconds at 600 W. After that, the pH of the mixture was normalized to the previous state by adding a sufficient amount of 0.2 M HNO_3, then magnetically mixed for about 30 minutes. Finally, the mixture was centrifugated and washed with acetone three times. As-collected catalyst powder was placed in a furnace and dried overnight at 100°C.

3.2.4. Physico-Chemical Characterizations

X-ray photoelectron spectroscopy (XPS) was performed using PHI 5000 VersaProbe Al Kα instrument under vacuum with an energy range of 0 to 900 eV, step size of 1.0 eV and X-ray spot size of 100 μm. The crystallinity of the Pt-PBI/MWCNT catalyst was determined by X-ray diffraction (XRD) using Rigaku Ultima-IV (Cu Kα radiation, 1.54056 Å). Thermal gravimetric analysis (TGA) was conducted using Perkin Elmer Pyris 1 under air at a heating rate of 5 °C min^{-1}. FEI Tecnai G^2 with an accelerated voltage of 120 kV was used as a transmission electron microscope (TEM).

3.2.5. Electrochemical Characterization

The electrochemical performance of the prepared Pt-PBI/MWCNT catalyst was examined through the cyclic voltammetry analysis. An electrochemical workstation,

Wonatech Zive SP2 with the three-electrode system, was prepared to contain a glassy carbon (GC) working electrode (0.0707 cm^2), Ag/AgCl (incl. KCl) reference electrode and Pt wire auxiliary electrode. The catalyst solution was prepared by ultrasonically mixing of 2.75 mg Pt-PBI/MWCNT powder, 17 mg Nafion® Solution, 180 µl DI water, and 1230 µl Isopropyl Alcohol (IPA). 2 µl of as-prepared solution was dropped onto the surface of GC electrode (polished with an alumina suspension) in order to obtain 0.02 $mg \cdot cm^{-2}$ of final Pt loading, and dried overnight at 25°C. 0.1M $HClO_4$ was used as an electrolyte solution, and before the experiment, excessive O_2 was removed from the solution by purging N_2 gas for about 30 minutes. The experiment was performed at 25°C with a 50 $mV \cdot s^{-1}$ scan rate between -0.25V and 1.2V. For the reference, a commercial Pt/C and Pt/MWCNT electrocatalysts were also prepared and tested using the aforementioned methods.

3.2.6. Preparation of Membrane Electrode Assemblies

The catalyst ink was prepared through the ultrasonically mixing of Teflon binder (5.0 mg), DI water (0.5 ml), propanol (3.4 ml), and the necessary amount of Pt-PBI/MWCNT powder (16.5 mg). Due to the lower solubility and slow oxygen diffusion in phosphoric acid, the final catalyst loading in the HT-PEMFC applications must be relatively higher than that in the LT-PEMFC applications. So, the final catalyst loadings were selected as 0.6 $mg_{Pt} \cdot cm^{-2}$ for both the anode and the cathode. The as-prepared catalyst ink was applied on a 5 cm^2 carbon paper gas diffusion layer (GDL) using a Sonotek (USA) ultrasonic spraying machine. After the removal of residual solvent, gas diffusion electrodes (GDEs) were ready to assembly with the membrane. The 40 µm commercial polybenzimidazole (PBI) membranes were immersed in H_3PO_4 (85 wt.% aqueous solution) at room temperature for about seven days to maintain proton conductivity. The acid doping level (mole number of H_3PO_4 per repeat unit of PBI) of the membranes was calculated as approximately 11. Finally, prepared GDEs were attached and sandwiched to the H_3PO_4 doped membrane by hot-pressing method at 150°C under a pressure of 172 $N \cdot cm^{-2}$ for 5 min. For the reference, a membrane-electrode-assembly (MEA) consisting of commercial Pt/C catalyst (0.6

$mg_{Pt} \cdot cm^{-2}$ for both the anode and the cathode) was prepared using the aforementioned methods.

3.3. High-Temperature PEM Fuel Cell Tests

Single-cell performances of MEAs were evaluated through the single-cell PEMFC test station (TEKSIS Co., Turkey) at the operating temperatures of 150°C, 160°C, 170°C, and 180°C under the atmospheric pressure (~101 kPa) and non-humidified conditions. Sealing of the MEAs, with graphite bipolar plates, gaskets, and current collectors, was carefully conducted to avoid stray current and gas leakage. Before the single-cell test, the leak test was conducted with the assistance of USFCC leak check procedure. During the experiments, pure H_2 (0.05 slpm ($l \cdot min^{-1}$)) and dry air (0.15 slpm) were fed to the anode/cathode as fuel and oxidant, respectively. The temperature of the single-cell was controlled by calibrated tandem thermocouples placed in anodic and cathodic bipolar plates. The relative humidity and pressure were controlled by the integrated hygrometer and barometer sensors. Before the V-i curves were collected, the load was adjusted to 0.6V and held there for about an hour to gather steady information. After the measurement of the open-circuit voltage (OCV), the current values were recorded through the step-wise switching of load from 0.9V to 0.4V with an interval of 0.05V. The schematic demonstration of the test station is detailed in the flowsheet below (Figure 3.2).

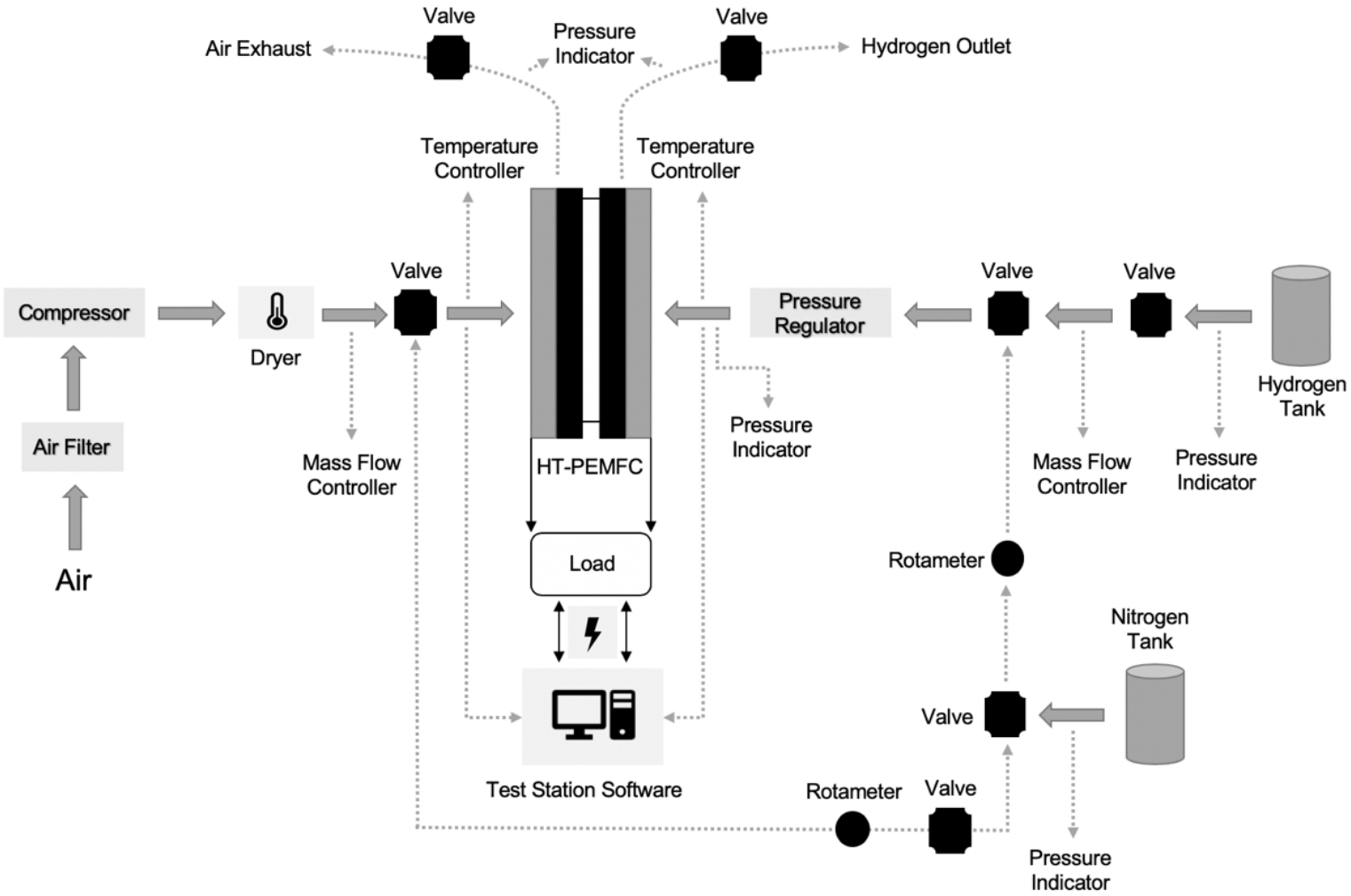

Figure 3.2. Schematic demonstration of the HT-PEMC test station.

CHAPTER 4

RESULTS & DISCUSSIONS FOR Co-N/MWCNT

SYNTHESIS AND CHARACTERIZATION OF Co-N/MWCNT CATALYST FOR OXYGEN REDUCTION REACTION (ORR) AND EVALUATION OF ITS PERFORMANCE IN HT-PEM FUEL CELL

4.1. Physico-Chemical Characterization

4.1.1. X-Ray Photoelectron Spectroscopy (XPS)

X-ray photoelectron spectroscopy is one of the most efficient ways to estimate elemental composition and the chemical state of the catalyst by giving enhanced information about structures of the complexes. Spectrum concluded that the presence of carbon, oxygen, nitrogen, and cobalt in the catalyst. Content of Co (5% wt.) and N (1% wt.) in the doped catalyst are much less than the C (90% wt.). To obtain further information, the core level of N 1s and Co 2p peaks must be deconvoluted. In the N 1s (Figure 4.1), two of the deconvoluted peaks, around 399.8 eV and 401.2 eV, belong to the pyrrolic-N and graphitic-N, respectively. The third peak, around 398.8 eV, belongs to both pyridinic-N and fragments of nitrogen complex with cobalt, Co-N_x. These moieties in the complex are very important for oxygen reduction reaction and directly related to the electrochemical performance. It is believed that the pyridinic-N sites generally obtained from the ring-opening of TAPy during pyrolysis at 700°C. In the Co 2p range (Figure 4.2), also three characteristics peaks were observed. Metallic Co, ternary complex (CoC_xN_y) / cobalt oxides (Co_xO_y) and cobalt nitrogen complex (Co-N_x) were obtained at 778.5 eV, 780.0 eV, and 781.4 eV, respectively. The cobalt nitrogen complex around 781.4 eV is consistent with the corresponding peak that detected at 398.8 eV in the N 1s spectrum.

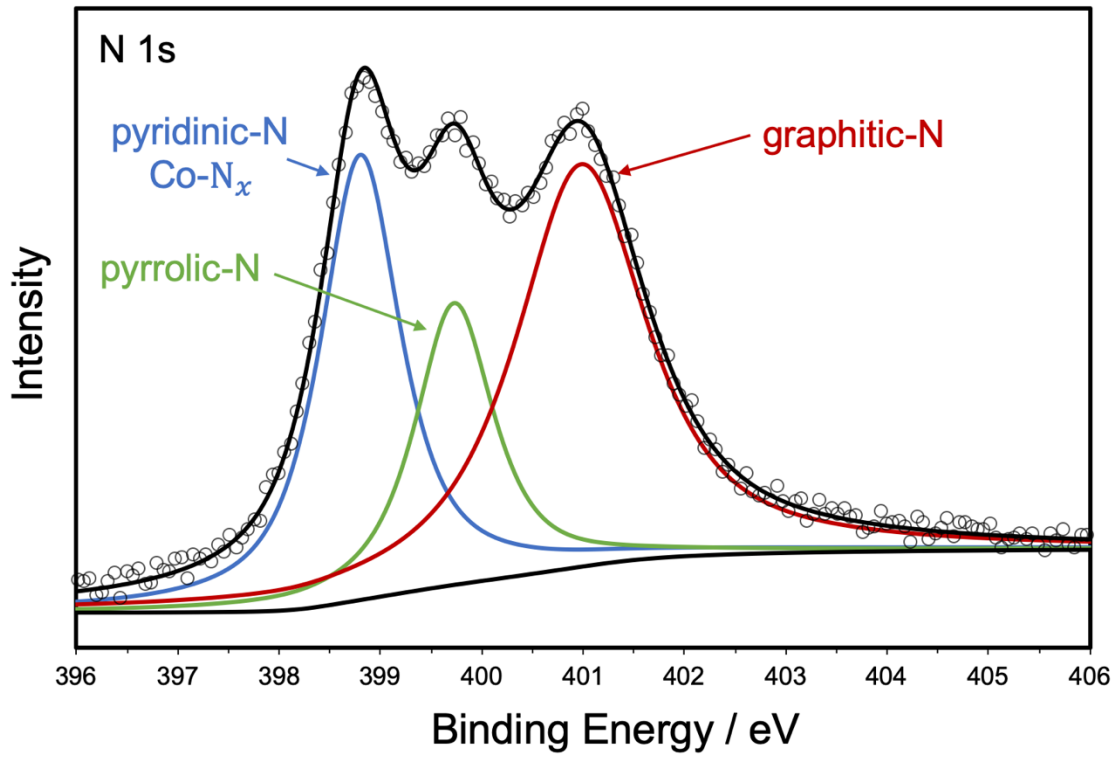

Figure 4.1. XPS spectra of N 1s.

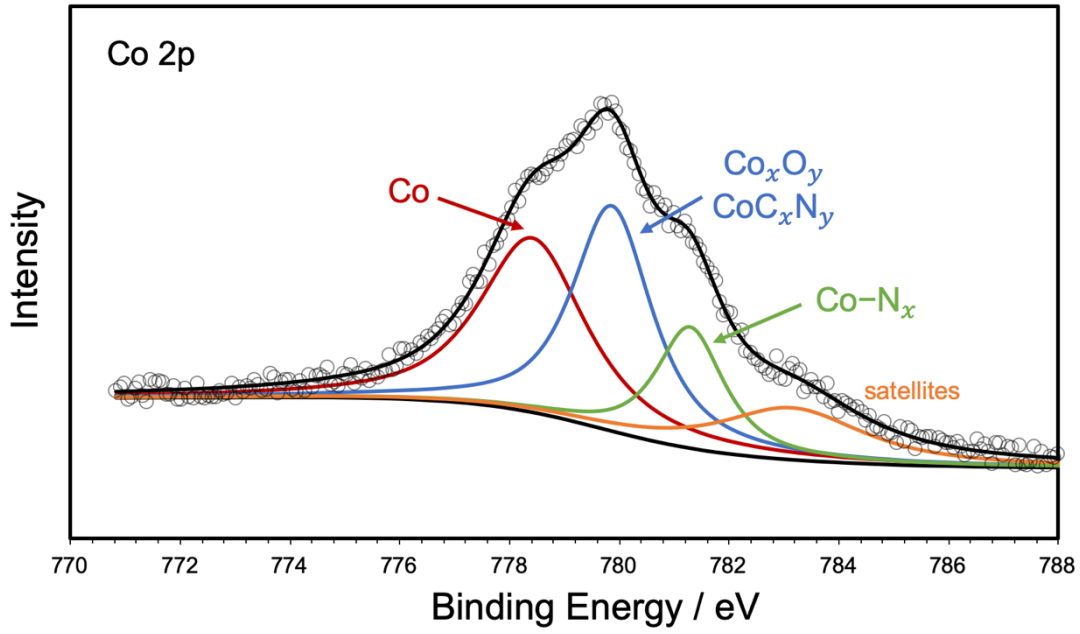

Figure 4.2. XPS spectra of Co 2p.

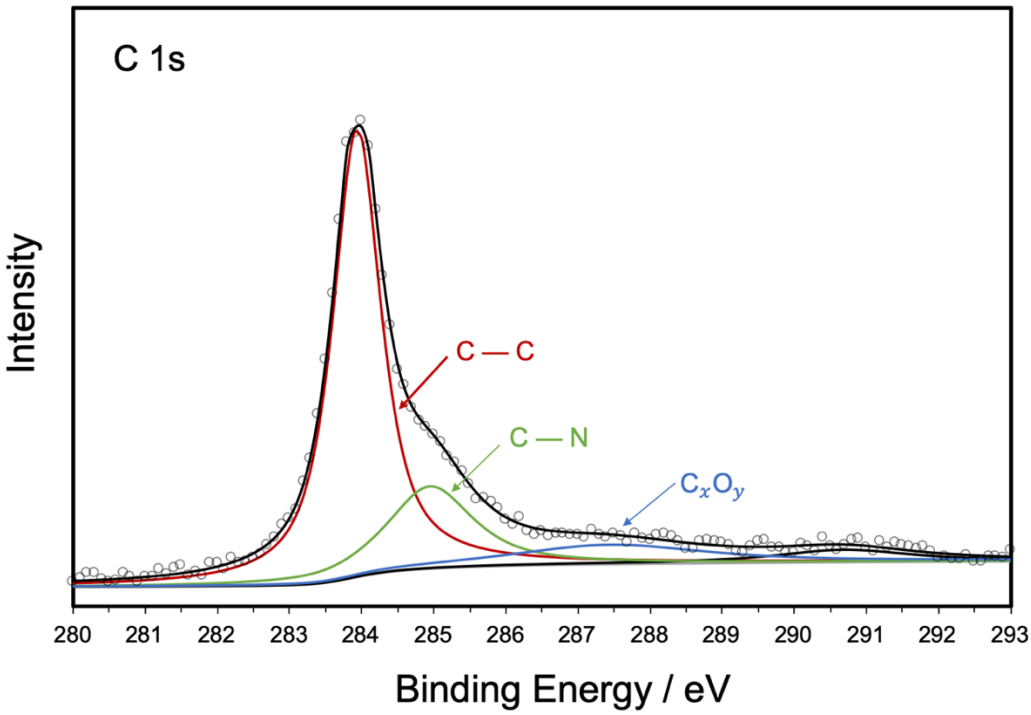

Figure 4.3. XPS spectra of C 1s.

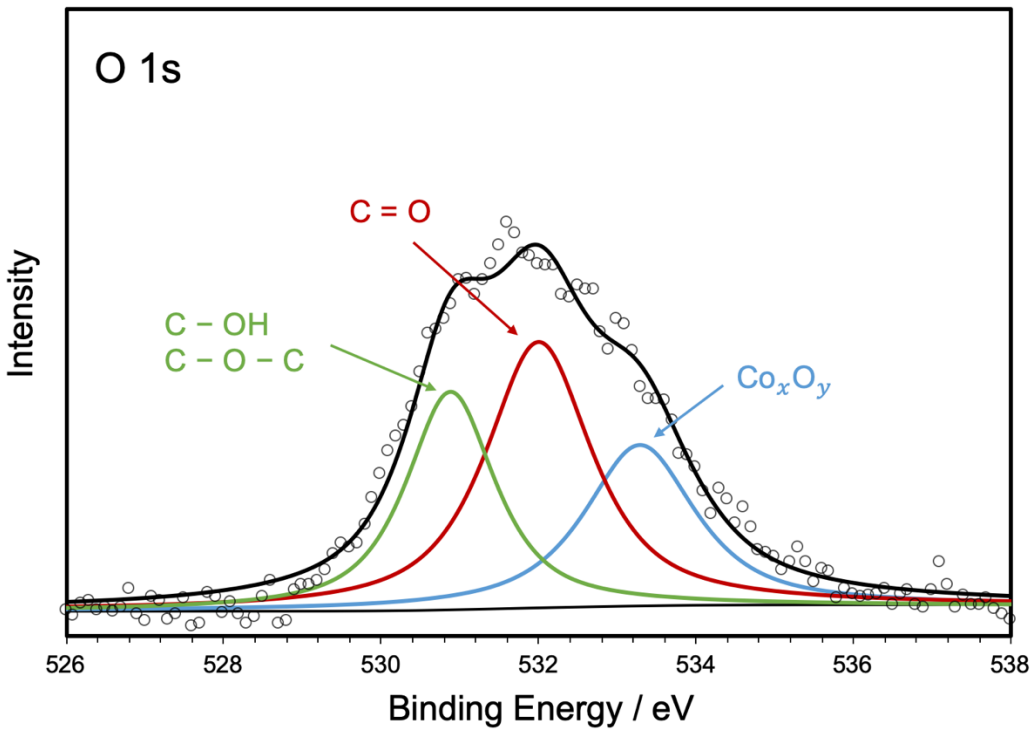

Figure 4.4. XPS spectra of O 1s.

From the XPS spectrum, supplementary information about C 1s and O 1s is shown in Figures 4.3 and 4.4. In the C 1s spectra, the most intense peak around 284.2 eV belongs to the graphitic structure (C — C) of CNTs. Peak around 285.5 eV belongs to the N-sp^2C structure. There is also some shake-up which comes from the C_xO_y fragments. In the O 1s spectra, oxide fragments of cobalt and carbon are consistent with the Co 2p and C 1s regions. Peak positions, components, and their compositions are summarized in Table 4.1.

Table 4.1. *Summary of N 1s and Co 2p components and compositions from XPS data.*

N 1s			**Co 2p**		
Component	**eV**	**%**	**Component**	**eV**	**%**
Pyridinic-N / Co-N_x	398.8	34.7	Co	778.5	40.8
Pyrrolic-N	399.8	18.7	CoC_xN_y / Co_xO_y	780.0	36.6
Graphitic-N	401.2	46.6	Co-N_x	781.4	22.6

4.1.2. Time-of-Flight Secondary Ion Mass Spectrometry (ToF-SIMS)

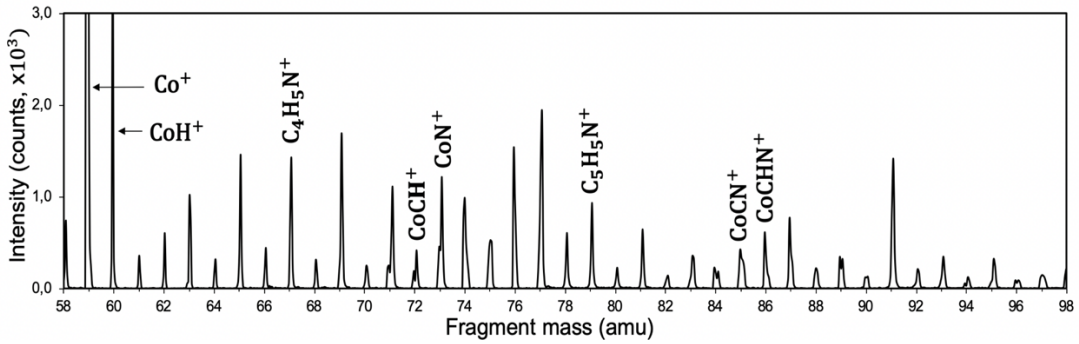

Figure 4.5. ToF-SIMS spectra of Co-N/MWCNT.

ToF-SIMS is a highly sensitive surface characterization method used for gathering analytical information about molecular structures of surfaces. From the high-resolution ToF-SIMS spectra (Figure 4.5 and 4.6), ion fragments of Co generally incorporated with N, H, and C. It was known that Co-based centers are considered as one of the favored sites for ORR. Furthermore, when comparing the amount of pyrrolic-N (C_4H_5N) and pyridinic-N (C_5H_5N) ions, intensities confirmed that the

deconvoluted triplet peaks obtained in the XPS analysis because the peak located at 398.8 eV belongs to both pyridinic-N and Co-N_x fragments in the catalyst. $CoCN^+$ ions were also observed around 85, but the molecular weights beyond 95 could not be directly attributed to CoN_xC_y due to a wide variety of ionic combinations.

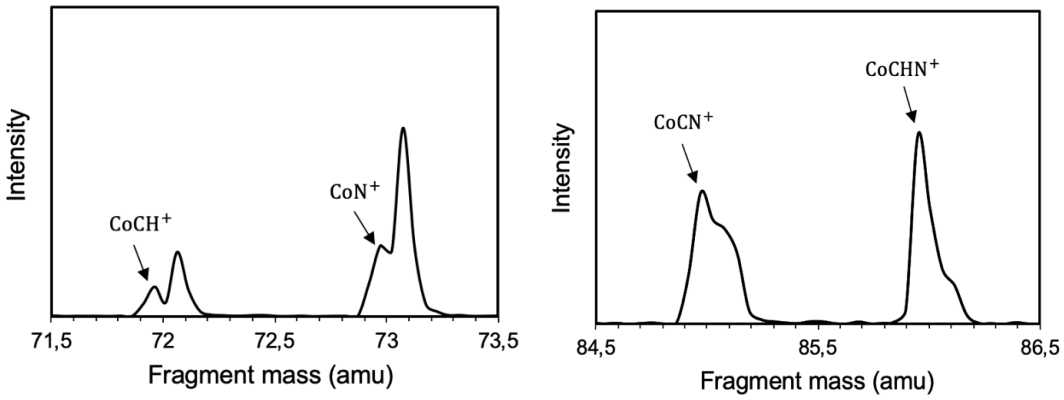

Figure 4.6. ToF-SIMS spectra of some Co-based fragments.

4.1.3. X-Ray Diffraction (XRD)

The corresponding XRD pattern (Figure 4.7) shows that the most intense peak, 2θ = 26°, is related to the crystallinity of multi-walled carbon-nanotubes and diffracted from (002) planes of the graphitic structure. Moreover, the XRD pattern concluded that the amount of crystalline cobalt species was relatively high, which is supportive information about the amount of metallic cobalt species in the Co 2p region in the XPS analysis. Peaks from the 2θ = 44.2°, 51.4°, 75.9° are related with the (100), (200) and (220) planes of metallic cobalt, which is in the form of the face-centered cubic structure. Parameters of high-temperature pyrolysis were sufficient enough to increase the amount of crystalline cobalt species [38,39]. In addition to that, the average crystallite size (L) of Co nanoparticles on N-doped carbon nanotubes was calculated as 7.43 nm using Scherrer equation (4.1) where $\lambda_{K\alpha}$ is the wavelength of X-ray (~0.154 nm), B is the FWHM in radians and θ is the Bragg angle at the peak maximum (see Appendix A for calculations).

$$L = \frac{0.89\,\lambda_{K\alpha}}{B_{(2\theta)}\cos\theta} \tag{4.1}$$

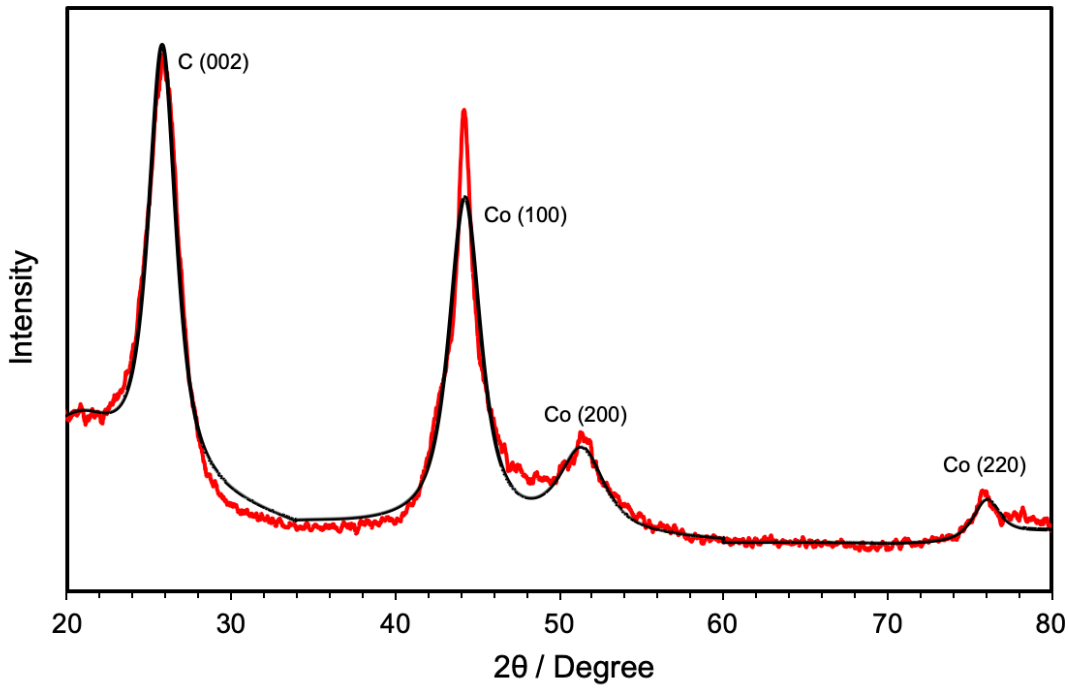

Figure 4.7. XRD spectra of synthesized Co-N/MWCNT electrocatalyst showing characteristic peaks of crystalline graphitic structure and platinum particles

However, due to the crystal imperfection and distortion, rearranging Scherrer equation (Eq 4.2) and importing strain induction (ε) with Williamson-Hall plot may give better results for estimating average Co crystallite size [76-78]. Using the datasets of Co (100), (200), and (220), the y-intersect of a "*BCosθ vs. 4Sinθ*" plot gave the more accurate crystallite size value, which was 6.23 ± 0.1 nm. (See Appendix A for calculations).

$$B_{(2\theta)}\cos\theta = \frac{0.89\,\lambda_{K\alpha}}{L} + 4\varepsilon\sin\theta \qquad (4.2)$$

So, results concluded that the pyrolysis parameters were sufficient enough to create stable and active Co-N_x sites in the complex. Graphitizing degree of the material further investigated by the dispersive Raman spectroscopy (D-Raman).

4.1.4. Dispersive Raman Spectroscopy (D-Raman)

From the Raman spectra, typical G (1584 cm^{-1}) and D (1345 cm^{-1}) bands generally give a hint about the quality of carbon-based catalysts by evaluating graphitization of

the structure. G band represents the hexagonally sp^2-hybridized carbon atoms in the network, showing the integrity of the graphene layer. In contrast, the D band is related to the disordered carbon defect sites in the framework. From the spectra (Figure 4.8), the ratio of the I_D/I_G was determined as 1.25, meaning that the amorphous nature of Co-N/MWCNT has slightly weaker graphitization, which results in a high amount of active distortions.

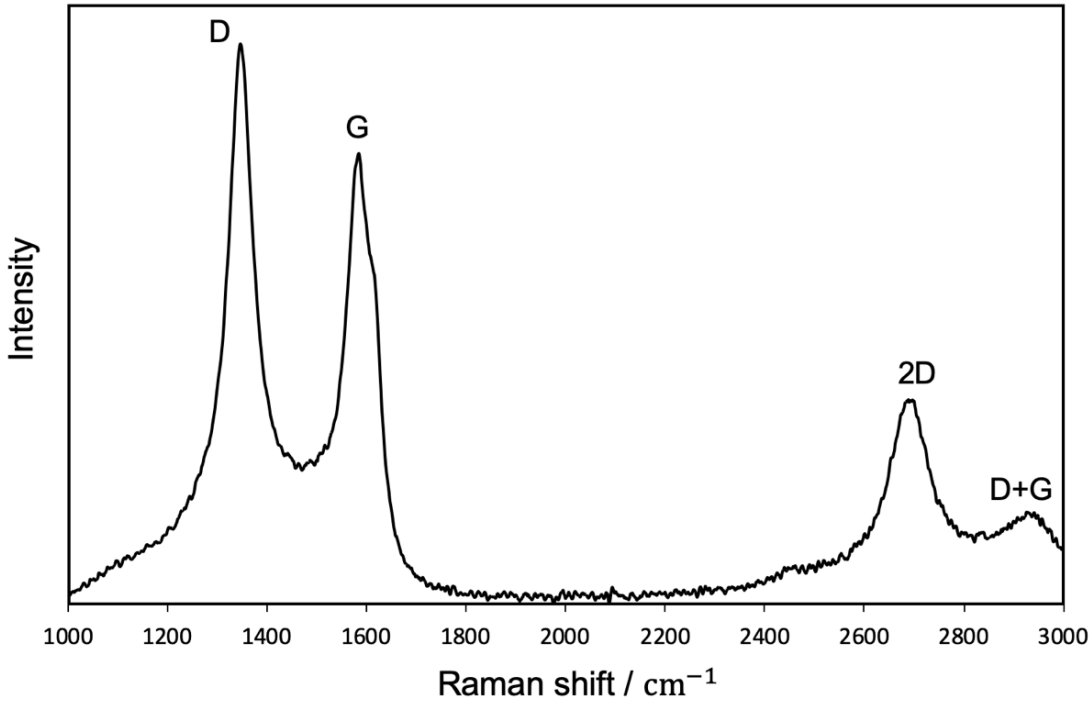

Figure 4.8. Raman spectra of Co-N/MWCNT catalyst.

Increasing the pyrolysis temperature may increase the crystallization of carbons, which led to an increase in the formation of stable C-C bonds, but this brings the problem of decreasing N-C active sites, which is strictly essential for catalytic properties. Due to a lower fraction of sp^2-hybridized carbons, the formation of active amorphous Co-N_x sites might be favored during pyrolysis around 700°C. Raman spectroscopy may also provide further information about the layers of the graphite that can be obtained by the I_{2D}/I_G ratio, which was around 0.5, and it confirmed the multi-layered structure of the carbon nanotubes.

4.1.5. High-Resolution Transmission Electron Microscopy (HR-TEM)

Being an essential tool for morphological characterization, TEM images were also supplementary to previously discussed characterizations. As shown in the TEM images, Co nanoparticles with relatively uniform size are distributed homogeneously along the multi-walled carbon nanotubes. From the high-magnification images (Figure 4.12), the Sauter mean-particle diameter (d_{32}) of Co nanoparticles was calculated as 8.47 nm, which is in good agreement with the XRD and proves the uniform dispersion along the carbon nanotubes. However, due to the crystal growth during the high-temperature pyrolysis, the presence of larger diameter nanoparticles (>20 nm) was also non-negligible. Furthermore, high-magnification images revealed that the presence of nitrogen-carbon layers that encapsulated Co spheres, which are thought to be the main formation sites of Co-N_4 structure. As additional information, lattice planes of cobalt nanoparticles (mostly (100)) and carbon nanotubes (verified by D-Raman) can also be observed from the HR-TEM images (Figure 4.11).

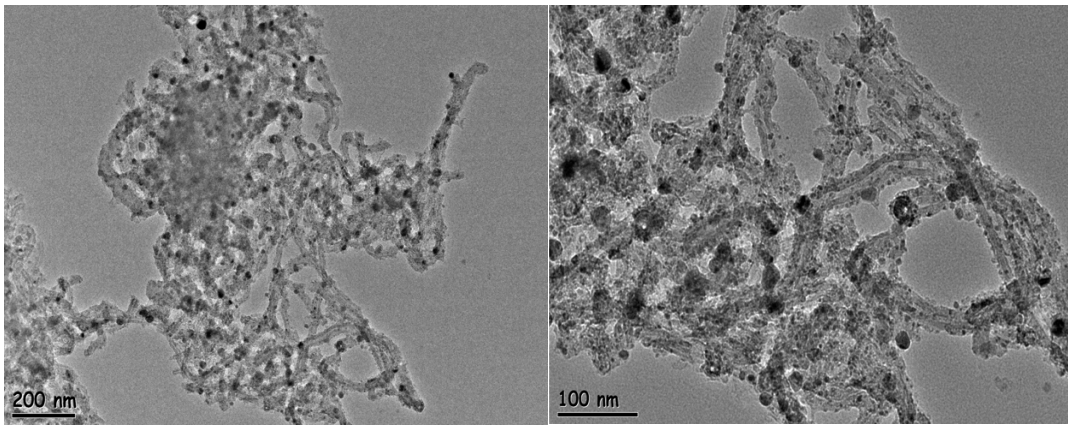

Figure 4.9. TEM images with different magnifications.

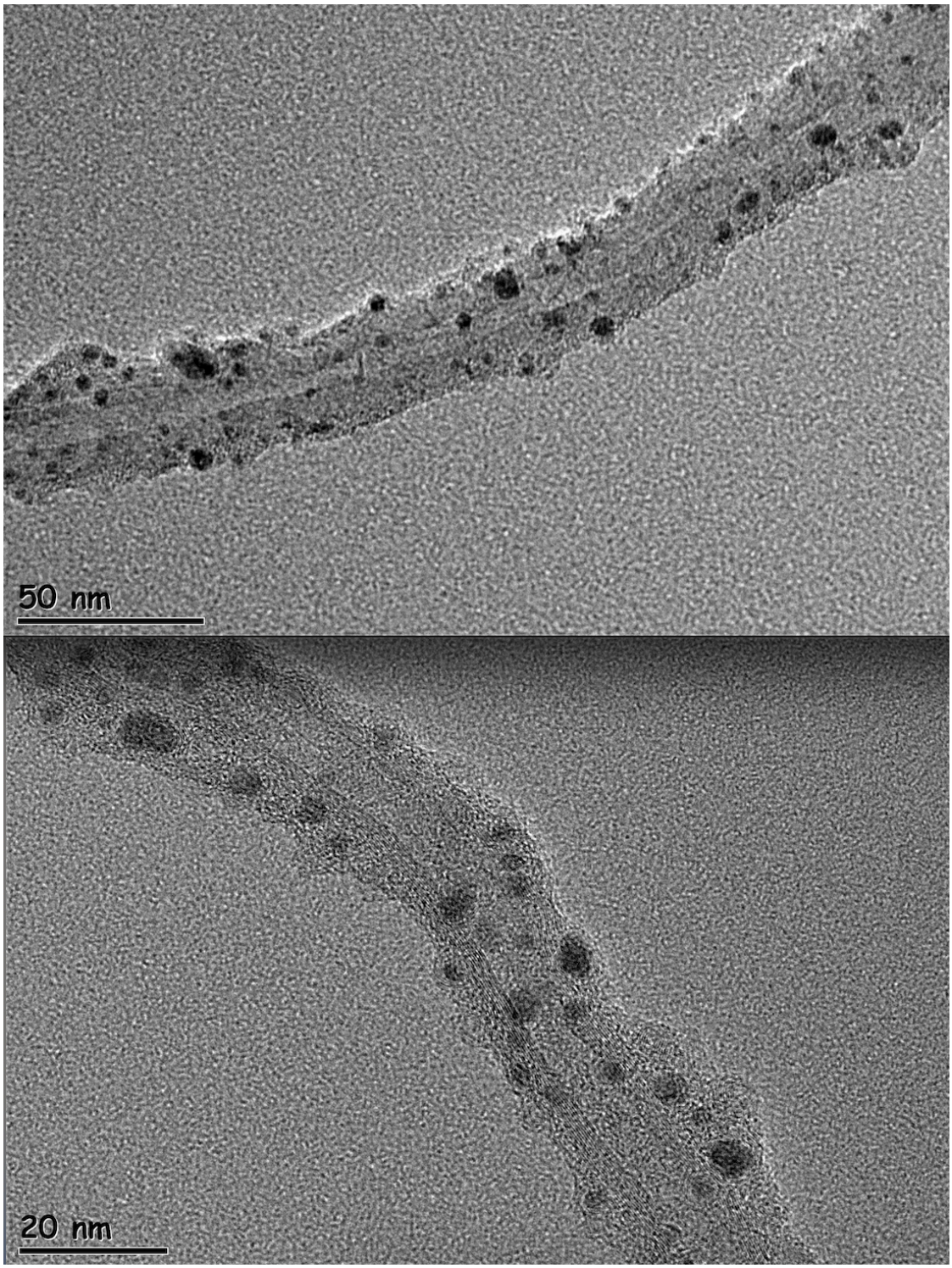

Figure 4.10. TEM images with different magnifications.

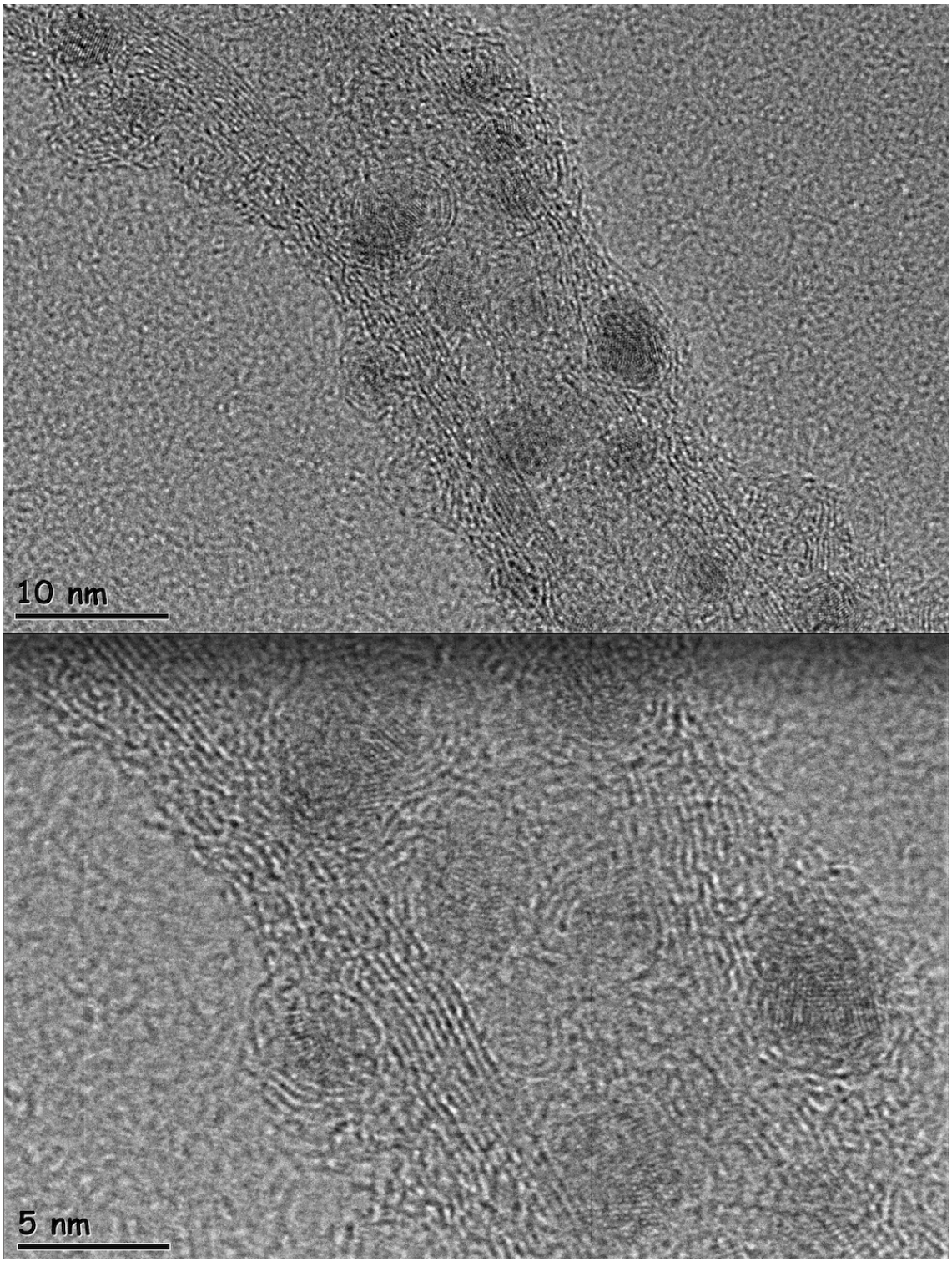

Figure 4.11. TEM images with different magnifications.

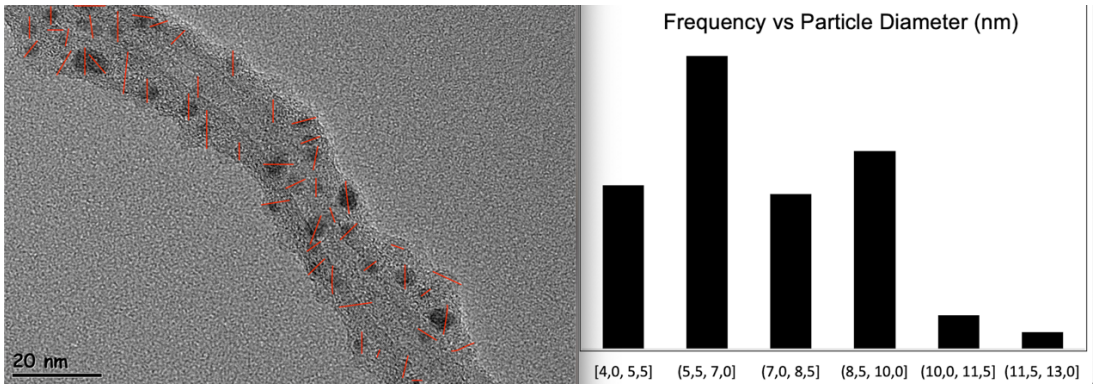

Figure 4.12. Particle size distribution from the HR-TEM image.

Specific surface area (SSA) of cobalt nanoparticles was calculated (Eq. 4.3) as 80 $m^2 \cdot g^{-1}$ by taking Sauter-mean-diameter (d_{32}) as 8.47 nm where ρ_{Pt} is the density of Pt and *d* is the diameter of Pt nanoparticles (See Appendix A for calculations).

$$SSA_{Co} = \frac{6000}{\rho_{Co}\, x\, d[3,2]}\ ,\ d\ [3,2] = \frac{\Sigma n_i\, d_i^3}{\Sigma n_i\, d_i^2} \tag{4.3}$$

4.2. Rotating Disc Electrode (RDE) Measurement

RDE plots (j_{app} vs. potential) and ($1/j_{app}$ vs. $1/\omega^{1/2}$) were shown in Figure 4.13 and 4.14 and analyzed through the Koutecky–Levich equation expressed as below where j_{app} is apparent current density and ω is the rotation rate ($rad \cdot s^{-1}$); *F* is Faraday constant (96485 $A \cdot s \cdot mol^{-1}$); C_{O_2} ($1.13 \cdot 10^{-6}$ $mol \cdot cm^{-3}$) is the saturated concentration of oxygen, D_{O_2} ($1.80 \cdot 10^{-5}$ $cm \cdot s^{-1}$) is the diffusion coefficient of oxygen; ν ($1.01 \cdot 10^{-2}$ $cm^2 \cdot s^{-1}$) is the kinematic viscosity of the solution. All the constants were collected from the literature for 0.5M H_2SO_4 solution [83,84].

$$\frac{1}{j} = \frac{1}{j_k} + \frac{1}{j_d} = \frac{1}{j_k} + \frac{1}{0.62nFC_{O_2}D_{O_2}^{2/3}\nu^{-1/6}\omega^{1/2}} \tag{4.4}$$

The number of transferred-electron (*n*) for O_2 reduction can be extracted from the slope of ($1/j_{app}$ vs. $1/\omega^{1/2}$), and kinetic current density (j_k) can be extracted from the y-intersection.

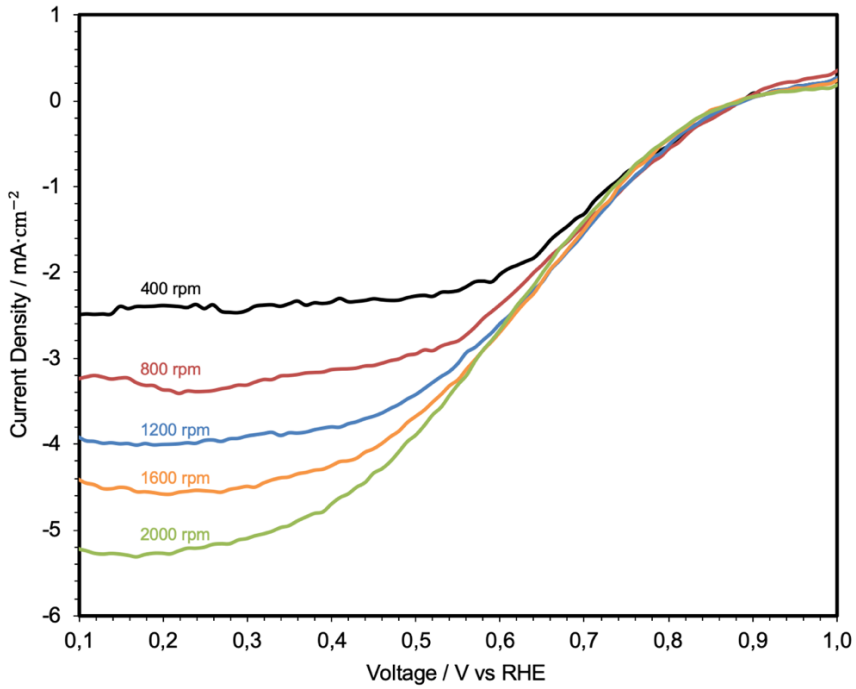

Figure 4.13. LSV polarization curves at different rotation rates for ORR.

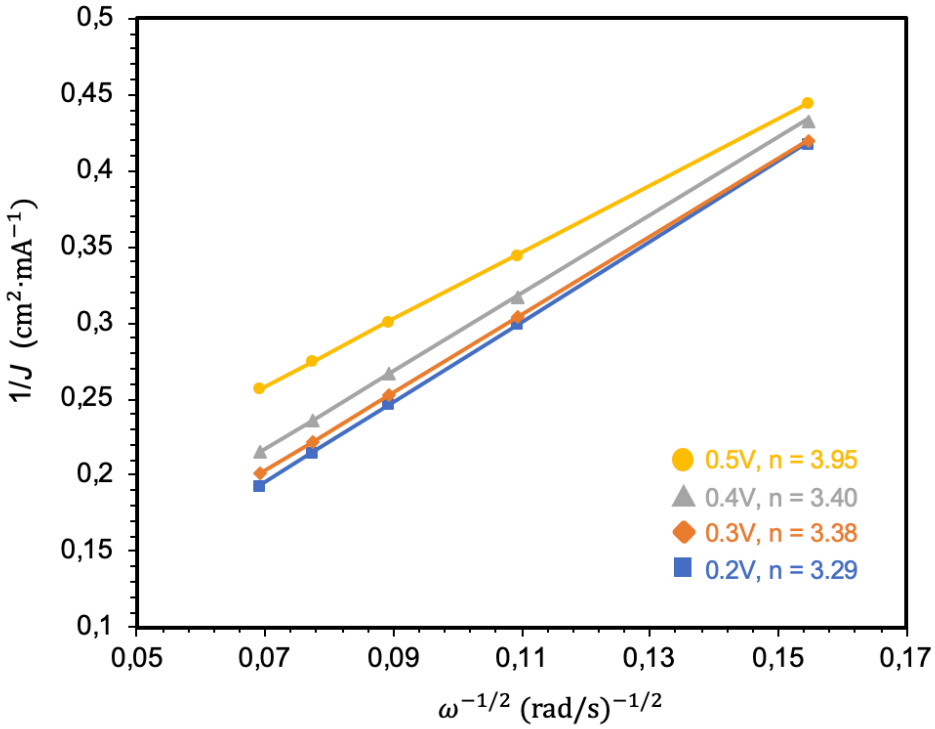

Figure 4.14. Koutecky-Levich plots at 0.2V, 0.3V, 0.4V, and 0.5V.

As a result, the K-L plot gave relatively good linearity at potentials between 0.2 and 0.5V. From the K-L plot (See Appendix A for calculations), the apparent number of

the transferred-electron (n) for oxygen reduction reaction was calculated (Eq. 4.4) as 3.29 at 0.2V, and increased to 3.95 at 0.5V, suggesting that the reaction mainly occurs through the four-electron transfer. The formation of water molecules through the $4e^-$ pathway is the most efficient and desired mechanism considering the development of electrocatalytic materials for fuel cell applications. On the other hand, there might be a small fraction of the two-electron pathway, which could be attributed to H_2O_2 formation through the pyrrolic-N fragments. However, comparing it with the direct-reduction, poisoning effect of HO_2^- was negligible. Furthermore, onset potential (E_{onset}), half-wave potential ($E_{1/2}$), and diffusion-limiting current density (j_d at 1200 rpm) were calculated as 0.83V (vs. RHE), 0.67V (vs. RHE), and 4.53 $mA \cdot cm^{-2}$ respectively. Especially in the lower overpotential regions, the study verified that the Co-N/MWCNT catalyst has decent electrochemical performance for the oxygen reduction reaction (ORR). For the comparison, LSV curves of Pt/C and Co-N/MWCNT catalysts at 1200 rpm prove that they have relatively same onset (E_{onset}) and halfwave potential ($E_{1/2}$) with an almost identical current density (Figure 4.15).

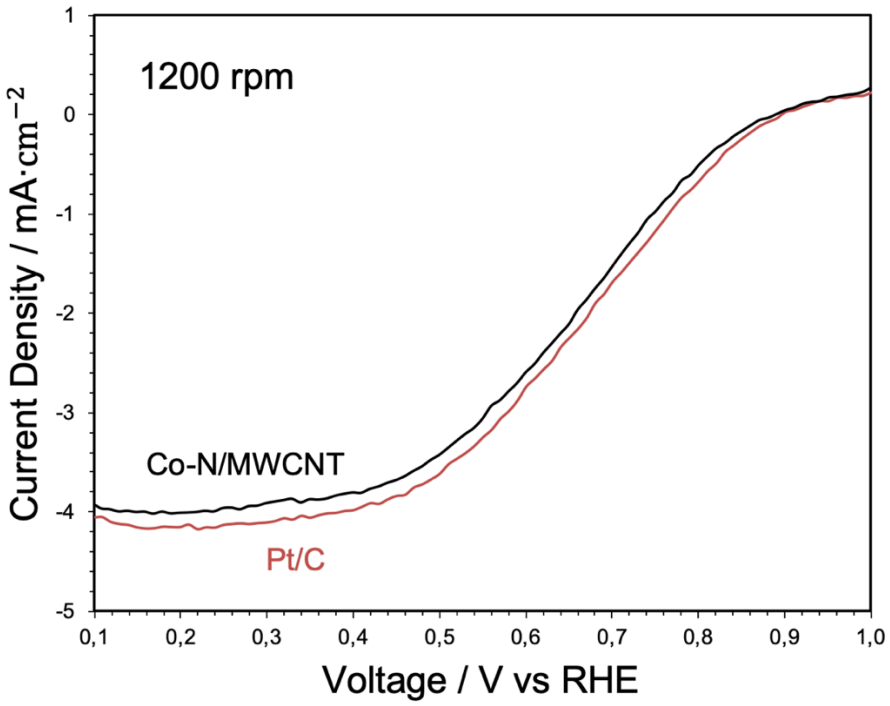

Figure 4.15. LSV curves of Pt/C and Co-N/MWCNT at 1200 rpm.

Table 4.2. *ORR performance of Co-N/MWCNT and comparison with the literature.*

Catalyst	Catalyst Loading ($mg \cdot cm^{-2}$)	E_{onset} (V)	$E_{1/2}$ (V)	$(n)_{max}$	Ref.
Co-N/MWCNT	0.400	0.83	0.67	3.95	This work
Co-N/C	0.600	0.83	0.65	2.60	[38]
Co-N/C	0.425	0.72	0.62	3.22	[35]
Co-N/C	0.100	0.72	0.60	3.17	[85]
Pt/C	0.02 (wt. Pt)	0.87	0.70	-	This work
Pt/C	0.014 (wt. Pt)	0.85	0.68	3.99	[85]

4.3. High-Temperature PEM Fuel Cell Test

The performance of a Co-N/MWCNT based MEA is summarized in Figure 4.16. Comparison of Co-N/MWCNT to the reference MEA (Pt/C for both anode and cathode) is outlined in Table 4.3. OCV of Co-N/MWCNT was found to be around 0.96V, and OCV of the Pt/C was wound to be around 0.94, at all temperatures. Many hypotheses conclude that the OCV difference can be attributed to the hydrogen crossover, resulting in an oxygen reduction reaction overpotential at the cathode. Because crossover current due to oxygen permeation does not affect the anode overpotential [92]. The initial assessment shows that the Co-N/MWCNT catalyst has slightly less parasitic reactions at the cathode site. In the RDE analysis, typical ORR performances of Co-N/MWCNT and Pt/C in an acidic electrolyte were found very similar. But, in the HT-PEMFC operation, Co-N/MWCNT catalyst was superior to the commercial Pt/C, especially at the 150°C and 160°C. It is thought that the main reason for that is the higher cathodic loading of Co-N/MWCNT (3.0 $mg \cdot cm^{-2}$) and three-dimensional support material, which enhances activity. On the other hand, it was observed that the performance of the Co-N/MWCNT catalyst was significantly decreased while increasing the temperature. This could be attributed to the higher operating temperatures, which may accelerate the oxidation of cobalt species and decomposition of nitrogen complexes leading to some stability problems at elevated temperatures.

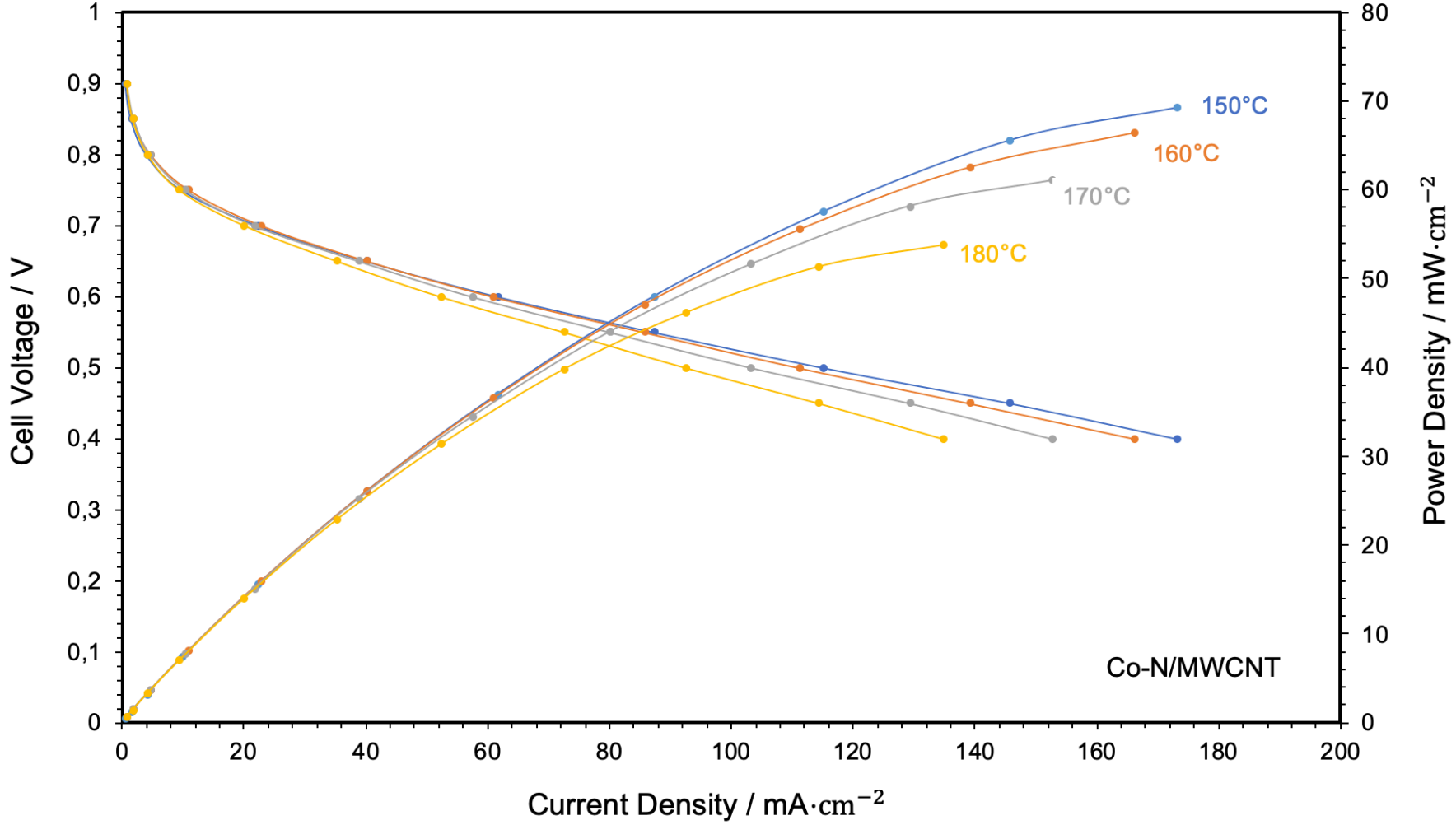

Figure 4.16. HT-PEMFC polarization curves of Co-N/MWCNT catalyst at different temperatures.

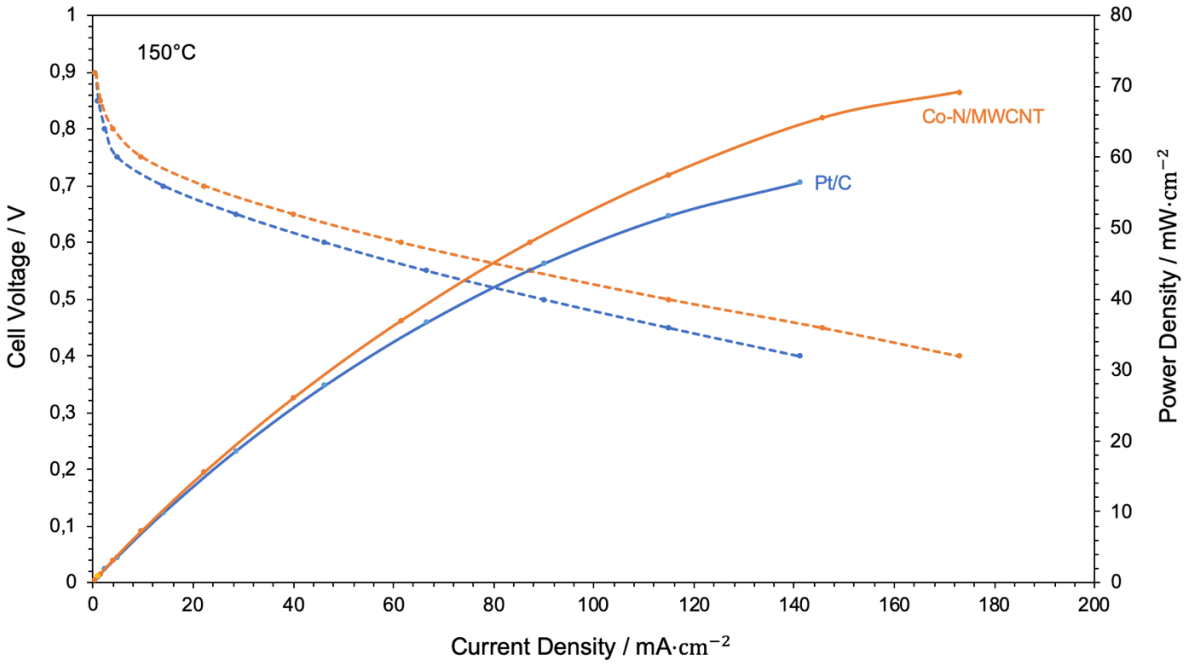

Figure 4.17. Voltage, current & power density curves of Co-N/MWCNT and reference Pt/C at 150 ℃.

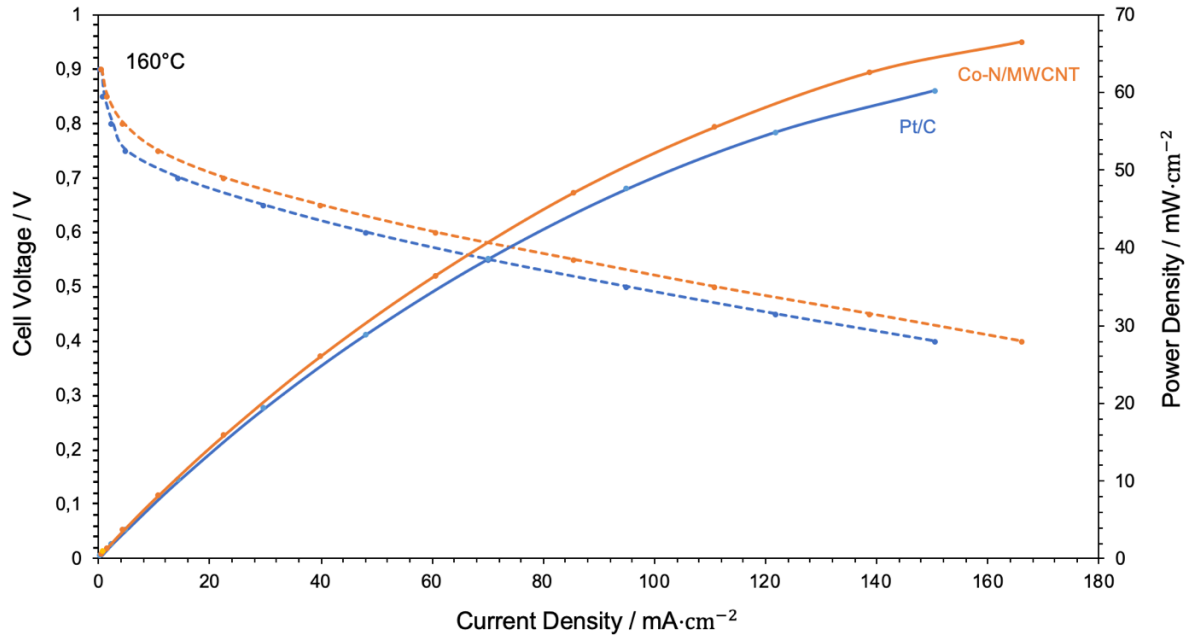

Figure 4.18. Voltage, current & power density curves of Co-N/MWCNT and reference Pt/C at 160 ℃.

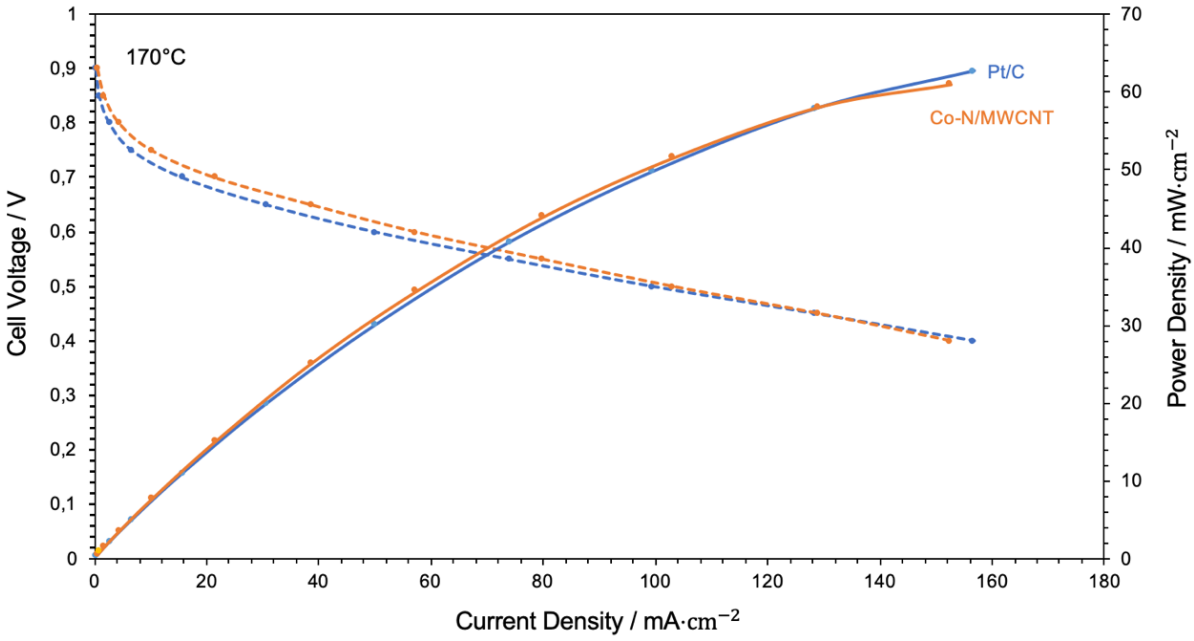

Figure 4.19. Voltage, current & power density curves of Co-N/MWCNT and reference Pt/C at 170 ℃.

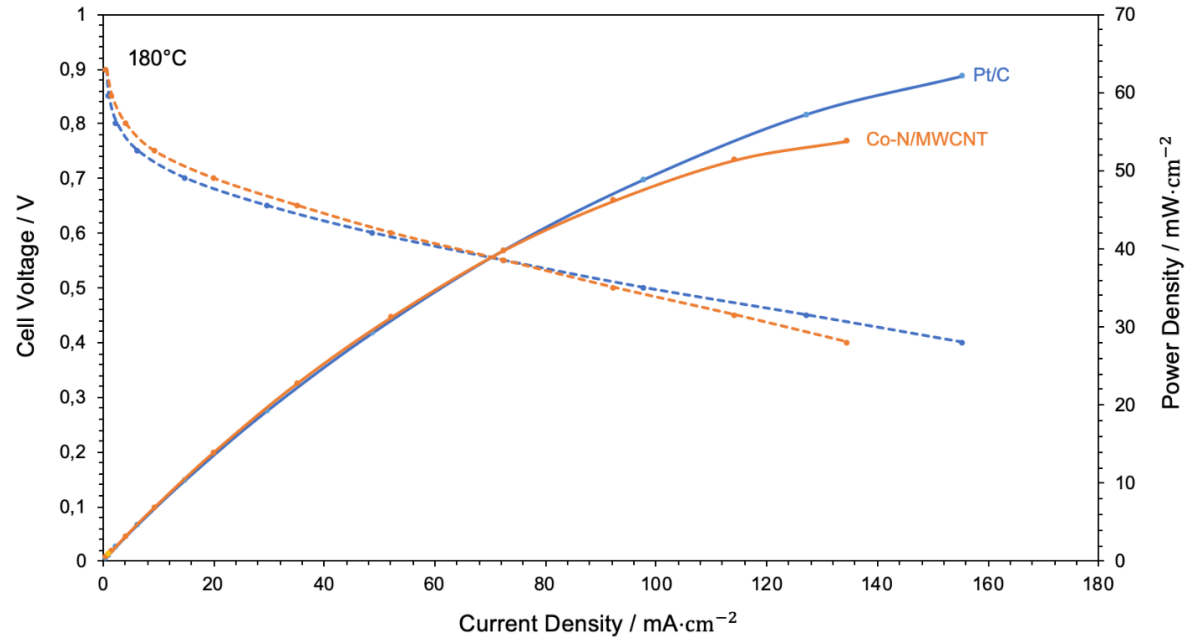

Figure 4.20. Voltage, current & power density curves of Co-N/MWCNT and reference Pt/C at 180 ℃.

At 170°C, Co-N/MWCNT and Pt/C had nearly the same performance. At 180°C, Co-N/MWCNT lost 25% of its initial performance and became inferior to Pt/C. Operating temperature is very important and must be carefully controlled to avoid significant performance losses because combining it with the acid, higher operating temperatures may deteriorate electrodes under the long-term operations. In this study, current and power density values were found to be relatively lower than that in the LT-PEMFC's according to the literature. As pointed out, this could be attributed to Warburg impedance in the lower-frequency regions at higher temperatures [87]. A comparison of Co-N/MWCNT to the reference MEA (Pt/C for both anode and cathode) is summarized in Table 4.3. Single-cell fuel cell test results were very supportive. They proved that the Co-N/MWCNT electrocatalyst could be the promising alternative to noble Pt/C catalyst at the cathode site, especially for the lower boundary of high-temperature PEMFC applications. Detailed polarization curves of Pt/C vs. Co-N/MWCNT at different temperatures are summarized in Figure 4.17 to 4.20.

Table 4.3. *Summary of single-cell HT-PEMFC performance of Co-N/MWCNT and Pt/C.*

Cathode	**OCV**	**P_{max} ($mW \cdot cm^{-2}$)**	**I_{max} ($mA \cdot cm^{-2}$)**	**$I_{0.6V}$ ($mA \cdot cm^{-2}$)**
Co-N/MWCNT, 150°C	0.96 V	69	173	62
Co-N/MWCNT, 160°C	0.96 V	66	166	61
Co-N/MWCNT, 170°C	0.96 V	61	152	57
Co-N/MWCNT, 180°C	0.96 V	53	134	52
Pt/C, 150°C	0.94 V	57	141	47
Pt/C, 160°C	0.94 V	60	150	48
Pt/C, 170°C	0.94 V	62	156	50
Pt/C, 180°C	0.94 V	62	155	49

CHAPTER 5

RESULTS & DISCUSSIONS FOR Pt-PBI/MWCNT

SYNTHESIS AND CHARACTERIZATION OF Pt-PBI/MWCNT COMPOSITE ELECTROCATALYST AND EVALUATION OF ITS PERFORMANCE IN HT-PEM FUEL CELL

5.1. Physico-Chemical Characterizations

5.1.1. Thermogravimetric Analysis (TGA)

The thermogravimetric analysis (TGA) aims to examine the decomposition behavior of catalyst at elevated temperatures, and the amount of metallic Pt over PBI wrapped carbon-nanotubes. TGA curve (Figure 5.1) revealed that there are three significant weight reductions at around 200°C, 380°C, and 800°C. The first one is attributed to the dehydration of residual acid molecules in the complex, including (-COOH) functionalized sites of MWCNTs and volatiles. The second one belongs to the simultaneous decomposition of wrapping polymer (PBI) film and multi-walled carbon nanotubes. The final one, around 800°C, is thought to be related to the decomposition of retained agglomeration of larger diameter carbon-nanotubes. Also, it was indicated that there was no significant weight reduction at the typical operating range (150°C - 180°C) of HT-PEMFCs. At the end of the analysis, the amount of Pt nanoparticles in the composite was calculated as ~39 wt%, which means that ~98% of fed-Pt was loaded onto the surface of PBI/MWCNT support material. Such a high yield demonstrates that the success of decreasing the amount of Pt waste and lowering the cost of the electrocatalyst.

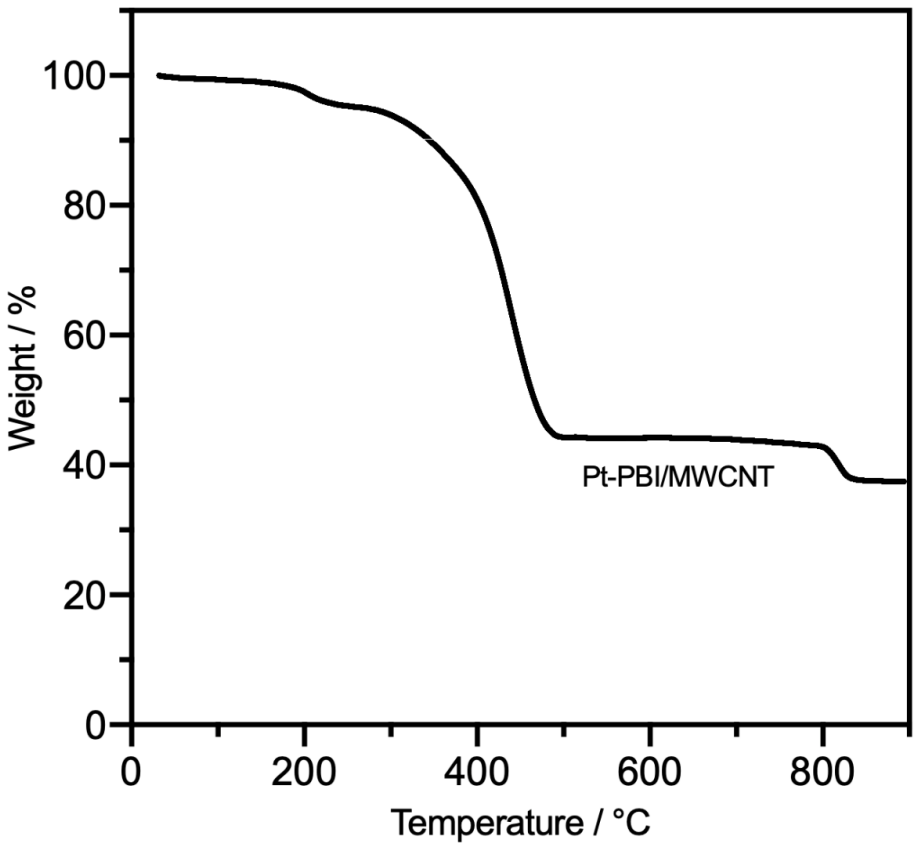

Figure 5.1. TGA curve of Pt-PBI/MWCNT electrocatalyst under air at a heating rate of 5 °C min^{-1} showing temperature-dependent weight loss of the catalyst powder.

5.1.2. X-Ray Photoelectron Spectroscopy (XPS)

From the XPS spectra (Figure 5.2), two of the peaks with the highest intensity belong to the spin-orbital splitting of Pt (0). Double peaks at 71.3 and 74.4 eV are related to Pt (0) $4f_{7/2}$ and $4f_{5/2}$, respectively. Having zero dominant valences demonstrates that the Pt nanoparticles were reduced appropriately by the microwave irradiation to ensure better electrochemical performance. Further analysis exhibited deconvoluted doublet peaks of Pt (II) around 76.0 eV and 72.8 eV, related to the oxide complex of Pt (PtO). Moreover, the XPS analysis proves that the presence of N 1s peaks around 399.6 eV and 400.0 eV are directly related to the presence of Polybenzimidazole (PBI) in the catalyst (Figure 5.3).

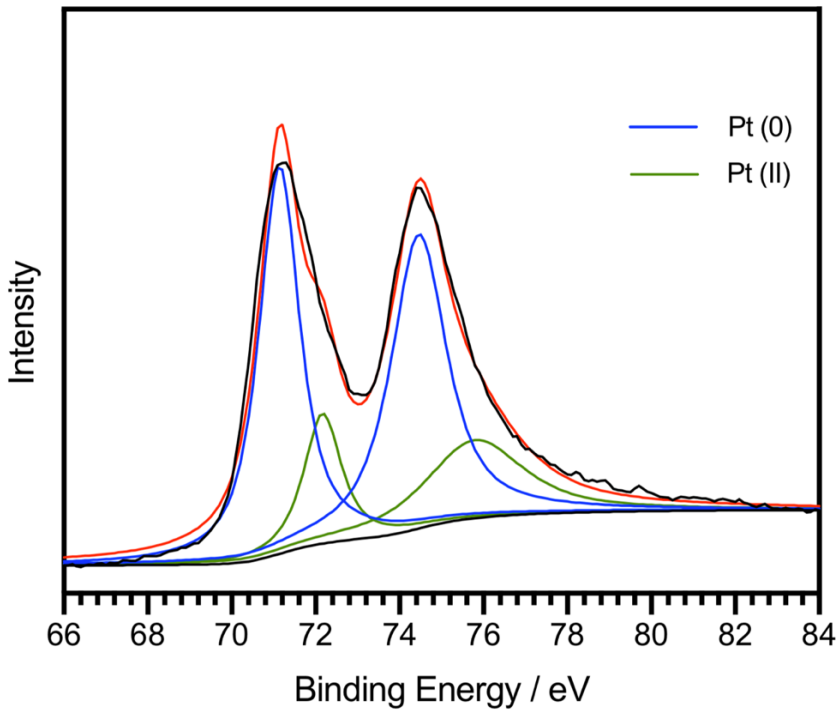

Figure 5.2. High-resolution XPS spectra of core level platinum 4f region showing its valence states.

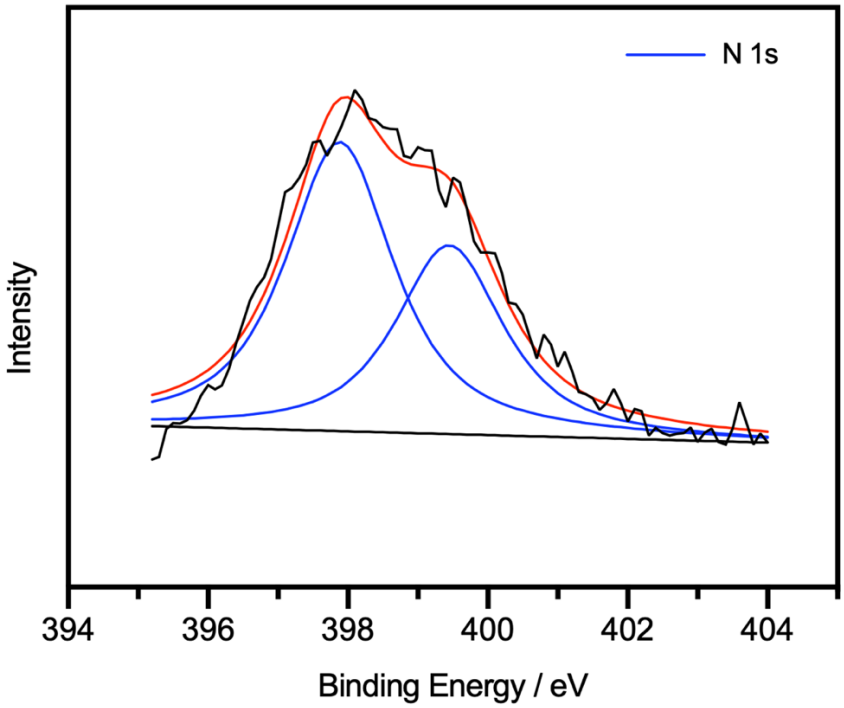

Figure 5.3. Core level nitrogen 1s region showing doublet peaks related to the presence of PBI in the framework.

5.1.3. X-Ray Diffraction (XRD)

The corresponding XRD pattern (Figure 5.4) shows that the most intense peak, 2θ = 25.8°, is related to the crystallinity of multi-walled carbon-nanotubes and diffracted from (002) planes of graphitic structure. The characteristic peaks of Pt (111), (220) and (311) are revealed at 2θ = 39.7°, 67.5°, and 81.0°, respectively. The diffraction peak around 2θ = 46° may belong to both Pt (200) and C (001), further deconvolution may also provide extensive information about the exact locations of the peaks. In the sample, the average crystallite size (L) of Pt nanoparticles was estimated from the full-width at half-maximum (FWHM) of the peak 2θ= 67.5° with using Scherrer equation (Eq 5.1) where $\lambda_{K\alpha}$ is the wavelength of X-ray (~0.154 nm), B is the FWHM in radians and θ is the Bragg angle at peak maximum.

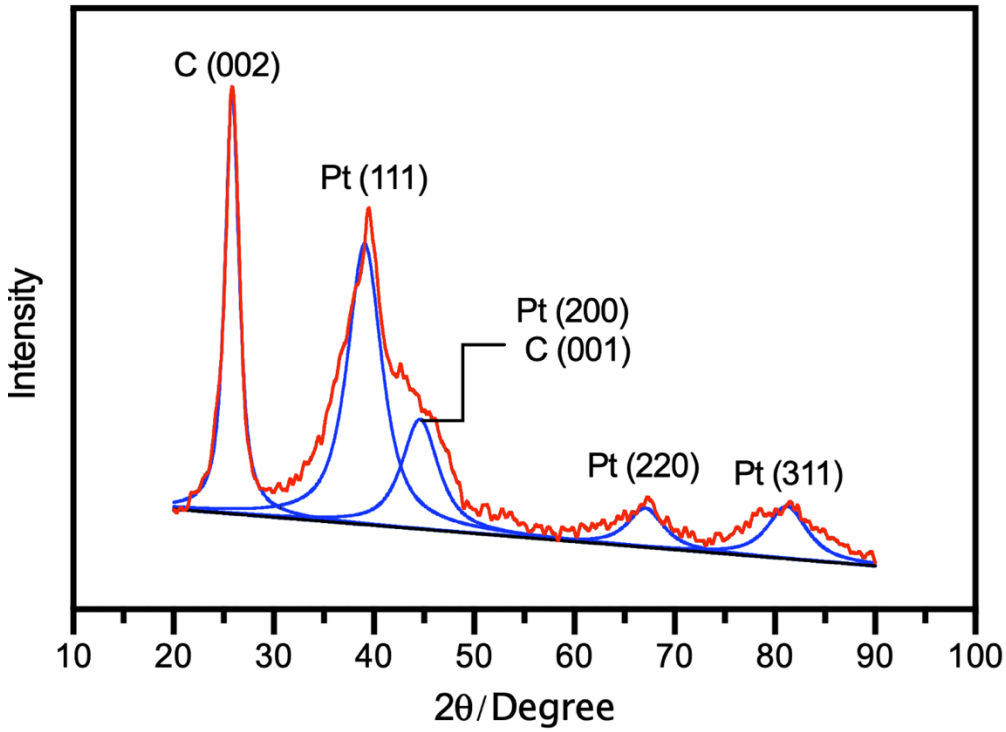

Figure 5.4. XRD spectra of synthesized Pt-PBI/MWCNT electrocatalyst showing characteristic peaks of crystalline graphitic structure and platinum particles.

$$L = \frac{0.89\,\lambda_{K\alpha}}{B_{(2\theta)}\cos\theta} \qquad (5.1)$$

Using the Scherrer equation (5.1), the average diameter of the Pt crystallites on the PBI/MWCNT was calculated as 1.94 nm. However, due to the crystal imperfection and distortion, rearranging Scherrer equation (Eq 5.2) and importing strain induction (ε) with Williamson-Hall plot may give better results for estimating average Pt crystallite size [76-78]. Using the datasets of Pt (111), (200), (220) and (311), the y-intersect of a "*BCosθ vs. 4Sinθ*" plot gave the more accurate crystallite size value which was 1.99 ± 0.1 nm. (See Appendix B for calculations).

$$B_{(2\theta)}\cos\theta = \frac{0.89\,\lambda_{K\alpha}}{L} + 4\varepsilon\sin\theta \qquad (5.2)$$

5.1.4. Transmission Electron Microscopy (TEM)

Being an essential tool for morphological characterization, TEM images (Figure 5.5, 5.6, and 5.7) were also supplementary to previously discussed characterizations. As shown in the TEM image (Figure 5.6), the Pt nanoparticles are somehow distributed along the multi-walled carbon nanotubes. But it is thought that the thin polybenzimidazole film might allow the growth of larger platinum nanoparticles consisting of many crystallites. With the assistance of the high-magnification image analysis (Figure 5.5), the Sauter mean-particle diameter (d_{32}) of Pt nanoparticles was calculated as 4.9 nm. From the TEM image (Figure 5.7), a thin polymer layer over the nanotubes can also be observed, and correlated with the signals in the core level nitrogen spectra. The thickness of the layer (r_{PBI}) was calculated as ~3 nm.

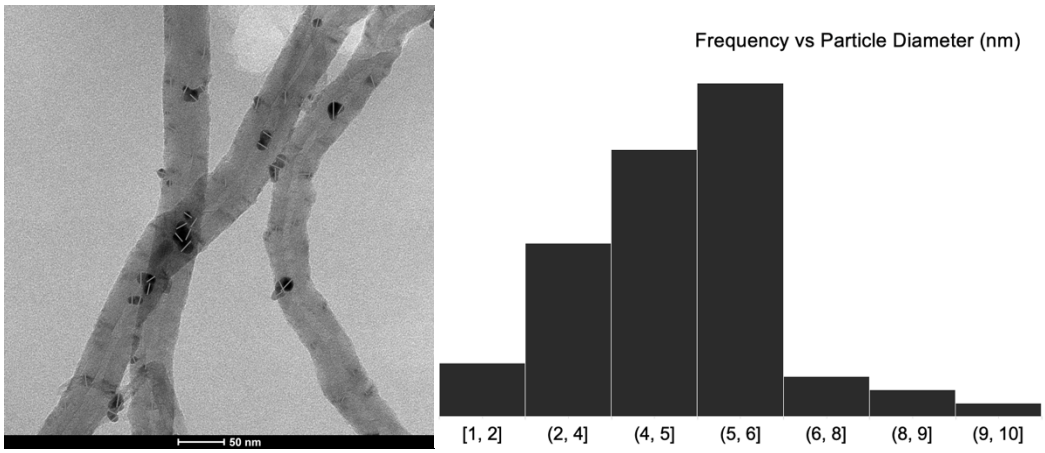

Figure 5.5. Particle size distribution from the TEM image.

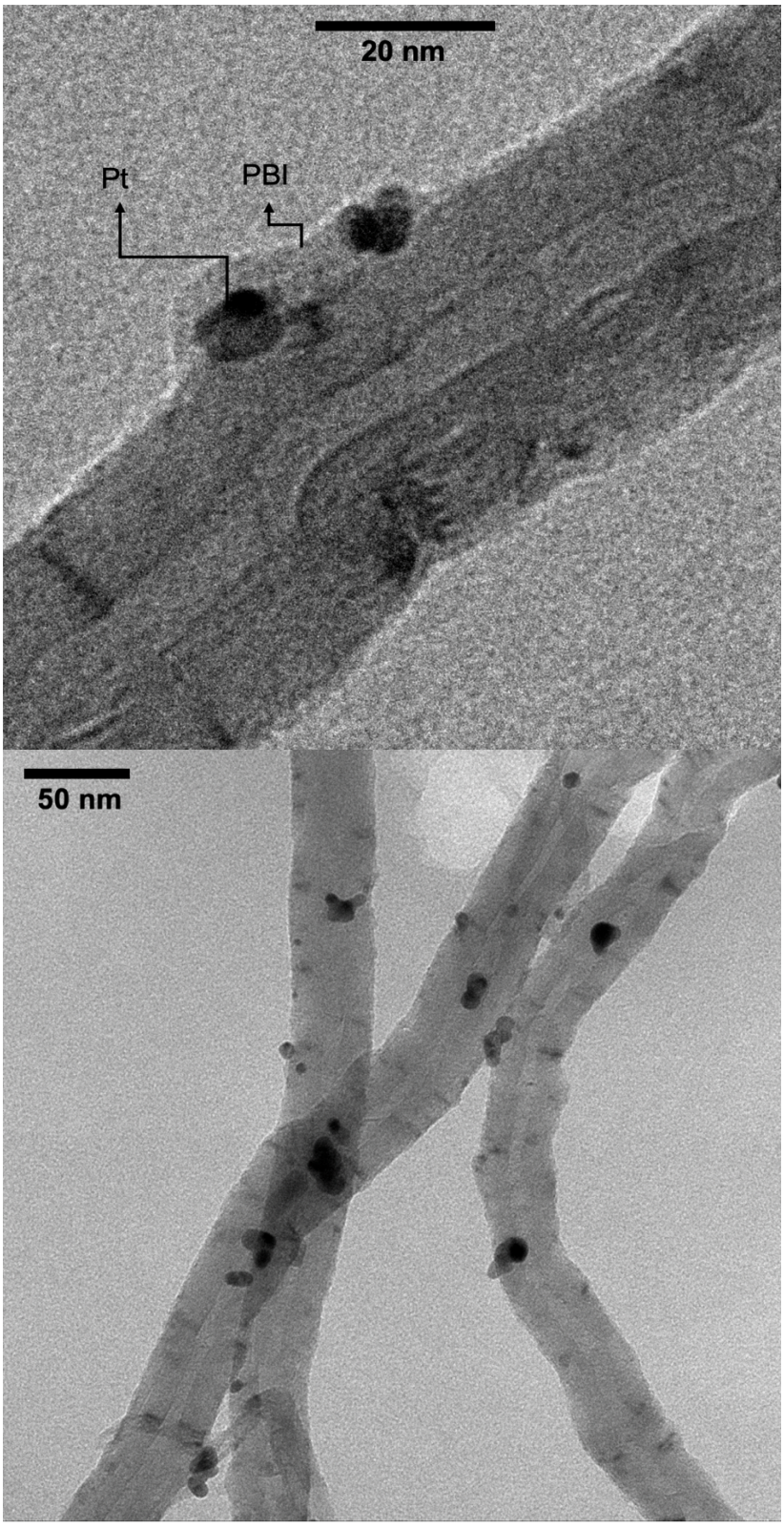

Figure 5.6. TEM images with different magnifications.

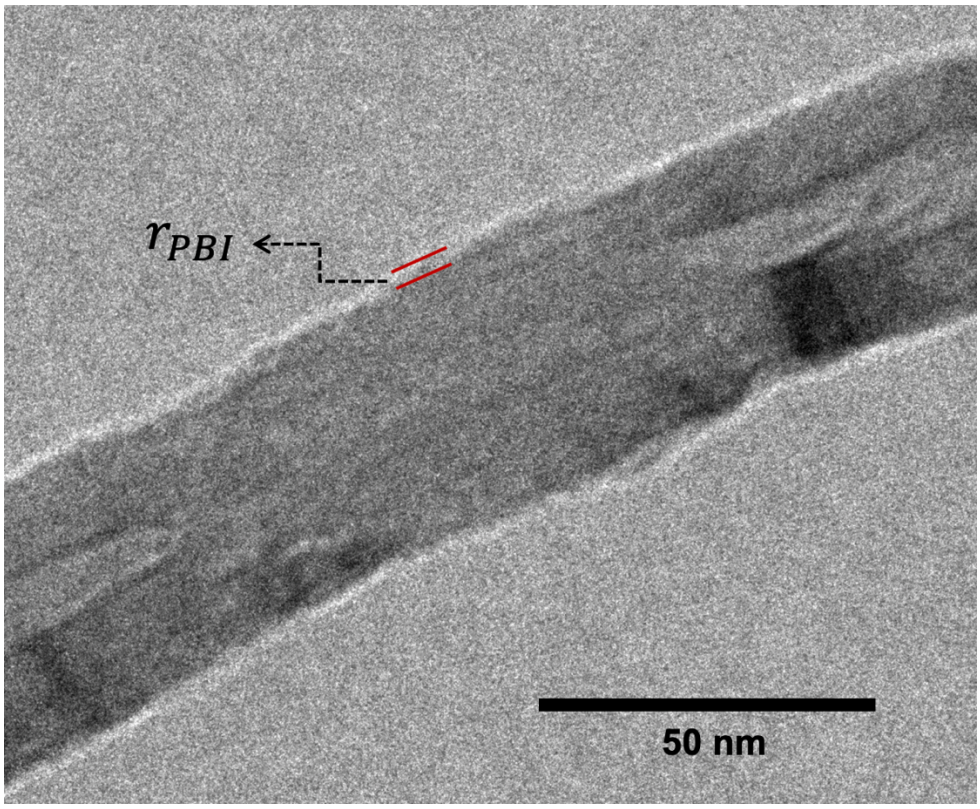

Figure 5.7. TEM image showing thin polybenzimidazole layer over carbon nanotube.

5.2. Cyclic Voltammetry (CV) Measurement

1000 cycle CV performance of Pt-PBI/MWCNT catalyst is shown in Figure 5.8.

$$ECSA\ (m^2 g^{-1}) = \frac{Q_H(\mu C\ cm^{-2})}{210\ (\mu C\ cm^{-2}) x\ Pt\ loading\ (g\ m^{-2})} \quad (5.3)$$

The electrochemically active surface area (ECSA) of the catalyst was calculated using Eq. 5.3 from the charges (Q_H) in the specific H_2 adsorption/desorption regions (-0.2V to 0.1V) assuming a value of 210 $\mu C \cdot cm^{-2}$ for the adsorption of hydrogen monolayer. The maximum ECSA value of Pt-PBI/MWCNT catalyst was calculated as 43.0 $m^2 \cdot g^{-1}$. For the comparison, ECSA of non-PBI, Pt-MWCNT catalyst, which was synthesized without changing any parameter [79] and commercial Pt/C (40% wt. Pt over Vulcan XC-72) catalyst were summarized in Table 5.1.

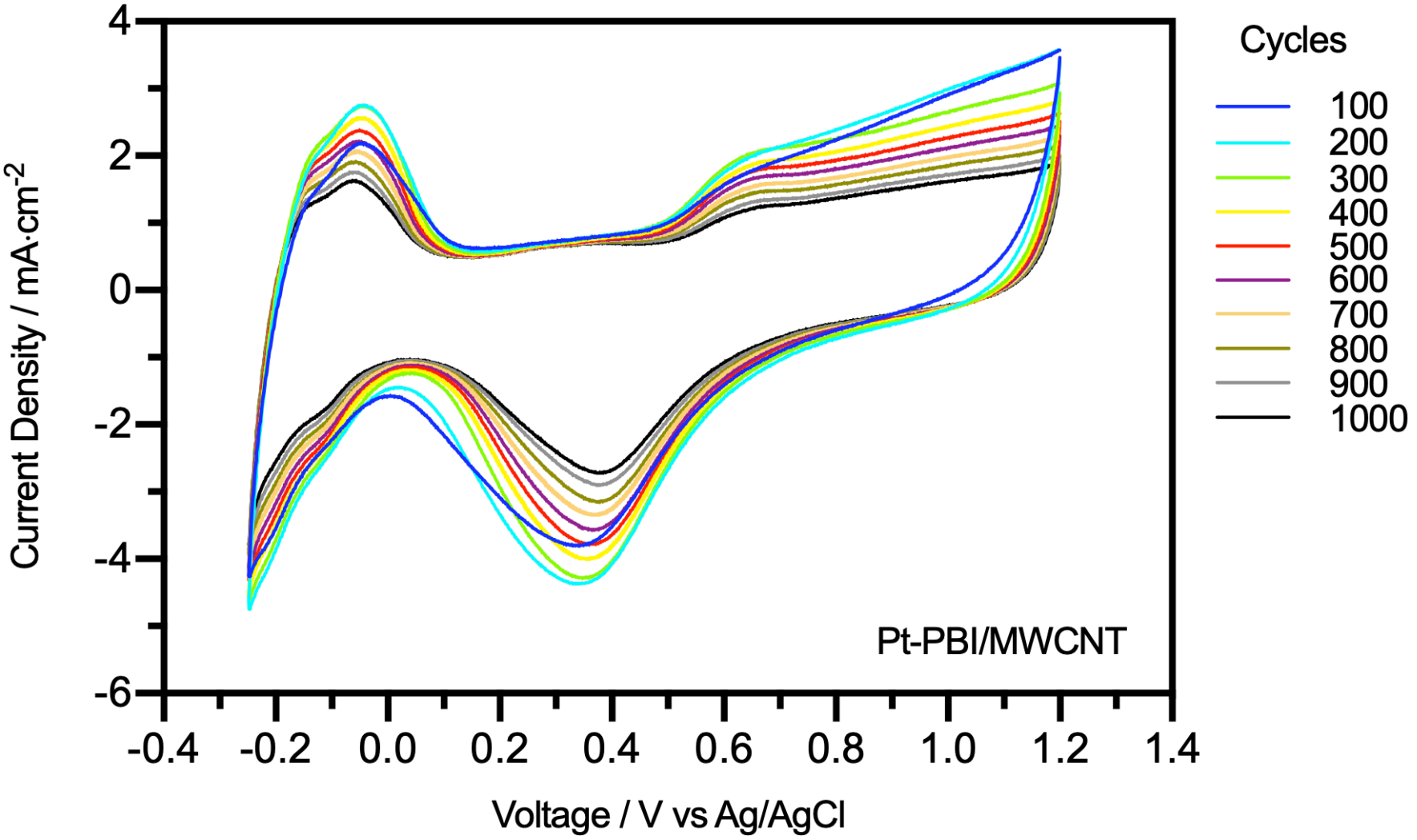

Figure 5.8. 1000 cycles CV performance of Pt-PBI/MWCNT catalyst.

It was shown that such a thin wrapping of PBI enabled a sufficient amount of electronic communication between Pt and MWCNT for fuel cell operations. But, considering the highest ECSA values, Pt-PBI/MWCNT catalyst was similar or slightly less active than that of Pt-MWCNT and commercial Pt/C catalysts (Vulcan XC-72). The reason for that can be attributed to the hydrophobic behavior of PBI film that wrapped over carbon nanotubes, which brings relatively poor contact between Pt-PBI/MWCNT catalyst and $HClO_4$ aqueous electrolyte during the CV analysis. However, due to the Lewis acid-base interactions between H_2PO_3-O-H and PBI imidazole-N groups, the Pt-PBI/MWCNT catalyst is much more compatible with the H_3PO_4 doped PBI membrane [86]. For all ECSA values, the most striking data is the durability performance of a Pt-PBI/MWCNT catalyst after the 1000th cycle. As seen in Figure 5.9 and 5.10, Pt-PBI/MWCNT catalyst preserved almost 80% of its maximum ECSA value. For the comparison, a typical Pt/MWCNT catalyst preserved 66% of its maximum, while commercial Pt/C preserved only 28% of its maximum. The reason for that might be the fine and uniform dispersion of smaller Pt nanoparticles on the polymer film.

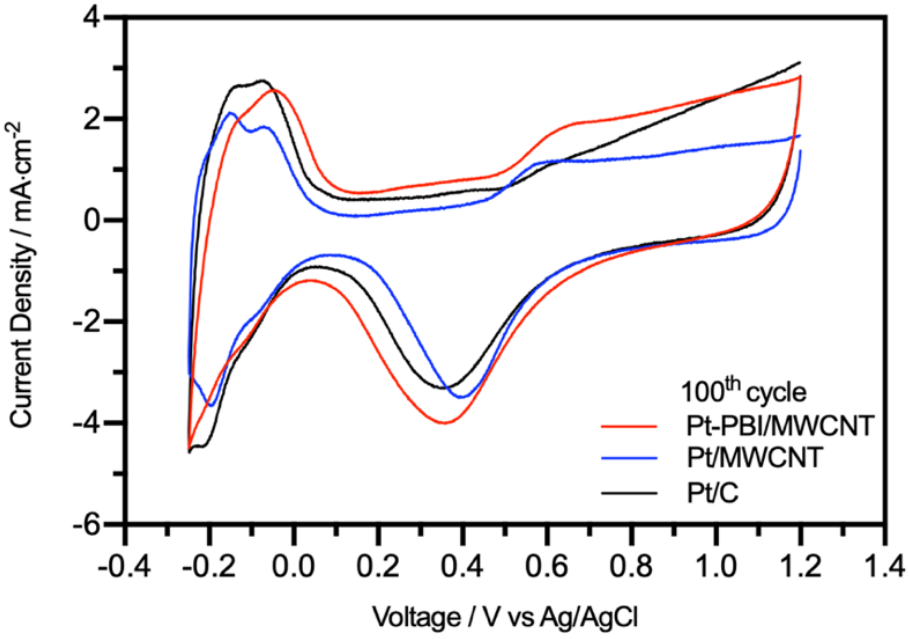

Figure 5.9. 100th cycle of Pt-PBI/MWCNT, Pt/MWCNT, and Pt/C catalysts in CV measurement.

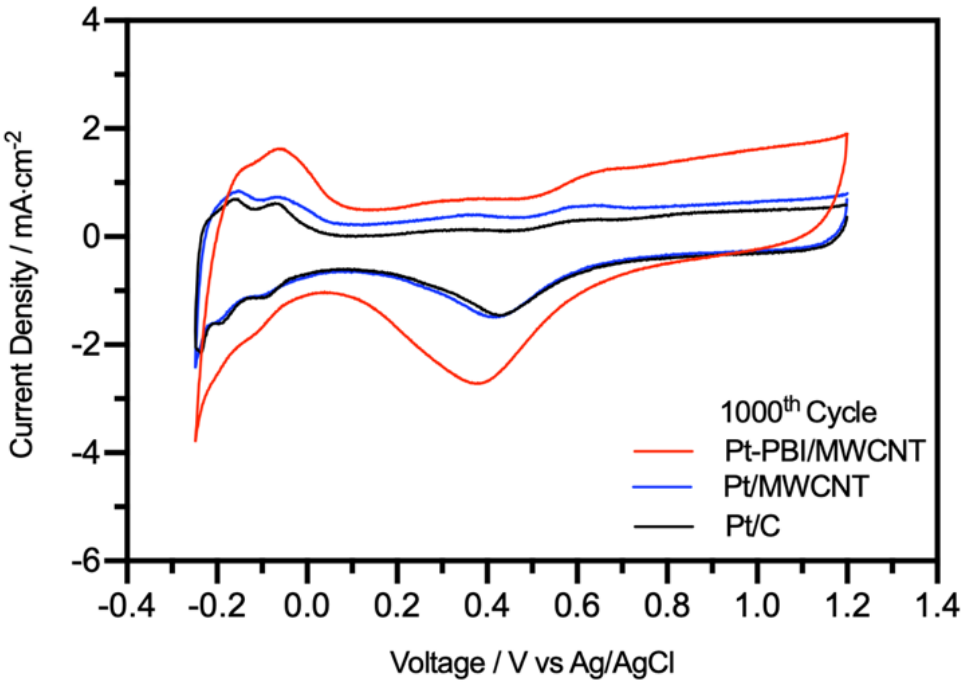

Figure 5.10. 1000th cycle of Pt-PBI/MWCNT, Pt/MWCNT, and Pt/C catalysts in CV measurement.

Table 5.1. *Summary of catalysts in terms of the ECSA and ECSA loss after 1000th CV cycle.*

Catalyst	**Pt (% wt.)**	**ECSA$_{max}$ ($m^2 \cdot g^{-1}$)**	**ECSA loss (%)**	**Loading wt. Pt ($mg \cdot cm^{-2}$)**
Pt-PBI/MWCNT	39	43	21	0.02
Pt/MWCNT	42	48	34	0.02
Pt/C	40	52	78	0.02

These results are also very supportive and parallel to the literature ones that asserted improvement in durability through preparing a support material by wrapping polymer film over carbon nanotubes. However, demonstration of durability under CV analysis could be supported with the long-term evaluations under single-cell tests. This would be examined in future studies, and it will be a significant contribution to the literature.

5.3. Specific Surface Area (SSA) and Pt Utilization Efficiency (η_{Pt})

Another parameter, Pt utilization efficiency (η_{Pt}) is essential for describing catalytic efficiency and it can be calculated by dividing ECSA to SSA (Eq. 5.4, Eq. 5.5, and Eq. 5.6) where ρ_{Pt} is the density of Pt and *d* is the diameter of Pt nanoparticles.

$$SSA_{Pt} = \frac{6000}{\rho_{Pt}\, x\, d} \tag{5.4}$$

$$\eta_{Pt} = \frac{ECSA}{SSA}\, x\, 100 \tag{5.5}$$

$$SSA_{Pt} = \frac{6000}{\rho_{Pt}\, x\, d[3,2]}\text{ , d [3,2]} = \frac{\Sigma n_i\, d_i^3}{\Sigma n_i\, d_i^2} \tag{5.6}$$

SSA provides valuable information about the quality of the catalyst. However, in the literature, there is confusion related to the calculation methods. In order to calculate SSA, using the average crystallite-size obtained from the Scherrer Eq. may be incorrect because nanoparticles generally consist of many grains. Using just the average crystallite size may result in very high SSA (140.6 $m^2 \cdot g^{-1}$) and very low utilization efficiency (30.6%). In this case, considering the Sauter-mean-diameter (d_{32}) would give a more accurate value. Specific surface area (SSA) of platinum nanoparticles was calculated (Eq. 5.6) as 57.1 $m^2 \cdot g^{-1}$ by taking Sauter mean diameter (d_{32}) as 4.9 nm. (See Appendix B for calculations). As seen in Table 5.2, there is a vast gap between estimates for both surface area and the utilization efficiency.

Table 5.2. *Comparison of d_{TEM} vs d_{XRD} and effects on SSA and* η_{Pt}.

Method	d (nm)	SSA_{Pt} ($m^2 \cdot g^{-1}$)	η_{Pt} (%)
d_{XRD}	1.99	140.6	30.6
d_{TEM}	4.90	57.1	75.3

5.4. High-Temperature PEM Fuel Cell Test

The performance of a Pt-PBI/MWCNT based MEA is summarized in Figure 5.11. Comparison of Pt-PBI/MWCNT to the reference MEA (Pt/C for both anode and cathode) is outlined in Table 5.3. OCV of Pt-PBI/MWCNT was found to be around 0.91V, and OCV of the Pt/C was wound to be around 0.94, at all temperatures. Many hypotheses conclude that the OCV difference can be attributed to the hydrogen crossover, resulting in an oxygen reduction reaction overpotential at the cathode. Because crossover current due to oxygen permeation does not affect the anode overpotential [92]. The initial assessment shows that the Pt-PBI/MWCNT catalyst has slightly more parasitic reactions at the cathode site. The highest current and power densities were calculated as 117 $mA \cdot cm^{-2}$ and 47 $mW \cdot cm^{-2}$ at 180°C, respectively. It was observed that the performance of Pt-PBI/MWCNT catalyst was inferior to Pt/C at all temperatures. As pointed out in the literature, the most likely reason for that could be the polymer film over nanotubes might block some of the active areas of platinum nanoparticles. In the cyclic voltammetry, it is found that the electrochemically active surface area of Pt-PBI/MWCNT was slightly lower than that of the commercial Pt/C. On the other hand, the performance of the Pt-PBI/MWCNT catalyst was sharply increased while increasing the temperature due to the increase in proton conductivity of polybenzimidazole film at elevated temperatures. In cyclic voltammetry, the durability of Pt-PBI/MWCNT was excellent. Still, according to single-cell test results, Pt-PBI/MWCNT needs more improvement in performance so it can be used as an electrocatalyst in a typical high-temperature PEMFC application. Detailed polarization curves of Pt/C vs. Pt-PBI/MWCNT at different temperatures are summarized in Figure 5.12 to 5.15.

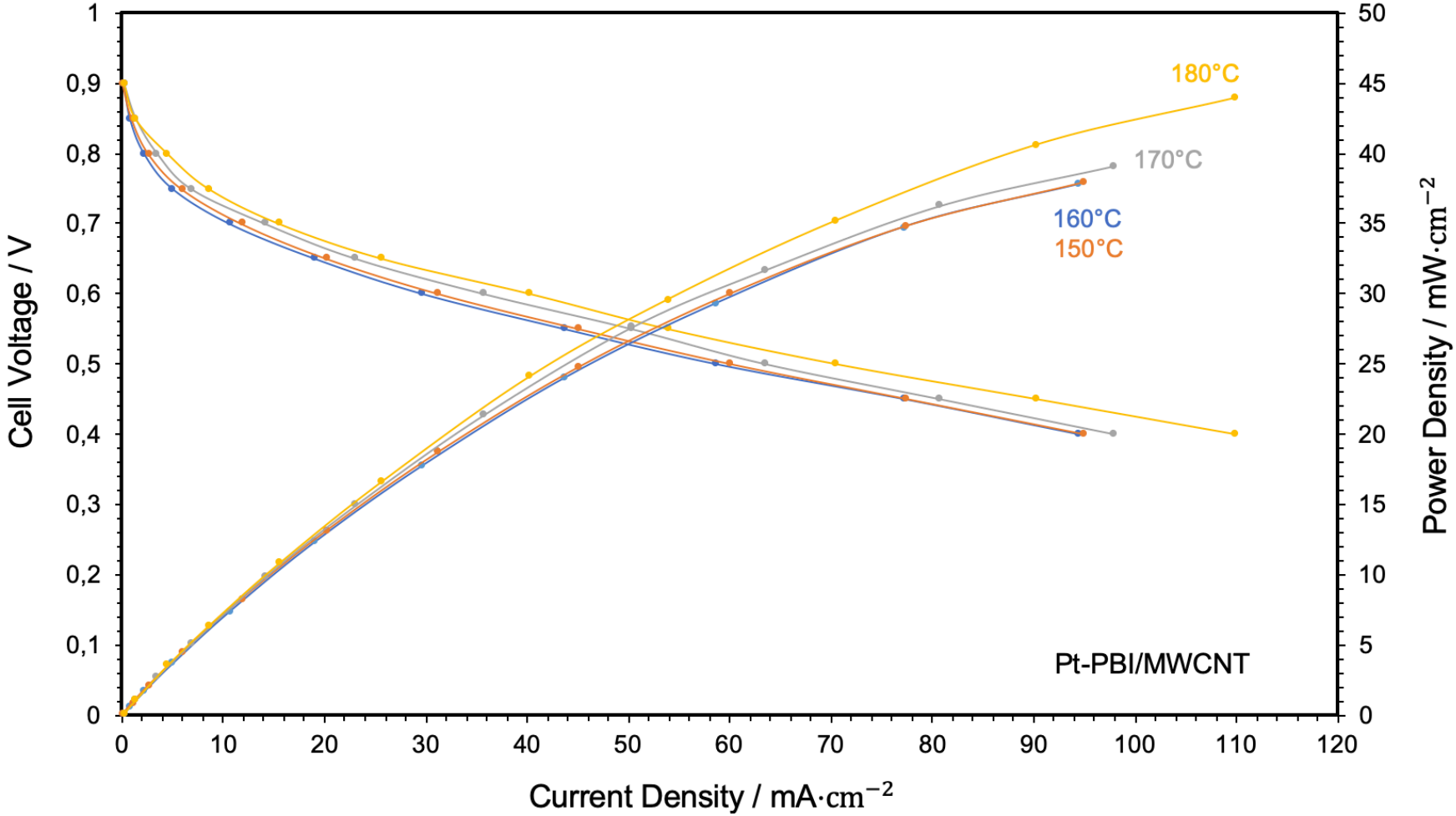

Figure 5.11. HT-PEMFC polarization curves of Pt-PBI/MWCNT catalyst at different temperatures.

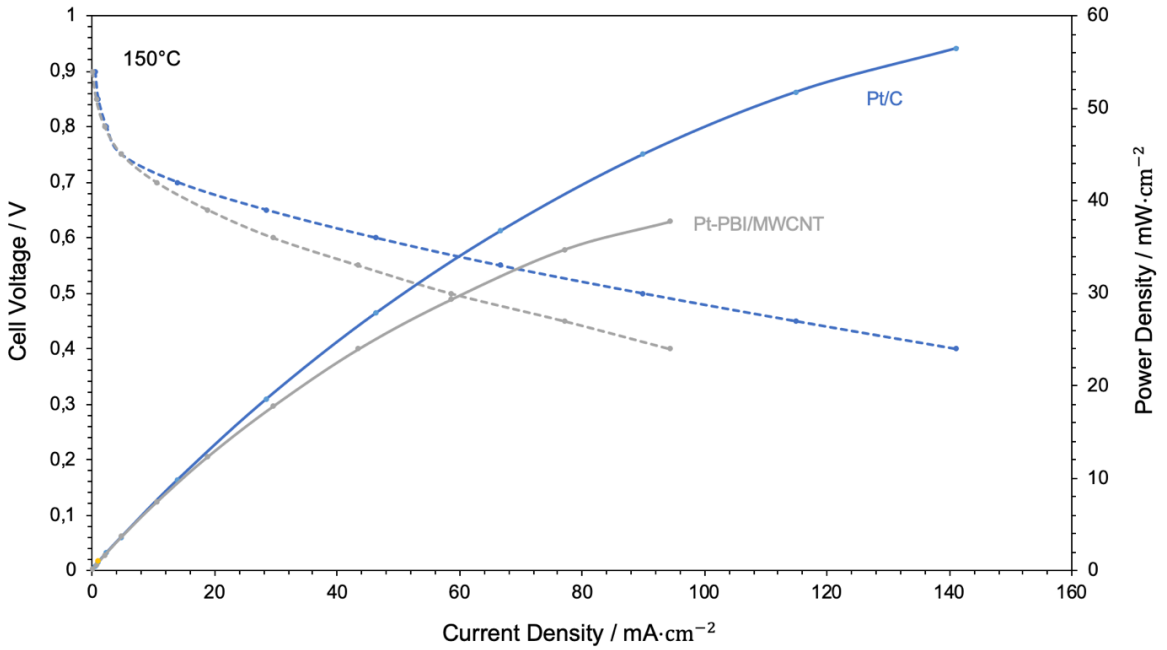

Figure 5.12. Voltage, current & power density curves of Pt-PBI/MWCNT and reference Pt/C at 150 ℃.

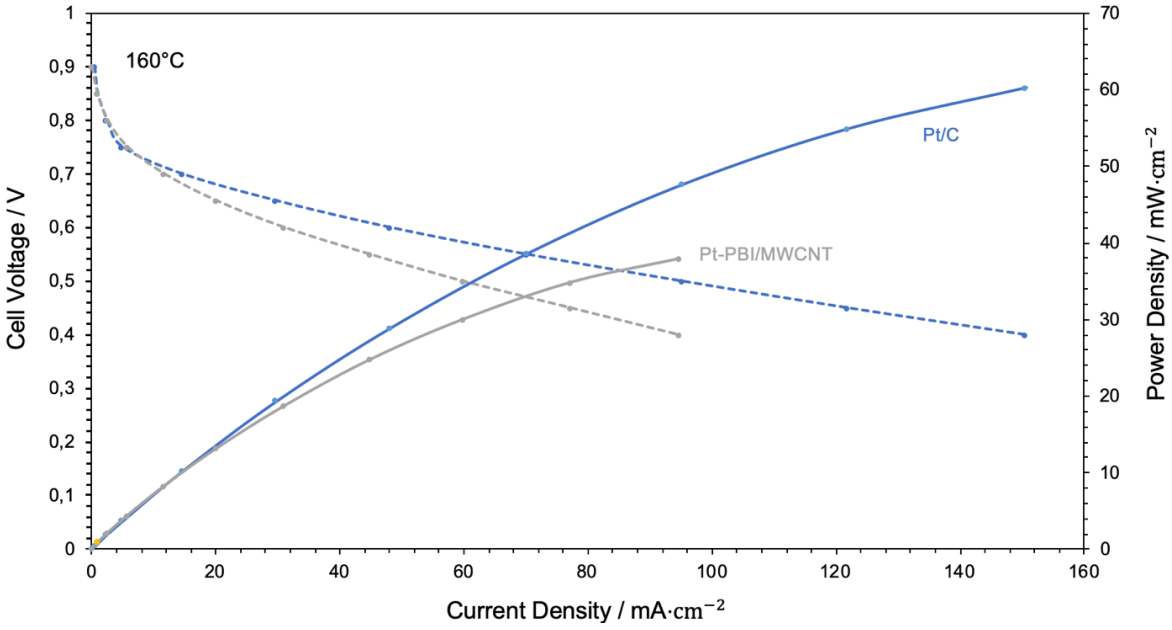

Figure 5.13. Voltage, current & power density curves of Pt-PBI/MWCNT and reference Pt/C at 160 ℃.

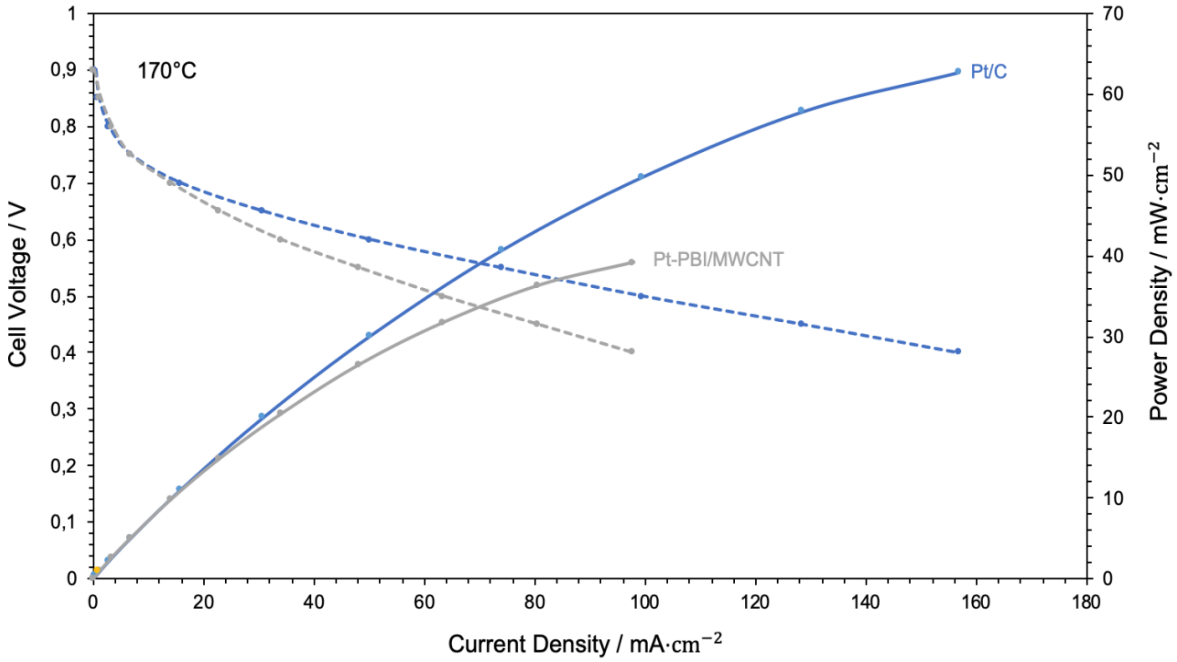

Figure 5.14. Voltage, current & power density curves of Pt-PBI/MWCNT and reference Pt/C at 170 ℃.

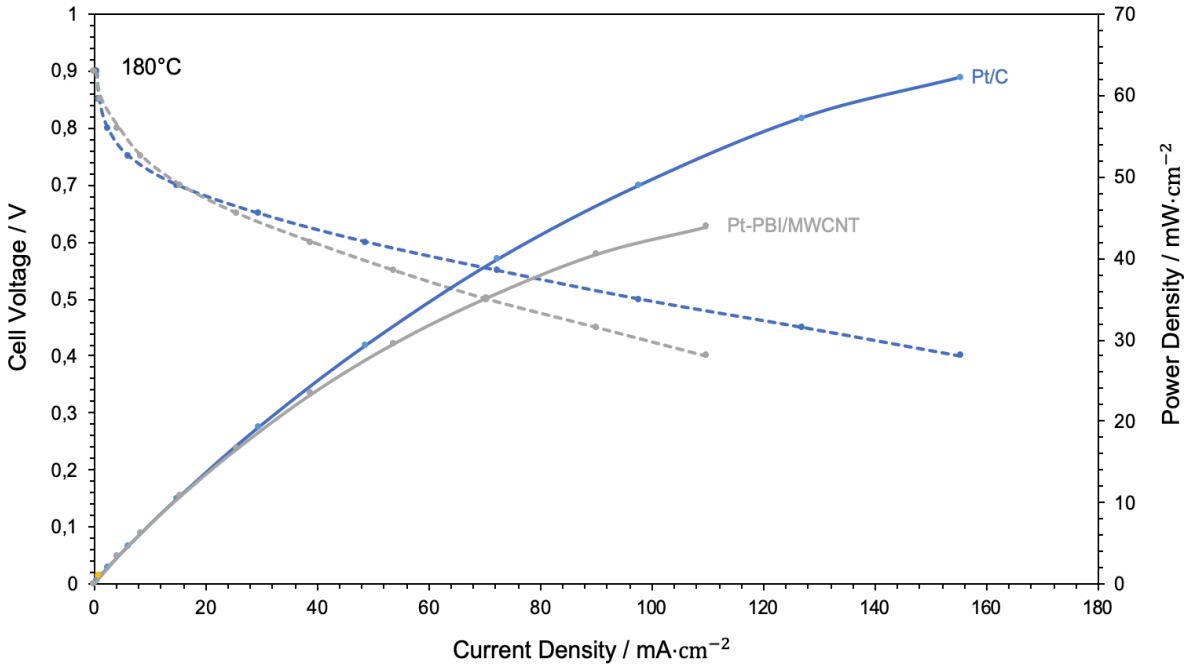

Figure 5.15. Voltage, current & power density curves of Pt-PBI/MWCNT and reference Pt/C at 180 ℃.

Table 5.3. *Summary of single-cell HT-PEMFC performance of Pt-PBI/MWCNT and Pt/C.*

MEA	OCV	P_{max} ($mW \cdot cm^{-2}$)	I_{max} ($mA \cdot cm^{-2}$)	$I_{0.6V}$ ($mA \cdot cm^{-2}$)
Pt-PBI/MWCNT, 150°C	0.91 V	38	94	30
Pt-PBI/MWCNT, 160°C	0.91 V	38	95	31
Pt-PBI/MWCNT, 170°C	0.91 V	40	98	36
Pt-PBI/MWCNT, 180°C	0.91 V	47	117	40
Pt/C, 150°C	0.94 V	57	141	47
Pt/C, 160°C	0.94 V	60	150	48
Pt/C, 170°C	0.94 V	62	156	50
Pt/C, 180°C	0.94 V	62	155	49

CHAPTER 6

CONCLUSIONS AND RECOMMENDATIONS

6.1. Conclusions and Recommendations for Co-N/MWCNT Catalyst

An increase in demand for noble metals is a huge problem considering the commercialization of fuel cell systems. Over the last few decades, efforts on developing cost-efficient catalytic materials have brought the introduction of Me-N-C complexes, especially for the oxygen reduction reaction. In this study, the development of a cobalt-nitrogen-carbon catalyst for high-temperature PEM fuel cell cathode was the primary goal. After the comprehensive literature review, the synthesis of non-noble Co-N/MWCNT electrocatalyst was achieved through the high-temperature pyrolysis method. According to the literature, the generation of cobalt-based electrocatalytic centers could be achieved through the one-hour heat treatment at 700°C under inert gas. Due to the infancy of the subject, extensive characterization is fundamental because, unlike the noble electrocatalyst, the performance of such electrocatalysts strongly depends on the physico-chemical states of the structures. Co-N/MWCNT powder was characterized by the five-step chemical/morphological analysis. Thanks to the high-resolution analytical surface characterization methods, XPS & ToF-SIMS, the presence of CoN/CoNC complexes was easily determined. Furthermore, deconvoluted triplet peaks proved that the formation of the pyridinic-N structure was favorable, which is strictly essential for desired oxygen reduction performance. From Raman spectra, high distortions along the open edges of graphite would also provide more active sites for the formation of catalytic complexes. The crystallization degree of the nanoparticles was investigated by XRD, and the average crystallite size was calculated as 6.23 nm. Finally, from the HR-TEM images, distributions of nanoparticles along nanotubes were found fine and uniform. The oxygen reduction performance of the catalyst was evaluated through the rotating disc

electrode (RDE) method. From the Koutecky-Levich plots, a maximum number of transferred-electron (n) and diffusion-limiting current density values were calculated as 3.95 and 4.53 $mA \cdot cm^{-2}$, respectively, which means that the reaction mainly occurs through the $4e^-$ pathway with a quite potent limiting factor. For the comparison, Co-N/MWCNT and commercial Pt/C also had very close E_{onset} and $E_{1/2}$. ORR performance of a non-noble catalyst was auspicious and further evaluated under the real-time single-cell PEM fuel cell test station. From the HT-PEMFC test results, current and power densities of Co-N/MWCNT was superior to that of commercial Pt/C at the 150°C and 160°C. Also, OCV values suggest that the less parasitic reactions take place at the cathode side. However, the performance of the Co-N/MWCNT catalyst was slightly decreased while increasing the temperature due to the stability issue of $Co\text{-}N_4$ sites at elevated temperatures. At the 170°C, Co-N/MWCNT and Pt/C have identical performance. At the 180°C, Co-N/MWCNT has lost 25% of its initial performance and became inferior to Pt/C. This lab-scale study verified that the Co-N/MWCNT electrocatalyst could be the promising alternative to the noble Pt/C catalyst at the cathode site, especially for the lower boundary of high-temperature PEMFC applications.

6.2. Conclusions and Recommendations for Pt-PBI/MWCNT Catalyst

Due to the higher operating temperatures and acidic environments, traditional platinum-based electrocatalysts may quickly degrade in high-temperature PEM fuel cell applications. According to the literature, increasing their durability can be achieved by wrapping carbon nanotubes with a polybenzimidazole (PBI) film. Due to the attraction between them, the polymer can easily coat the carbon nanotubes in a specific solvent. In this study, the preparation of PBI/MWCNT support material and microwave-assisted polyol reduction of platinum nanoparticles were examined. As-synthesized catalyst powder was characterized through the TGA, XPS, XRD, and TEM analysis. From the TGA, the amount of Pt nanoparticles in the composite was calculated as ~39 wt%, which means that ~98% of fed-Pt was loaded onto the surface of PBI/MWCNT support material. From the XPS, spin orbital-splitting of Pt 4f region gave double peaks, meaning that the platinum nanoparticles were reduced

appropriately by having zero valence electrons. The presence of a PBI in the catalyst was verified by the core level of the N 1s region from the XPS. The crystallization degree of nanoparticles was further investigated by XRD, and the average crystallite size was calculated as 1.99 nm. From the TEM images, the thin layer of polybenzimidazole film was shown over the carbon nanotubes, and the average platinum particle diameter was calculated as 4.90 nm. They enable smooth transportations of electrolytes while preventing unwanted agglomeration of active sites to enhance electrocatalytic properties. The electrochemical performance of the Pt-PBI/MWCNT catalyst was examined through the cyclic voltammetry (CV) analysis. The electrochemically active surface area (ECSA) of the catalyst was calculated as 43.0 $m^2 \cdot g^{-1}$. Such a thin wrapping of PBI enabled a sufficient amount of electronic communication between Pt and MWCNT for fuel cell operations. However, comparing it with the Pt-MWCNT and commercial Pt/C, ECSA of Pt-PBI/MWCNT was slightly lower due to the hydrophobic behavior of polybenzimidazole. But, the most striking data is the durability performance of a Pt-PBI/MWCNT catalyst after the 1000^{th} cycle. Pt-PBI/MWCNT catalyst preserved almost 80% of its initial ECSA. For the comparison, a typical Pt/MWCNT catalyst preserved 66% of its initial ECSA, while commercial Pt/C preserved only 28% of its initial ECSA, which makes the Pt-PBI/MWCNT is much more durable than the commercial Pt/C and Pt/MWCNT. The CV analysis concludes that the PBI-wrapped MWCNTs as a support material can somehow improve the durability of noble catalysts in a typical hydrogen oxidation demonstration. From the HT-PEMFC results, current and power densities of Pt-PBI/MWCNT were inferior to the Pt/C at all temperatures. The reason for that could be the polymer film over nanotubes might block some of the active areas of platinum nanoparticles. Increasing the durability by preparing a PBI/MWCNT support brought the reduction in electrochemical performance, which was nowhere near compared with the current commercial Pt/C catalysts. So, decreasing the amount of polybenzimidazole in the catalyst may bring the balance between durability and performance. Considering this study, such a catalyst is not fully efficient to serve in high-temperature PEM fuel cells. Unlike the commercial Pt/C, due to the increase in conductivity of PBI at elevated temperatures, it is observed that the peak power

density value of Pt-PBI/MWCNT is slightly increased from 38 $mW \cdot cm^{-2}$ to 47 $mW \cdot cm^{-2}$ while increasing the temperature towards 180°C, meaning that the Pt-PBI/MWCNT could be the better candidate at even higher operating temperatures. In the literature, reported maximum power density values of Pt-PBI/CNT catalysts are superabundant and found to be as high as 300-400 $mW \cdot cm^{-2}$ at 0.4 V because, in that studies, pure O_2 is used as an oxidant rather than conventional dry air which is the supercritical parameter to increase cell performance. The study concludes that the PBI-wrapped MWCNTs as a support material can somehow improve the durability of noble catalysts in a typical hydrogen oxidation demonstration. However, demonstration of durability under CV analysis could be supported with the long-term evaluations under single-cell tests. This would be considered in future studies.

REFERENCES

[1] Dicks, A., & Larmine, J. *Fuel Cell Systems Explained*. *Chapter 1 Introduction, pp.3*. John Wiley & Sons Ltd, England. 2003.

[2] Grove, W.R., On voltaic series and the combination of gases by platinum, *Philosophical Magazine and Journal of Science*, Series 3, 14, 127–130, 1839.

[3] Baur, E. and Preis, H., Über Brennstoff-ketten mit Festleitern, *Zeitschrift für Elektrochemie*, 43, 727–732, 1937.

[4] Broers, G.H.J. and Ketelaar, J.A.A., *High-temperature fuel cells,* Young, G.J., Ed., Reinhold Publishing Corporation, New York, 1960a, pp. 78–93.

[5] H. Gregor & Chen E. *Fuel Cell Technology Handbook*. *Chapter 2.1: History*, CRC Press, New York, 2003.

[6] Behling N. H., *Chapter 2 - Fuel Cells and the Challenges Ahead, Fuel Cells*, Elsevier, 2013, Pages 7-36, ISBN 9780444563255.

[7] Hilmi, Abdelkader & Yuh, Chao-Yi & Farooque, Md. (2009). *Fuel Cells – Molten Carbonate Fuel Cells | Anodes. Encyclopedia of Electrochemical Power Sources*, pp.454-461.

[8] Dicks, A., & Larmine, J. *Fuel Cell Systems Explained*. *Chapter 7 Solid Oxide Fuel Cells, pp.214*. John Wiley & Sons Ltd, England. 2003. ISBN: 0-470-84857-X

[9] Dicks, A., & Larmine, J. *Fuel Cell Systems Explained*. *Chapter 4 Proton Exchange Membrane Fuel Cells, pp.67*. John Wiley & Sons Ltd, England. 2003. ISBN: 0-470-84857-X

[10] H. Gregor & Chen E. *Fuel Cell Technology Handbook*. *Chapter 4: Fuel Cell Components and Their Impact on Performance*, CRC Press, New York, 2003.

[11] Cooper, K. R., & Smith, M. (2006). *Electrical test methods for on-line fuel cell ohmic resistance measurement*, *160*(February), 1088–1095.

[12] Abdi, H., Nezhad, R. R., & Salehimaleh, M. (2017). *Chapter 5, Fuel Cells*. *Distributed Generation Systems*. Elsevier Inc.

[13] Fox, E. B., & Colón-mercado, H. R. (2011). *Mass Transfer – Advanced Aspects, Chapter 13*, *Mass Transport Limitations in Proton Exchange Membrane Fuel Cells and Electrolyzers*, InTech, ISBN: 978-953-307-636-2.

[14] H. Gregor & Chen E. *Fuel Cell Technology Handbook*. *Chapter 4.3.1.1: Fuel Cell Components and Their Impact on Performance - Per Fluorinated Membranes,* CRC Press, New York, 2003.

[15] H. Gregor & Chen E. *Fuel Cell Technology Handbook*. *Chapter 4.3.1.3: Fuel Cell Components and Their Impact on Performance – High Performance/Lower Humidification,* CRC Press, New York, 2003.

[16] H. Gregor & Chen E. *Fuel Cell Technology Handbook*. *Chapter 4.3.2: Fuel Cell Components and Their Impact on Performance – Fuel Cell Electrodes and Gas Diffusion Layers,* CRC Press, New York, 2003.

[17] Antonlini, E. (1999) *Influence of nafion loading in the catalyst layer of gas diffusion electrodes for PEFC*, J. Power Sources, 77, 3.

[18] H. Gregor & Chen E. *Fuel Cell Technology Handbook*. *Chapter 4.4.1: Fuel Cell Components and Their Impact on Performance – Bipolar Plates,* CRC Press, New York, 2003.

[19] H. Gregor & Chen E. *Fuel Cell Technology Handbook*. *Chapter 4.4.2: Fuel Cell Components and Their Impact on Performance – Humidifiers and Cooling Plates,* CRC Press, New York, 2003.

[20] Strasser, K. (Siemens AG), *German Patent DE4,201,632,* 1993.

[21] Rosli, R. E., Sulong, A. B., Daud, W. R. W., & Zulkifley, M. A. (2016). *A review of high-temperature proton exchange membrane fuel cell (HT-PEMFC) system.* International Journal of Hydrogen Energy, 1–22.

[22] Chandan, A., Hattenberger, M., El-kharouf, A., Du, S., Dhir, A., Self, V., Bujalski, W. (2013). *High temperature (HT) polymer electrolyte membrane fuel cells (PEMFC) A review.* Journal of Power Sources, *231*, 264–278.

[23] H. Gregor & Chen E. *Fuel Cell Technology Handbook*. *Chapter 6.6: Catalysts for the Proton Exchange Membrane Fuel Cell – Cathode Electrocatalysts,* CRC Press, New York, 2003.

[24] Wang, J., Wang, H., & Fan, Y. (2018). *Techno-Economic Challenges of Fuel Cell Commercialization.* Engineering, *4*(3), 352–360.

[25] Yan, X., Yao, Y., & Chen, Y. (2018). *Highly Active and Stable Fe-N-C Oxygen Reduction Electrocatalysts Derived from Electrospinning and In Situ Pyrolysis*. Nanoscale Research Letters, *13*, 0–6.

[26] Huang, Y. P., Yuan, H. Y., Zhang, J, (2017). *Preparation and Properties of Tremella-like Fe-N-C Composite Catalyst for Oxygen Reduction Reaction*. Chinese Journal of Analytical Chemistry, *45*(9), 1297–1302.

[27] Kattel, S., & Wang, G. (2013). *A density functional theory study of oxygen reduction reaction on Me-N 4 (Me = Fe, Co, or Ni) clusters between graphitic pores*. Journal of Materials Chemistry, *1*(36), 10790–10797.

[28] Sun, M., Davenport, D., Liu, H., Qu, J., Elimelech, M., & Li, J. (2018). *Highly efficient and sustainable non-precious-metal Fe-N-C electrocatalysts for the oxygen reduction reaction*. Journal of Materials Chemistry, *6*(6), 2527–2539.

[29] Chung, M. W., & Choi, C. H. (2017). *Carbon nanofibers as parent materials for a graphene-based Fe-N-C catalyst for the oxygen reduction reaction*. Catalysis Today, *295*(April), 125–131.

[30] Kattel, S., & Wang, G. (2014). *Reaction Pathway for Oxygen Reduction on FeN4 Embedded Graphene*. The Journal of Physical Chemistry Letters, *5*(3), 452–456.

[31] Liang, W., Chen, J., Liu, Y., & Chen, S. (2014). *Density-Functional-Theory Calculation Analysis of Active Sites for Four-Electron Reduction of O_2 on Fe/N-Doped Graphene*. ACS Catalysis, *4*(11), 4170–4177.

[32] Gao, F., Zhao, G. L., Wang, Z., Bagayoko, D., & Liu, D. J. (2015). *Catalytic reaction on FeN4/C site of nitrogen functionalized carbon nanotubes as cathode catalyst for hydrogen fuel cells*. Catalysis Communications, *62*, 79–82.

[33] Titov, A., Zapol, P., Kral, P., Liu, D. J., Iddir, H., Baishya, K., & Curtiss, L. A. (2009). *Catalytic Fe-xN sites in carbon nanotubes*. Journal of Physical Chemistry C, *113*(52), 21629–21634.

[34] Kattel, S., & Wang, G. (2013). *A density functional theory study of oxygen reduction reaction on Me-N 4 (Me = Fe, Co, or Ni) clusters between graphitic pores.* Journal of Materials Chemistry A, *1*(36), 10790–10797.

[35] Tran, P. D., Morozan, A., Archambault, S., Heidkamp, J., Chenevier, P., Dau, H., … Artero, V. (2015). *A noble metal-free proton-exchange membrane fuel cell based on bio-inspired molecular catalysts*. Chemical Science, *6*(3), 2050–2053.

[36] Sa, Y. J., Kim, J. H., & Joo, S. H. (2017). *Recent Progress in the Identification of Active Sites in Pyrolyzed Fe-N/C Catalysts and Insights into Their Role in Oxygen Reduction Reaction.* Journal of Electrochemical Science and Technology, *8*(3), 169–182.

[37] Glibin, V. P., & Dodelet, J.-P. (2017). *Thermodynamic Stability in Acid Media of FeN_4 -Based Catalytic Sites Used for the Reaction of Oxygen Reduction in PEM Fuel Cells*. Journal of The Electrochemical Society, *164*(9), F948–F957.

[38] Lo Vecchio, C., Aricò, A. S., Monforte, G., & Baglio, V. (2018). *EDTA-derived Co–N–C and Fe–N–C electro-catalysts for the oxygen reduction reaction in acid environment*. Renewable Energy, *120*, 342–349.

[39] Bezerra, C. W. B., Zhang, L., Lee, K., Liu, H., Marques, A. L. B., Marques, E. P., … Zhang, J. (2008). *A review of Fe-N/C and Co-N/C catalysts for the oxygen reduction reaction*. Electrochimica Acta, *53*(15), 4937–4951.

[40] Lefèvre, M., Proietti, E., Jaouen, F., & Dodelet, J. P. (2009). *Iron-Based catalysts with improved oxygen reduction activity in polymer electrolyte fuel cells*. Science, *324*(5923), 71–74.

[41] Hossen M., Artyushkova K., Atanassov P. (2017). *Synthesis and characterization of high performing Fe-N-C catalyst for oxygen reduction reaction (ORR) in Alkaline Exchange Membrane Fuel Cells*. Journal of Power Sources 2017, 1-8.

[42] Zhao, X., Zhou, Y., Jin, A., Huang, K., Liu, F., & Tao, D. (2018). *Co-N-C catalysts synthesized by pyrolysis of Co-based deep eutectic solvents for aerobic oxidation of alcohols*, Royal Society of Chemistry, 15871–15878.

[43] Byeon, A., Lee, K. J., Lee, M. J., Lee, J. S., Lee, I. H., Park, H. Y., … Kim, J. Y. (2018). *Effect of Catalyst Pore Size on the Performance of Non-Precious Fe/N/C-Based Electrocatalysts for High-Temperature Polymer Electrolyte Membrane Fuel Cells*. ChemElectroChem, *5*(14), 1805–1810.

[44] Xiao, M., Zhu, J., Ma, L., Jin, Z., Ge, J., Deng, X., … Xing, W. (2018). *Microporous Framework Induced Synthesis of Single-Atom Dispersed Fe-N-C Acidic ORR Catalyst and Its in Situ Reduced Fe-N4Active Site Identification Revealed by X-ray Absorption Spectroscopy*. ACS Catalysis, *8*(4), 2824–2832.

[45] Zhao, D., Shui, J. L., Chen, C., Chen, X., Reprogle, B. M., Wang, D., & Liu, D. J. (2012). *Iron imidazolate framework as precursor for electrocatalysts in polymer electrolyte membrane fuel cells*. Chemical Science, *3*(11), 3200–3205.

[46] Yang, J., Liu, D. J., Kariuki, N. N., & Chen, L. X. (2008). *Aligned carbon nanotubes with built-in FeN4 active sites for electrocatalytic reduction of oxygen*. Chemical Communications, *3*(3), 329–331.

[47] Liu, Q., Liu, X., Zheng, L., & Shui, J. (2018). *The Solid-Phase Synthesis of an Fe-N-C Electrocatalyst for High-Power Proton-Exchange Membrane Fuel Cells,* Angewandte, *100049*(19), 1204–1208.

[48] Du, J., Cheng, F., Wang, S., Zhang, T., & Chen, J. (2014). *M(Salen)-derived nitrogen-doped M/C (M = Fe, Co, Ni) porous nanocomposites for electrocatalytic oxygen reduction*. Scientific Reports, *4*, 1–7.

[49] Du, H., Wang, C., Yang, C., & Hsu, H. (2014). *A high performance Polybenzimidazole – CNT hybrid electrode for high-temperature proton exchange membrane fuel cells,* Journal of Materials Chemistry A, 7015–7019.

[50] Jourdani, M., Mounir, H., & Marjani, A. El. (2017). *Latest Trends and Challenges in Proton Exchange Membrane Fuel Cell (PEMFC).* The Open Fuels & Energy Science Journal, *10*(1), 96–105.

[51] Kaewsai, D., Lin, H. L., & Yu, T. L. (2015). *Influence of Pyridine-Polybenzimidazole Film Thickness of Carbon Nanotube Supported Platinum on Fuel Cell Applications*, Fuel Cells (2), 361–374.

[52] Okamoto, M., Fujigaya, T., & Nakashima, N. (2009). *Design of an Assembly of Poly (benzimidazole), Carbon Nanotubes, and Pt Nanoparticles for a Fuel-Cell Electrocatalyst with an Ideal Interfacial Nanostructure*, Small Journals 5, (6) 735–740.

[53] Fujigaya, T., & Nakashima, N. (2013). *Fuel Cell Electrocatalyst Using Polybenzimidazole-Modified Carbon Nanotubes as Support Materials*, Materials Views, 1666–1681.

[54] Du, H., Yang, C., Hsu, H., Huang, H., Chang, S., Wang, C., … Chen, L. (2015). *ScienceDirect Pulsed electrochemical deposition of Pt NPs on polybenzimidazole-CNT hybrid electrode for high- temperature proton exchange membrane fuel cells*. International Journal of Hydrogen Energy, 1–7.

[55] M., Fujigaya, T., Hirata S., Nakashima, N. (2014). *A highly durable fuel cell electrocatalyst based on polybenzimidazole-coated stacked graphene*, Journal of Materials Chemistry A, 3888–3893.

[56] Zhang, L., Ni, Q., Shiga, A., Natsuki, T., & Fu, Y. (2011). *Preparation of Polybenzimidazole / Functionalized Carbon Nanotube Nanocomposite Films for use as Protective Coatings*, Polymer Engineering and Science, 1525-2532.

[57] Guo, Y., Li, J., Yuan, Y., Li, L., Zhang, M., Zhou, C., & Lin, Z. (2016). *A Rapid Microwave-Assisted Thermolysis Route to Highly Crystalline Carbon Nitrides for Efficient Hydrogen Generation*. Angewandte Chemie - International Edition, *55*(47), 14693–14697.

[58] Martins, L. M. D. R. S., Ribeiro, A. P. C., Carabineiro, S. A. C., Figueiredo, J. L., & Pombeiro, A. J. L. (2016). *Highly efficient and reusable CNT supported iron(ii) catalyst for microwave-assisted alcohol oxidation*. Dalton Transactions, *45*(16), 6816–6819.

[59] Lebègue, E., Baranton, S., & Coutanceau, C. (2011). *Polyol synthesis of nanosized Pt / C electrocatalysts assisted by pulse microwave activation*, Journal of Power Sources *196*, 920–927.

[60] Harish, S., Baranton, S., Coutanceau, C., & Joseph, J. (2012). *Microwave-assisted polyol method for the preparation of Pt/C, Ru/C and PtRu/C nanoparticles and its application in electrooxidation of methanol*. Journal of Power Sources, *214*, 33–39.

[61] Wang, H., Dong, R., Chang, H., & Liu, C. (2007). *Preparation and catalytic activity of Pt/C materials via microwave irradiation*, Materials Letter, *61*, 830–833.

[62] Zhang, W., Chen, J., Swiegers, G. F., Ma, Z., & Wallace, G. G. (2010). *Microwave-assisted synthesis of Pt/CNT nanocomposite electrocatalysts for PEM fuel cells*, Nanoscale, 282–286.

[63] Wu G., More K., Johnston C., Zelenay P (2011). *High-performance electrocatalysts for oxygen reduction derived from polyaniline, iron, and cobalt.* Science, 332:443.

[64] Michel L., Eric P., Frédéric J., Jean-Pol D. (2009). *Iron-based catalysts with improved oxygen reduction activity in polymer electrolyte fuel cells*. Science, 324:71.

[65] Zhao Y., Watanabe K., Hashimoto K. (2012). *Self-supporting oxygen reduction electrocatalysts made from a nitrogen-rich network polymer.* Journal of Chemistry Society, 134:19528.

[66] Li Y., Zhou W., Wang H., Xie L., Liang Y., Wei F., Idrobo J., Pennycook S., Dai HJ. (2012). *An oxygen reduction electrocatalyst based on carbon nanotube– graphene complexes*. Nature Nanotechnology, 7:394.

[67] Ferrero G., Preuss K., Marinovic A., Jorge A., Mansor N., Brett D., Fuertes A., Sevilla M., Titirici M. (2016). *Fe–N-doped carbon capsules with outstanding electrochemical performance and stability for the oxygen reduction reaction in both acid and alkaline conditions*. ACS Nano, 10:5922–5932.

[68] Lin L., Zhu Q., Xu A. (2014). *Noble-metal-free Fe–N/C catalyst for highly efficient oxygen reduction reaction under both alkaline and acidic conditions.* Journal of Chemistry Society, 136:11027.

[69] Liang H., Wei W., Wu Z., Feng X., Millen K. (2013). *Mesoporous metal–nitrogen- doped carbon electrocatalysts for highly efficient oxygen reduction reaction*. Journal of Chemistry Society, 135:16002.

[70] [Kramm U., Herranz J., Larouche N., Arruda TM., Lefevre M., Jaouen F., Bogdanoff P., Fiechter S., Abs-Wurmbach I., Mukerjee S., Dodelet JP (2012). *Structure of the catalytic sites in Fe/N/C-catalysts for O2-reduction in PEM fuel cells*. Phys Chem, 14:11673–11688.

[71] Gong K., Du F., Xia Z., Durstock M., Dai L. (2009). *Nitrogen-doped carbon nanotube arrays with high electrocatalytic activity for oxygen reduction*. Science 323:760.

[72] Han M., Zhang G., Liu Z., Wang S., Li M., Zhu J. (2011). *Cross-linked polybenzimidazole with enhanced stability for high temperature proton exchange membrane fuel cells*. Journal of Materials Chemistry; 21:2187.

[73] Wang JT, Savinell RF, Wainright J, Litt M, Yu H. (1996). *H2/O2 fuel cell using acid doped polybenzimidazole as polymer electrolyte*. Electrochimica Acta 1996; 41:193.

[74] Yuan W., Lu S., Xiang Y., Jiang S. (2014). *Pt-based nanoparticles on non-covalent functionalized carbon nanotubes as effective electrocatalysts for proton exchange membrane fuel cells*. RSC Adv, 4:4626.

[75] Kannan R., Kagalwala H., Chaudhari H., Kharul U., Kurungot S., Pillai VK. (2011) *Improved performance of phosphonated carbon nanotube-polybenzimidazole composite membranes in proton exchange membrane fuel cells*. Journal of Materials Chemistry, 21:7223.

[76] Mote, V. D., Purushotham, Y., & Dole, B. N. (2012). *Williamson-Hall analysis in estimation of lattice strain in nanometer-sized ZnO particles*. Journal of Theoretical and Applied Physics, 6(1), 6.

[77] Speakman S. A. *Estimating Crystallite Size Using XRD*. MIT Center for Materials Science and Engineering, MIT USA.

[78] Klug H., Alexander L. X-Ray *Diffraction Procedures for Polycrystalline and Amorphous Materials 2nd edition – Chapter 9: Crystallite Size and Lattice Strains from Line Broadening*. John Wiley & Sons, 1974.

[79] Devrim Y., & Arica E. D., (2019). *Multi-walled carbon nanotubes decorated by platinum catalyst for high temperature PEM fuel cell*. International Journal of Hydrogen Energy, *44*(34), 18951–18966.

[80] Science, M. (2008). *Fundamentals of Rotating Disc and Ring – Disc Electrode Techniques and their Applications to Study of the Oxygen Reduction Mechanism at Pt / C Electrode for Fuel Cells*. Israel Journal of Chemistry, *48*, 215–228.

[81] Du, C., Tan, Q., Yin, G., & Zhang, J. (2014). *Chapter 5 - Rotating Disk Electrode Method*. *Rotating Electrode Methods and Oxygen Reduction Electrocatalysts*. Elsevier B.V

[82] Wang, H. J., Ishihara, S., Ariga, K. & Yamauchi Y., (2012). *All-metal layer-by-layer films: bimetallic alternative layers with accessible mesopores for enhanced electrocatalysis*. J. Am. Chem. Soc. 134, 10819–10821.

[83] Ocampo, A. L., Castellanos, R. H., & Sebastian, P. J. (2002). *Kinetic Study of the Oxygen Reduction Reaction on Ruy (CO)n in Acid Medium with Different Concentrations of Methanol*. Journal of New Materials for Electrochemical Systems. *168*, 163–168.

[84] Itoe, R. N., Wesson, G. D., & Kalu, E. E. (2000). *Evaluation of Oxygen Transport Parameters in H 2 SO 4 -CH 3 OH Mixtures Using Electrochemical Methods*. Journal of the Electrochemical Society. *147*(7), 2445–2450.

[85] Du, C., Tan, Q., Yin, G., & Zhang, J. (2014). *Chapter 7 – Applications of RDE and RRDE Methods in Oxygen Reduction Reaction,* Elsevier B.V

[86] Kaewsai, D., Lin, H. L., & Yu, T. L. (2015). *Influence of Pyridine-Polybenzimidazole Film Thickness of Carbon Nanotube Supported Platinum on Fuel Cell Applications*, Fuel Cells (2), 361–374.

[87] Byeon, A., Lee, K. J., Lee, M. J., Lee, J. S., Lee, I. H., Park, H. Y., … Kim, J. Y. (2018). *Effect of Catalyst Pore Size on the Performance of Non-Precious Fe/N/C-Based Electrocatalysts for High-Temperature Polymer Electrolyte Membrane Fuel Cells*. ChemElectroChem, *5*(14), 1805–1810.

[88] Braun, D., Cherdron, H., Rehahn, M., Ritter, H., Voit, B. (2013). *Chapter 4 – Polymer Synthesis: Theory and Practice,* Springer.

[89] Chem, J. M., Bjerrum, N. J., & He, R. (2012). *Synthesis and properties of poly (aryl sulfone benzimidazole) and its copolymers for high temperature membrane electrolytes for fuel cells*, Journal of Mat. Chem. 11185–11195.

[90] Choi, S. W., Park, J., Pak, C., Choi, K., Lee, J.-H., & Chang, H. (2013). *Design and Synthesis of Cross-Linked Copolymer Membranes Based on Poly(benzoxazine) and Polybenzimidazole and Their Application to an Electrolyte Membrane for a High-Temperature PEM Fuel Cell*. Polymers, *5*, 77-.

[91] Ma, Y. L., Wainright, J., Litt, M., & Savinell, R. (2004). *Conductivity of PBI Membranes for High-Temperature Polymer Electrolyte Fuel Cells*. Journal of The Electrochemical Society, *151*, A8–A16.

[92] Vilekar, S. A., & Datta, R. (2010). *The effect of hydrogen crossover on open-circuit voltage in polymer electrolyte membrane fuel cells*, Journal of Power Sources, *195*, 2241–2247.

APPENDICES

A. Calculations for Co-N/MWCNT catalyst

- Crystallite size calculation from XRD data;

$$L = \frac{0.89\,\lambda_{K\alpha}}{B_{(2\theta)}\cos\theta}$$

$\lambda_{K\alpha}$ = 0.154 nm, 2θ = 44.2° for Co (100)

B (FWHM) = 1.14 deg. = 0.0199 rad. $cos\theta = \cos\frac{44.2}{2} = 22.1$

$$L = \frac{0.89\,(0.154)}{0.0199\,(0.927)} = 7.43 \text{ nm}$$

- Crystallite-size correction from the Williamson-Hall plot;

$$B_{(2\theta)}\,cos\theta = \frac{0.89\,\lambda_{K\alpha}}{L} + 4\varepsilon sin\theta$$

Table A.1. *Summary of XRD data.*

Plane	Angle θ	FWHM (deg.)	FWHM (rad.)	Sinθ	Cosθ	βCosθ	4Sinθ
Co (100) 44.2°	22.10°	1.14	0.0199	0.38	0.93	0.018	1.50
Co (200) 51.4°	25.70°	1.45	0.0253	0.43	0.90	0.023	1.73
Co (220) 75.9°	37.95°	1.39	0.0237	0.61	0.79	0.019	2.46

To find the average particle size (*L*) from Williamson-Hall plot, the construction of a "y = mx + a" linear equation through "$Cos\theta$ *vs.* $4sin\theta$" is required. After the linear plot, the equation becomes,

y = - 0,0012 x + 0,0222

x-intersect of such an equation gives the strain induction (ε) while y-intersect is required for the calculation of particle size (L). Then,

$$0.0222 = \frac{0.89\,(0.154)}{L}\text{, } L = 6.23 \text{ nm}$$

- Calculations for the number of transferred-electron (n) through the oxygen reduction reaction (ORR) by using Koutecky-Levich plots.

Table A.2. *Rotation data and required conversions for K-L plots.*

rpm	**ω (rad/s)**	**ω^{-1} $(rad/s)^{-1}$**	**$\omega^{-1/2}$ $(rad/s)^{-1/2}$**
400	41.88	0.024	0.154
800	83.77	0.012	0.109
1200	125.66	0.008	0.089
1600	167.55	0.006	0.077
2000	209.44	0.0047	0.069

- Geometrical surface area of the GC electrode: A = 0.0707 cm^2,

Sample calculations for 0.2V;

Table A.3. *Current data and required conversions for K-L plots.*

i (A)	**i (mA)**	***J*** **(i/A) $(mA \cdot cm^{-2})$**	**1/*J*** **(A/i) $(cm^2 \cdot mA^{-1})$**
0.00017 (400 rpm)	0.17	2.39	0.418
0.00024 (800 rpm)	0.24	3.38	0.296
0.00028 (1200 rpm)	0.28	4.00	0.250
0.00032 (1600 rpm)	0.32	4.57	0.218
0.00034 (2000 rpm)	0.34	5.28	0.189

Constructing a K-L plot with ($1/J$ vs. $\omega^{-1/2}$) and obtaining y = mx + a linear equation will provide information about the number of the transferred electron (n) through the oxygen reduction reaction (ORR). From the K-L plot at 0.2V, equation was determined as y = 2.6289x + 0.0119. The slope of the $1/J$ vs. $\omega^{-1/2}$ straight line will equal $1 / (0.62nFCD^{2/3}v^{-1/6})$ (equation below) where "n" can be extracted easily.

$$\frac{1}{j} = \frac{1}{j_k} + \frac{1}{j_d} = \frac{1}{j_k} + \frac{1}{0.62nFC_{O_2}D_{O_2}^{2/3}v^{-1/6}\omega^{1/2}}$$

F; (96485 A×s×mol^{-1}); C_{O_2} (1.13×10^{-6} mol×cm^{-3}); D_{O_2} (1.93×10^{-5} cm×s^{-1}); ν (1.01×10^{-2} cm^2×s^{-1}).

$$\text{slope} = 1 / 0.62nFCD^{2/3}v^{-1/6}$$

$$1 / \text{slope} = 0.62nFCD^{2/3}v^{-1/6}$$

$$1 / 2.6289 = 0.115438 \text{ (n)}$$

$$n = 3.29$$

Same calculations were also applied to find "n" at 0.3, 0.4, and 0.5V which were found as 3.38, 3.40, and 3.95, respectively with an average of 3.50.

- Diffusion-limiting current density was calculated at 1200 rpm;

$$j_d = 0.62nFCD^{2/3}v^{-1/6}\omega^{1/2}$$

$$j_d = 0.404 \text{ (11.21)} = 4.53 \text{ mA·cm}^{-2}$$

- SSA_{Co} for Co-N/MWCNT, d [3,2] = 8.47 nm;

$$SSA_{Co} = \frac{6000}{\rho_{Co}\, x\, d[3,2]} = \frac{6000}{8.86\, x\, 8.42} = 80 \text{ m}^2\text{·g}^{-1}$$

B. Calculations for Pt-PBI/MWCNT catalyst

- Crystallite size calculation from XRD data;

$$L = \frac{0.89\,\lambda_{K\alpha}}{B_{(2\theta)}\cos\theta}$$

$\lambda_{K\alpha}$ = 0.154 nm, 2θ = 67.5° for Pt (220)

B (FWHM) = 4.9 deg. = 0.085 rad.

$$cos\theta = \cos\frac{67.5}{2} = 0.83$$

$$L = \frac{0.89\,(0.154)}{0.085\,(0.83)} = 1.94 \text{ nm}$$

- Crystallite size correction from Williamson-Hall plot;

$$B_{(2\theta)}\,cos\theta = \frac{0.89\,\lambda_{K\alpha}}{L} + 4\varepsilon\,sin\theta$$

Table B.1. *Summary of XRD data.*

Plane	Angle θ	FWHM (deg.)	FWHM (rad.)	Sinθ	Cosθ	βCosθ	4Sinθ
Pt (111) 39.7°	19.8°	5.1	0.089	0.33	0.94	0.084	1.34
Pt (200) 46.0°	23.0°	4.9	0.10	0.39	0.92	0.092	1.56
Pt (220) 67.5°	33.7°	5.9	0.085	0.55	0.83	0.07	2.22
Pt (311) 81.0°	40.5°	8.5	0.15	0.65	0.76	0.11	2.59

To find the average crystallite size (*L*) from Williamson-Hall plot, the construction of a "y = mx + a" linear equation through "$Cos\theta$ *vs. 4sin*θ" is required. After the linear plot, the equation becomes,

$$y = 0.1156\,x + 0.06857$$

x-intersect of such an equation gives the strain induction (ε) while the y-intersect is required for the calculation of crystallite size (L). Then,

$$0.06857 = \frac{0.89\,(0.154)}{L}\text{, } L = 1.99 \text{ nm}$$

- ECSA, SSA_{Pt} and η_{Pt} calculations for Pt-PBI/MWCNT;

Q_H = 0.001907 ($C \cdot cm^{-2}$) for H_2 adsorbtion/desorption region obtained from CV curve.

$$ECSA\ (m^2 g^{-1}) = \frac{1907\ (\mu C\ cm^{-2})}{210\ (\mu C\ cm^{-2})\ x\ 0.21\ (g\ m^{-2})} = 43\ m^2\ g^{-1}$$

$-Assuming\ d = 1.99\ nm\ from\ XRD\ data$;

$$SSA_{Pt} = \frac{6000}{\rho_{Pt}\ x\ d} = \frac{6000}{21.45\ (g\ cm^3)\ x\ 1.99\ nm} = 140.6\ m^2\ g^{-1}$$

$$\eta_{Pt} = \frac{ECSA}{SSA}\ x\ 100 = \frac{43}{140.6}\ x\ 100 = 30.6\%$$

$-Assuming\ d = 4.9\ nm\ from\ TEM\ images$;

$$SSA_{Pt} = \frac{6000}{\rho_{Pt}\ x\ d} = \frac{6000}{21.45\ (g\ cm^3)\ x\ 4.9\ nm} = 57.1\ m^2\ g^{-1}$$

$$\eta_{Pt} = \frac{ECSA}{SSA}\ x\ 100 = \frac{43.0}{57.1}\ x\ 100 = 75.3\ \%$$